الجمهورية الجزائرية الديمقراطية الشعبية
People's Democratic Republic of Algeria
وزارة التعليم العالي و البحث العلمي
Ministry of Higher Education and Scientific Research

Mohamed Khider Biskra University

Faculty of Exact Sciences and Life Sciences

Department of Material Science

Sector: Physics

Option: Physics of materials and photonic components

Ref:.....

Thesis presented with a view to obtaining

the diploma of:

DOCTORATE

Study of hybrid organic-inorganic solar cells based on perovskite materials

(Etude de cellules solaires hybrides organiques-inorganiques à base de matériaux pérovskites)

Presented by

Azri Faiza

Date: February 3rd, 2022

In front of the board of examiners composed of:

Ms MEFTAH Amjad	Professor , University of Biskra	Chair
Mrs MEFTAH Afak	Professor , University of Biskra	Supervisor
Mr DEHIMI Lakhdar	Professor, University of Batna	Examiner
Mr LAKHDAR Nacereddine	Professor , University of El Ouad	Examiner
Mr SENGOUGA Nouredine	Professor , University of Biskra	Co-supervisor

ACKNOWLEDGMENTS

All the thanks is for god, who gave me the force and the will to accomplish this work.

In this occasion, I would like to give special thanks, to my teacher and supervisor Pr. Meftah Afak, not only for the invaluable input and suggestions but also for being patient with me.

Many thanks to all my teachers at the University of Mohamed Khider Biskra.

And finally I would like to thank my little family and my big family who were always by my side for supporting me.

AZRI Faiza

Abstract

In this work two perovskite solar cells in n-i-p and p-i-n configurations were studied using SCAPS simulator. The two primary solar cells' structures are $FTO/ITO/Perovskite/PEDOT:PSS/Au$ and $FTO/PEDOT:PSS/Perovskite/ITO/Au$. The achieved power conversion efficiencies were 13.94% and 10.99%, for n-i-p and p-i-n PSCs, respectively. In order to enhance its performance, several materials were suggested as electron and hole transport layers (ETL and HTL). For both configurations, it was found that Zinc oxide (ZnO) and titanium dioxide (TiO_2) are the most adequate materials as ETL and Copper (I) thiocyanate ($CuSCN$) forms the appropriate HTL. Also, performances of n-i-p and p-i-n PSCs were improved by optimizing the absorber thickness which was found to be 1 μm. With these considerations the power conversion efficiency reached 25.02% and 25.11% for conventional (n-i-p) and inverted PSCs, respectively .In addition, the detrimental effect of defects at the $perovskite/TiO_2$ interface on our PSCs performance is also presented. Furthermore, the effect of temperature on PSCs were studied.

Key words: Simulation, Solar cell, Perovskite, conventional PSC, inverted PSC.

الملـخص

في هذا العمل، تمت دراسة خليتين شمسيتين للبيروفسكايت ذات البنيتين n-i-p و p-i-n بإستعمال برنامج المحاكاة SCAPS. الخليتين الأوليتين هما $FTO/ITO/Perovskite/PEDOT:PSS/Au$ و $FTO/PEDOT:PSS/Perovskite/ITO/Au$. مردود التحويل المتحصل عليه كان 13.94 % و 10.99% للخليتين العادية و المقلوبة على التوالي. من أجل تحسين أداء هاتين الخليتين، تم إقتراح العديد من المواد كطبقات ناقلة الالكترونات و الثقوب. من أجل كلا الخليتين، وُجد أن أكسيد الزنك و ثنائي أكسيد التيتان هما أنسب مادتين لنقل الإلكترونات و أن ثيوسيانات النحاس ($CuSCN$) هو المادة المناسبة لنقل الثقوب. أيضا، تحسين أداء الخليتين بجعل سُمك المادة الفعالة يساوي $1\ \mu m$. بإعتبار هذه التحسينات مردود التحويل وصل إلى 25.02% في الخلية العادية و الى 25.11% في الخلية المقلوبة. بالإضافة إلى ذلك، تمت دراسة التأثير الهدام للعيوب في السطح الفاصل بين البيروفسكايت و ثنائي أكسيد التيتان و كذلك تأير درجة الحرارة على أداء الخليتين.

الكلمات المفتاحية: محاكاة، خلية شمسية، بيروفسكايت، خلية بيروفسكايت عادية، خلية بيروفسكايت مقلوبة

Table of content

List of figures

List of tables

List of abbreviations

PSC	Perovskite Solar Cell
PV	Photo Voltaic
OPV	Organic Photo Voltaic
J	Current density
I	Current
V	Voltage
q	Elemantary charge
I_{ph}	Photogenrated current
I_d	Diode Current
I_S	Dark saturation current
K_B	Boltzmann constant
T	Absolute temperature
n	Ideality factor
R_s	Series resistance
R_{sh}	Shunt resistance
J_{sc}	Short circuit current
V_{oc}	Open circuit voltage
FF	Fill factor
P_{max}	Maximum produced power
V_m	Maximum voltage
I_m	Maximum current
η	Power conversion efficiency

P_{inc}	Incident power
$NREL$	National Renewable Energy Laboratory
HTL	Hole transport layer
ETL	Electron transport Layer
VB	Valence band
CB	Conduction band
MA	Methyl Ammonium
FA	Formamidinium
$HOIP$	Hybrid Organic Inorganic perovskite
DMF	Dimethylformamide
GBL	Gamma-butiloractone
$DMSO$	dimethyl sulfoxide
SHJ	Silicon heterojunction
IBC	interdigitated back contact solar cell
LED	Light Emitting Diode
$PeLED$	Perovskite Light Emitting Diode
ETM	Electron Transport Material
HTM	Hole Transport Material
TCO	Transparent Conductive Oxide
PCE	Power conversion efficiency
$HOMO$	Highest Occupied Molecular Orbital
$LUMO$	Lowest Unoccupied Molecular Orbital

Introduction

Introduction

Energy is necessary for humankind's existence and continuance. This energy needs technology to be produced and utilized. The resource of energy is one of the main factors that characterize the production process of energy. Furthermore, the energy sources can be divided into two categories according to the duration of its existence; the non-renewable energy includes all the sources of energy that can be exploited in a finite quantity, among them: Coal, natural gases, petroleum and its derivatives, radioactive elements. The quantity of energy obtained from non-renewable energy is high [1]. The renewable energy sources with an immediate regeneration includes: Solar, wind, tides, geothermal and hydroelectricity... etc. But the energy amount obtained from these sources is lower compared to the first category.

The sun produces energy in form of light. The idea of converting sunlight into usable form of energy is inspired from photosynthesis. This concept is used in solar cells basing on photovoltaic effect. The field of solar cells has witnessed great development over the years.

One of the most promising and most "talked-about" solar cells is hybrid organic-inorganic perovskite solar cells. The rapid growth in renewable energy and solar cells technology made perovskite solar cells (PSC) a specular star in photovoltaics industry. This relatively new technology requires huge researches because it promises excellent energy future; it also holds immense potential for better engineering, more efficient solar cells. PSCs composed of organic-metal-halide materials have made impressive progress in just a few years with maximum power conversion efficiencies (PCEs) evolving from 3.8 % in 2009 to a certified 22.1 % in 2016 [2] and today they exceeded 25 % in power conversion efficiency [3]. Hybrid organic–inorganic halide perovskite solar cells (PSCs) have risen to stardom owing to the unusual characteristics of the halide perovskite absorber such as high charge carrier mobility, large and strong optical absorption, long free carrier diffusion length, low exciton binding energy, cost, as well as their low processing temperature [4].

Motivation

Recently, perovskite materials are considered as promising candidates for hybrid solar cells due to their ease of fabrication, strong absorption of light, and low non-radiative recombination rates, plus its ability to exploit on over 20 years of development of related dye-sensitized and organic photovoltaic cells [5]. Perovskite cells are less costly to produce than their silicon counterparts and are flexible, lightweight, ultra-thin and semi-transparent according to their components and thickness [6]. The dramatically success of PSCs has attracted the experts of inorganic thin-films and organic PV materials to the field of PSC research. Perovskite solar cell includes a perovskite structured compound, such as hybrid organic-inorganic lead halide-based material as the absorption layer. This cell is more efficient than both thin-film technologies and the single-crystalline silicon solar cell. Furthermore, advances in the design of device architecture are one of the most important factors that drove the evolution of PSCs. Planar heterojunction structures in the n-i-p and p-i-n configurations are proposed as conventional and inverted structures, respectively. Furthermore, perovskite cells are able to produce energy from artificial light. Also they can be efficient even with incident sunrays from other angles in addition to 90 degrees angles unlike silicon panels [6].

Current deposition methods of perovskite materials made perovskite solar cells scaling up to be market competitors. Spin coating and Ink-Jet printer methods could be implemented to mass produce these cells at a very low production cost [7]

Aims and objectives

The major challenge of photovoltaic is to produce more efficient solar cells with less prices and long lifetime. One of the promising methods to enhance the performance of hybrid solar cells is to determine best candidate materials working as electron and hole transport layers. The aim of this work is to study the effect of changing electron and hole transport materials in order to achieve best efficiencies and to specify a bunch of options for charge transport layers. Also, studying and examining the performance of both conventional and inverted perovskite solar cells and determining the most efficient one. Using numerical simulation, two different configurations of perovskite solar cells

were investigated to determine which one is more efficient. Moreover, effects of electron and hole transport layers for n-i-p and p-i-n structures were studied by alteration them every time using its potential replacements.

Structure of the thesis

This thesis is organized into three chapters. Chapter one is a background on solar cells in general. The history and evolution of solar cells will be touched upon small paragraphs describing different generations of solar cells. Also, working principals of solar cell devices were explained leading to its electrical parameters and how to calculate them.

Chapter two is an overview on perovskite materials. In this chapter we will talk about history and evolution of perovskite materials then their crystal and electronic structure. Also, properties and deposition methods of perovskite materials will be discussed. Then, we will mention applications of perovskite based solar cells in some different fields and its possible architectures. Later, the hysteresis process of perovskite materials and its causes will be discussed briefly.

Chapter three is about simulation of perovskite solar cells. We will start by describing the utilized simulation software which is SCAPS 1D and its working basics such as the manner to define a problem and how to run it; also the most important steps for achieving a successful simulation as our study requires. After that, we will present the structure of modeled solar cell which is in planar configuration and results of simulating conventional and inverted perovskite solar cells. And make a comparison between their extracted output parameters.

Then, we will study the effect of charge transport layers on both solar cells in conventional and inverted configurations. This is in order to specify the suitable materials for transporting electrons and holes from both sides n and p, respectively. After that, we will enhance solar cells performance by improving thickness of absorber layer. Furthermore, we will present defects which may be present at perovskite/ titanium dioxide interface and studying the impact of these defects on solar cells performance. Finally, we will study the effect of temperature on PSCs' performance.

Chapter 1

Fundamentals of Solar Cell

1.1 Introduction

The safer and cleaner renewable energy sources are required to compensate the limited sources of conventional nonrenewable energy such as gas, coal and petroleum even the nuclear power generation. For many years, photovoltaic (PV) technologies offered such solutions and already have been used [8]. Initially, the use of PVs was for power generation on satellites and space craft [9] and later also for terrestrial applications [10].

Another factor favoring the development of PV industry, which is the growth of population in off-grid rural areas not connected to the state electrical networks (about 2.5 billion worldwide) [11]

Also, social concerns about modern improved living norms as well as the high human desire to economize spending money drove to relying on solar cells as an alternative energy source for terrestrial applications. In addition, there is a necessity to protect our health and environment. The use of environmentally-benign PV technology instead of the conventional fossil fuels is the lone way to reduce producing environmentally-harmful greenhouse gases [12].

Global energy deficiencies led to increasing research interests on PV technology [13]. In addition to improvement of the silicon solar cells efficiencies [14] with reduction of solar energy cost, a new PV materials and novel solar cells devices have developed. The increase in production volume and new cost efficient solar cell technologies rendered this achievement possible. Presently, a number of promising options for future developments of PV technology are available. The high cost of solar cell modules hindered the commercialization of these technologies. Improved performance, lower cost and reliability of PV systems remain major concerns even though efforts made by researchers over the years [15].

The base concept of the solar cell is converting sunlight into a usable form of energy. Where, the solar cell is an optoelectronic device able to convert light into electric current, both the direct sun light and also artificial or ambient light. The term light is

referred here as the electromagnetic radiation emitted by the sun on to the surface of the earth.

1.2 Evolution and History of Solar Cells

The best replacement of fossil fuel for energy generation is solar cells technology which is advanced in order to produce cheap, efficient and a long life time (stable) solar cells. In order to meet these ultimate goals in photovoltaic technology which has led to discoveries of new materials and new techniques in solar cells fabrication, research has been going on [16].

Today, four generations of solar cells are available, thus, enabling the use of different types of solar cells according to our needs and preferences.

1.2.1 First generation

Silicon solar cells are the most widely used of all solar cells, and they are also the most efficient in terms of single crystalline cell photovoltaic devices. These solar cells based on silicon wafer are considered as first generation solar cells. Bell Laboratories developed the first silicon solar cell in 1954 [16-17], with an efficiency of 6%. This type of solar cell is the most widely used with the highest reported cell efficiency (single crystal cell) of $\sim 28\%$ [18]. In this generation of solar cells, there are three types of silicon: single crystalline silicon ($c-Si$), multicrystalline silicon and amorphous silicon (a-Si). However, $c-Si$ is expensive and involves high cost of fabrication. This has increased recent research interests into the next generation of thin film solar cells.

1.2.2 Second generation

The second generation materials had been developed to reduce production costs of solar cells without threatens their energy efficiency [16]. This second generation materials had been developed to reduce production costs of solar cells without jeopardizing their energy output [16]. Thin film materials have been the subject of intensive research to

reduce the fabrication costs of the technology based on silicon, and to increase material utilization. The main materials emerged as the most promising candidates for this generation are: hydrogenated amorphous silicon ($a-Si:H$), cadmium telluride ($CdTe$) as well as copper indium diselenide ($CuInSe_2$) and its related alloys like Copper Indium Gallium diselenide $CuIn_xGa_{1-x}Se_2$ ($CIGS$) [19-20]. The highest recorded efficiencies of $CIGS$ and $CdTe$ thin film single cells are as high as 23.4% and 22.1%, respectively [21]. Most of materials consisting these cells are rare and expensive (indium) or highly toxic (cadmium). Because of these drawbacks, a different generation of solar cells has been inspired [19].

1.2.3 Third generation

The third generation of solar cells is the cheapest type of solar cells. The efficiencies gotten so far for dye-sensitized and organics single cells are $\sim 11.9\,\%$ and 16.5% respectively [21]. This indicates that the efficiency of organic solar cell generation is generally very low. Furthermore, organic photovoltaic is technologically immature and its wide spread applications are limited by several instabilities issues such as cells degradation mechanisms in different environments. Hence, OPV and dye-sensitized technology are relatively low to make these cells competitive in a commercial market [19]. With the relentless effort of researchers in photovoltaics, a new type of solar cell which is based on organic-inorganic hybrid solar cell known as perovskite solar cells emerged as promising technology.

1.2.4 Fourth generation

The fourth-generation solar cells are hybrid, which combine the low cost and flexibility of conducting polymer films (organic materials) with the lifetime stability of novel nanostructures (inorganic materials).

Fourth-generation approaches to photovoltaics (PVs) aim to achieve high efficiency devices but still use thin films deposition methods. Also, in common with Si-based thin-

film technologies, these will use materials that are both nontoxic and not limited in abundance.

This type of solar cells consist of p-n junctions in different semiconductor materials with increased bandgap are placed on top of each other, to absorb different sections of the solar spectrum. Where, the highest bandgap intercepts the sunlight first [22].

1.3 Working principle of typical silicon Solar Cell

The basic property common to all photovoltaic cells is that they convert sunlight into electrical power by the photovoltaic effect, which is the generation of a potential difference at the junction of two different materials when the device is illuminated by the sun radiation. Where, the device works as a diode in the dark and generates photovoltage under illumination. The conventional silicon solar cell structure is illustrated in Figure 1.1.

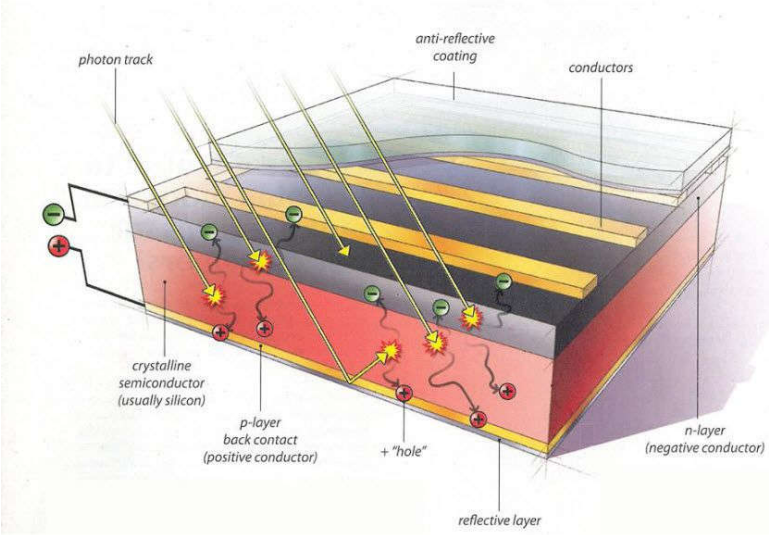

Figure 1. 1: Conventional solar cell structure.

The transformation of solar energy to an electric energy is based on three mechanisms:

1.3.1 Absorption of photons

Photons with energy more than gap energy are absorbed by the active material where these photons transferred to an electron-hole pairs. Electron moves to the conduction band leaving a hole at the valence band (Figure 1.2). The excess of photon energy compared with gap width is transferred to heat. While, photons with energy inferior than gap width go through the material without being absorbing [23].

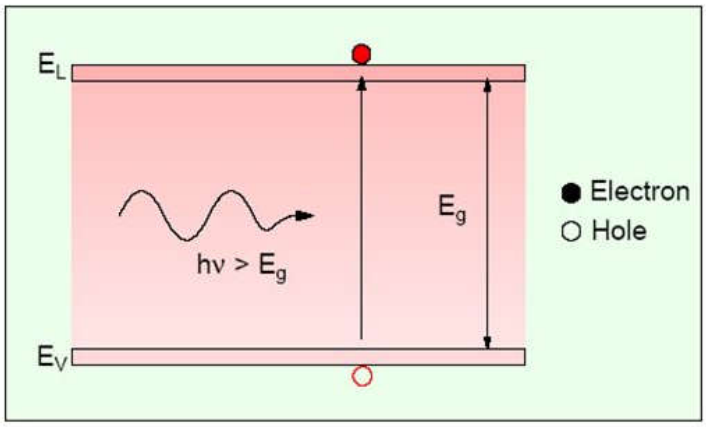

Figure 1.2: Absorption phenomena in semiconductors.

1.3.2 Conversion of photon energy to an electric energy

A zone of charge space is formed by depopulating the area between *n* and *p* materials leading to creation of an electric field, which is the responsible on electron-hole pairs separation at the *p*-*n* junction [24]. If the light-generated minority carrier reaches the *p*-*n* junction, it is swept across the junction by the electric field at the junction, where it is now a majority carrier as presented in Figure 1.3.

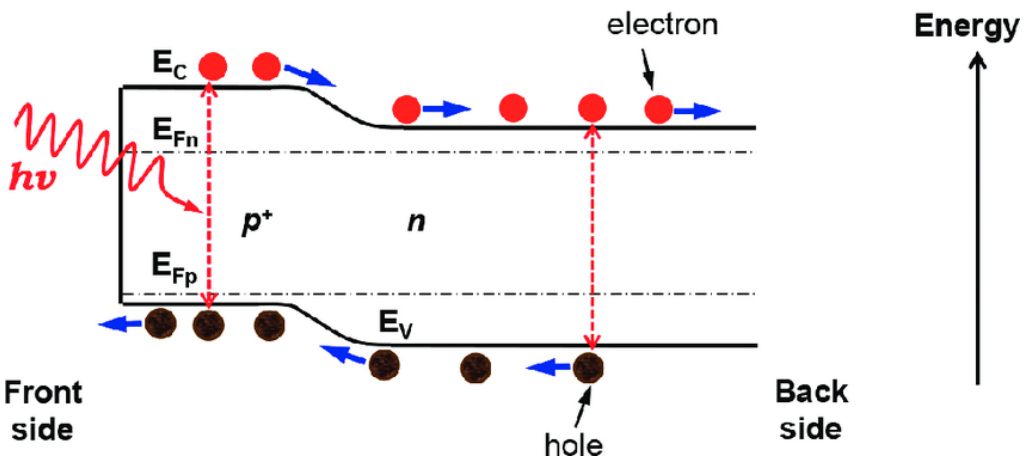

Figure 1. 3: Functioning principle of the solar cell.

1.3.3 Collection of charges

Charges are collected by metallic electrodes at front and rear surfaces of the cell. So, an electric current is generated by the solar cell [25].

1.4 Electrical parameters of the solar cell

The electrical behavior of the solar cell can be best described by its current-voltage characteristic curve ($J - V$) (Figure 1.4). Variations of current 'I' (or current density 'J') in function of voltage 'V' in dark and under illumination allow to evaluate the device performance [26].

1.4.1 Equivalent electrical circuit

The electrical behavior of an ideal device can be modeled using the Shockley diode equation (Equation 1.1) [27]:

$$I(V) = I_{ph} - I_d = I_{ph} - I_s\left(\exp\left(\frac{qV}{K_BT}\right) - 1\right) \quad 1.1$$

Where,

I_{ph} : Photogenerated current (A).

I_d : Diode current(A).

I_s : Dark saturation current (current density flowing through the diode under reverse bias in the dark),

K_B: Boltzmann constant $(1.38066 \times 10^{-23}\ J/K = 8.61400 \times 10^{-5}\ eV/K)$.

T : Absolute temperature (K).

q : Absolute charge of an electron $(1.60281 \times 10^{-19}\ C)$.

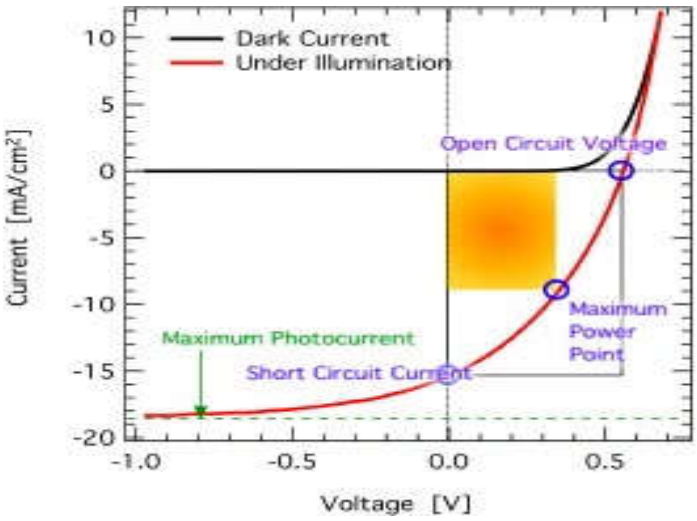

Figure 1. 4: J-V characteristic in dark and under illumination of a solar cell.

In reality, no device is ideal and so the equation must be modified to account for potential losses that may arise [28]. In case of real solar cell, the solar cell is modeled as presented circuit in Figure 1.5.

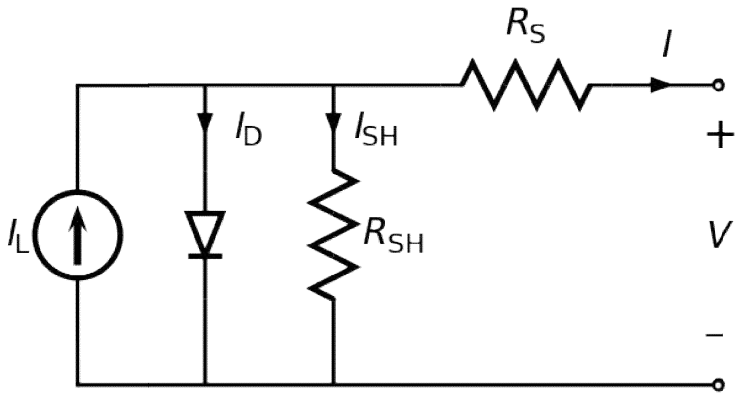

Figure 1. 5: The equivalent circuit of a real solar cell.

I-V characteristic is presented by Equation 1.2 [28]:

$$I = I_{ph} - I_s\left(\exp\left(\frac{q(V+IR_s)}{nK_BT}\right) - 1\right) - \frac{V+IR_s}{R_{sh}} \qquad 1.2$$

Where:

n : Ideality factor of diode.

R_s : Series resistance (Ω).

R_{sh} : Shunt resistance (Ω).

Ideally for an efficient solar cell, R_s should be minimized ($R_s \to 0$) and R_{sh} should be maximized ($R_{sh} \to \infty$) [29].

1.4.2 Short circuit current

The short circuit current is the maximum photo-generated current delivered by a solar cell when the terminals of the solar cell are short-circuited. It yields information about the charge separation and transport efficiency in the cell. $\boldsymbol{I_{sc}}$ is related to illumination intensity, illuminated surface, wave lengths of radiation, charges mobilities and temperature[27].

$$I(V = 0) = I_{sc} = I_{ph} \qquad 1.3$$

1.4.3 Open circuit voltage

At zero current ($I = 0$), the voltage reaches the maximum value ($\boldsymbol{V_{oc}}$) (i.e. when the terminals of the solar cell are not connected to each other) [27].

$$V_{oc} = \frac{nK_BT}{q}\, ln\,(\frac{I_{ph}}{I_s} + 1) \qquad 1.4$$

1.4.4 Fill Factor

The fill factor ($\boldsymbol{FF}$) is defined as the ratio between the maximum produced power (P_m) and the product of short circuit current and open circuit voltage. FF is used to characterize the non-ideality or in other words the "squareness" of the $J - V$ curve [30].

$$FF = \frac{P_m}{V_{oc}\times I_{sc}} = \frac{V_m\times I_m}{V_{oc}\times I_{sc}} \qquad 1.5$$

1.4.5 Power conversion efficiency

It is one of most important parameters, which is used to evaluate solar cells performance. The power conversion efficiency ($\boldsymbol{\eta}$)is defined as the ratio between the generated power by the cell (P_m) and the incident power from the sun radiation (P_{inc}).The efficiency depends on the spectrum and intensity of the incident sunlight and the temperature of the solar cell [27].

$$\eta = \frac{P_m}{P_{inc}} \qquad 1.6$$

Chapter 2

Perovskite materials and Solar cells design

2.1 Evolution and History of Perovskite Solar Cells

Recent type of solar cells has gained a major interest which is perovskite solar cells (PSCs) as "third and even fourth generation solar cells". The compounds with formula of ABX_3 (originated from the mineral name of calcium titanate $CaTiO_3$[31] generally belong to a perovskite-type compound; which was discovered in 1839 by German mineralogist Gustav Rose, and was named in honor of the Russian mineralogist Lev Perovski (1792-1856) [32].

Inorganic perovskite oxides (e.g., $CaTiO_3$, $BaTiO_3$, $LaMnO_3$, etc.) and halides ($CsSnI_3, CsPbI_3$, etc.),have gained a big attention due to their divers applications in optics, magnetics, electronics and superconductors [32]. Hybrid organic-inorganic perovskites which contains an organic ammonium cation (CH_3NH_3, $NH = CHNH_3$, etc.), a divalent metal cation (Pb^{2+}, $Sn^{2+}, Cd^{2+}, Fe^{2+}, Co^{2+}, Cu^{2+}$, etc.), and halide ions (Cl^-, Br^- or I^-), has attracted attention of scientific community [32].

The first perovskite solar cell was reported by Kojima et al. in 2009 [33]. They used methylammonium lead iodide ($CH_3NH_3PbI_3$, '$MAPbI_3$') and methylammonium lead bromide ($CH_3NH_3PbBr_3$, '$MAPbBr_3$') as solid sensitizers in dye-sensitized solar cells (DSSCs) with liquid electrolyte [13]. This DSSC showed low power conversion efficiency of 3.13% and 3.81% for $MAPbI_3$and$MAPbBr_3$solar cells, respectively [32-33].

In 2012, Michael M. Lee et al. reported a meso-Superstructured organometal halide perovskites solar cell with power conversion efficiency of 10.9% [21-34] by replacing the liquid electrolyte by a solid hole transport material (HTM). Due tremendous efforts by scientific researchers, power conversion efficiency reached 25.2% according NREL [3] (Figure 2.1).

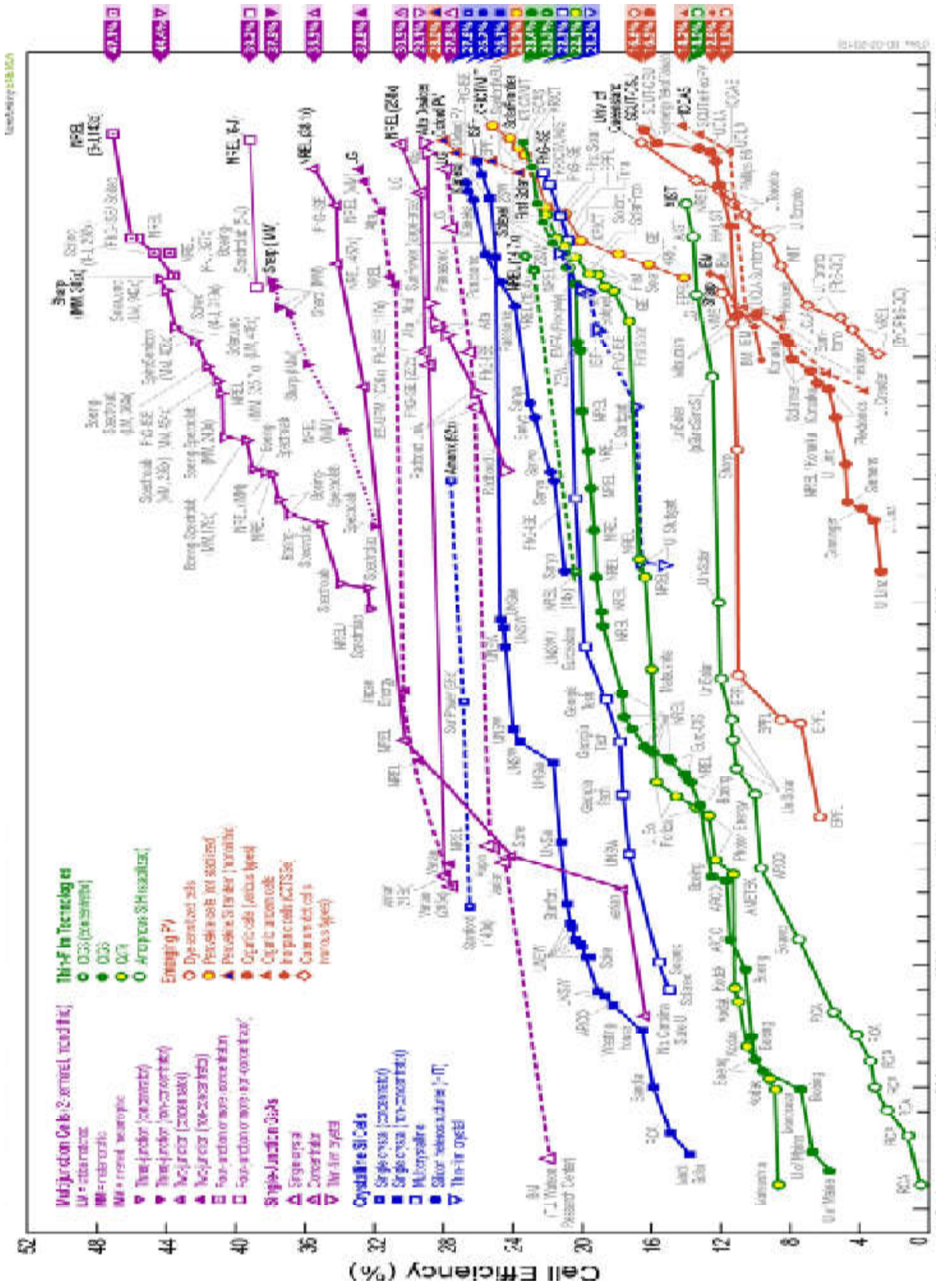

Figure 2. 1: Evolution of solar cell efficiencies.

Perovskite solar cells have much architecture that has evolved over time. First cell was based on the design of the liquid electrolyte DSSC configuration, which reported in 2009. In 2012, the first step to development of the mesoscopic and meso-superstructured architectures, when the liquid electrolyte was replaced by a solid state hole transport material (HTM) [32].

During 2013-2014, a “regular” structure was developed using penetrated perovskite materials into mesoporous metal oxide layer, and was capped by another layer on the top. Since then, the regular structure has been widely used to fabricate high-efficiency PSCs [32].

2.2 Perovskite Crystal Structure

As mentioned before, "Perovskite" originates from the mineral name of calcium titanate ($CaTiO_3$) and the compounds with formula of ABX_3 generally belong to a perovskite-type compound, where the A is a divalent and B is a tetravalent metal ions [32].

Figure 2.2 illustrates the perovskite structure, where the A cation is coordinated with twelve X ions and the B cation with six. Thus, the A cation is normally found to be somewhat larger than the B cation [35]. In addition to the oxide perovskites, halide-based perovskites are also well known.

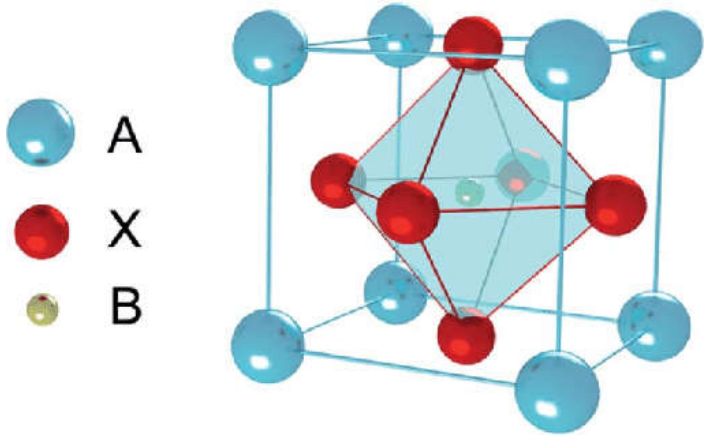

Figure 2. 2: Perovskite cubic crystal structure.

By replacing the cationic component with an organic ammonium at the A site, the resulting compound is called an "organic-inorganic perovskite compound". The metal

ion component usually is tin or lead. The general formula of perovskite compounds is $[(RNH_3)_mMX_n]$, in which modifications of metal (M), halide (X) and organic groups (R) precisely control the physical properties. Among them, the tin perovskite is relatively better for electrical conduction, and the lead one is better for optical properties [36].

In next sections, we will concentrate on $CH_3NH_3PbI_3$materials because much of the high efficiency solar cells have focused on $CH_3NH_3PbI_3$ as light absorber.

2.3 Electronic Structure of Perovskites

In the hybrid perovskite structure of $CH_3NH_3PbI_3$, the metal has an occupied s orbital (lone pair) whose electrons interact strongly with the in-plane anion p states forming an anti bonding state as the top of the VB with mostly s-orbital character. The CB minimum is constituted from anti-bonding Pb(6p)-I(5p) states with a p orbital character (Figure 2.3.a) [37].

The substitution of the monovalent A cation does not directly affect the electronic band structure in halide perovskites [32].

Both VB and CB are formed by anti-bonding orbitals. The anti-bonding structure contributes to suppression of charge recombination leading to superior photovoltaic property such as high voltage generation. Figure 2.3.b, shows a high symmetry of band structure, which enables direct p-p electron transition from VB to CB [40].

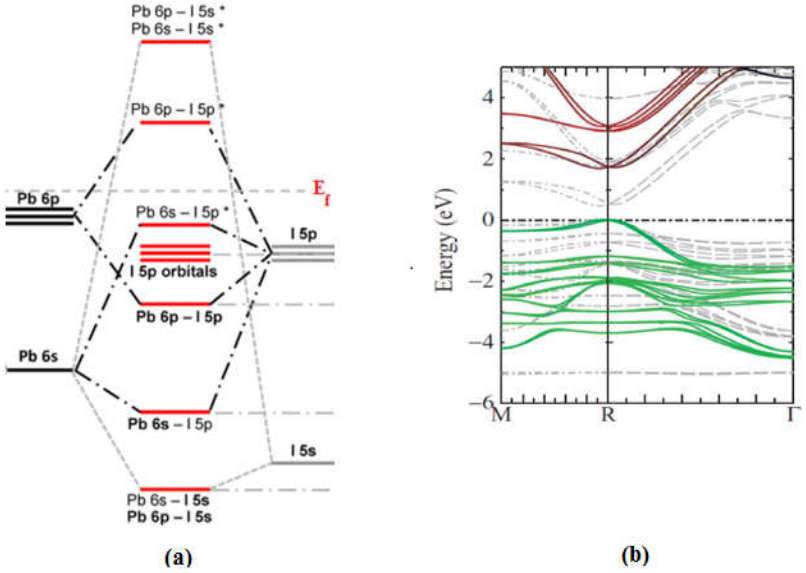

Figure 2. 3: (a) Bonding diagram of a $[\boldsymbol{PbI}\ ]^{-}$ cluster, representing the perovskite $\boldsymbol{CH_3NH_3PI_3}$[38] and (b) The bottom shows the band gap structure for the quasiparticle self-consistent GW approximation [39].

2.4 Tuning the band gap with composition

The composition of the perovskite AMX_3 has been altered by incorporating other monovalent cations A [formamidinium (FA^+) and Cs^+], divalent cation$M$ (Sn^{2+}), and halide ions X (Br^- and Cl^-), which results in optical absorption tunability [4] as shown in figure 2.4. This make their band gap can be tuned widely from the blue to the red spectral regions [41]. As mentioned before, the valence and conduction bands of perovskites are determined by the inorganic octahedron. The organic cation does not contribute to these bands but modulates the band gap by modifying the lead-halide bond distance [41].

However, the tolerance factor t affected by the A cation size, changes the spacing of $[MX_6]^{-2}$ octahedra, leading to altering the band gap. The decreased ionic sizes of FA^+, MA^+, and Cs^+ cations (253, 217 and 181 pm, respectively) led to increasing band gaps 1.48, 1.52 and 1.67 eV for ($FAPbI_3$), ($MAPbI_3$),) and ($CsPbI_3$),), respectively [3]. While the ionic size of the halide decreases, the band gap increases and for single crystals it is found to be 2.97, 2.24, and 1.53 eV for the Cl, Br, and I perovskite, respectively [42].

The full tunability of the band gap for $CH_3NH_3PbX_3$ has been demonstrated for $I-Br$ compositions and strongly recommended for $Br-Cl$ compositions from UV–visible absorption spectroscopy and PL measurements [41]. From a photovoltaic perspective, $MAPbI_3$ is thus suitable for single band gap absorbers and $MAPbBr_3$ could be interesting for tandem applications whereas $MAPbCl_3$ is relevant to light emitting devices [42].

Using perovskites with mixed cations and halides is an important theme because the pure perovskite compounds suitable for PV applications come with numerous disadvantages [42]. For instance, some MA stabilizes the perovskite structure and prevents it from transforming into the yellow polymorph known for the FA perovskites. Introducing Br allows tuning the band gap, which is favorable for tandem applications, and some Br appears to be favorable for the device performance [42]. Moreover, incorporation of the inorganic Cs^+ stabilizes the perovskite phase of $FAPbI_3$ and reduces the defect density [4].

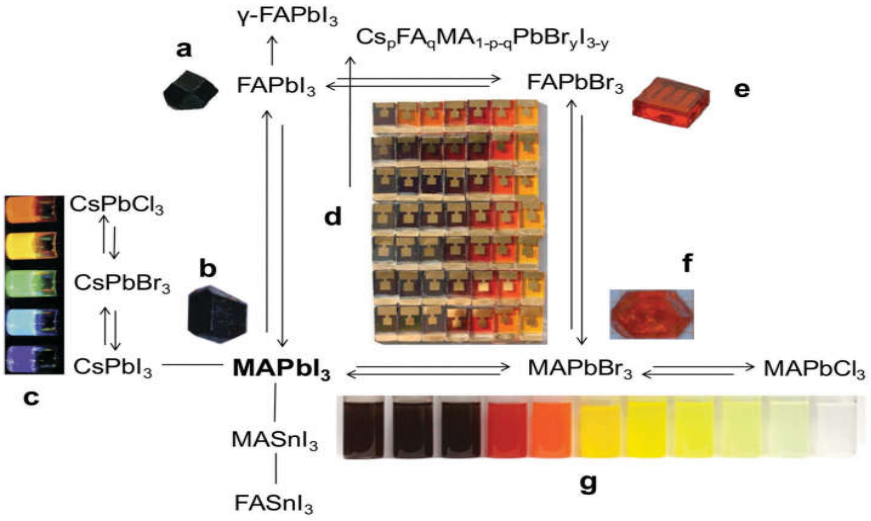

Figure 2. 4: The versatility of hybrid perovskite material $\boldsymbol{Cs_pFA_qMA_{1-p-q}PbBryI_{3-y}}$ and their absorption tunability. Schematics of some investigated perovskites closely related to $\boldsymbol{APbI_3}$. The insets show (a) single crystal of $\boldsymbol{FAPbI_3}$, (b) single crystal of $\boldsymbol{MAPbI_3}$, (c) colloidal solutions of $\boldsymbol{CsPbX_3}$ $(\boldsymbol{X = Cl, Br, I})$ perovskites, (d) solar cells of 49 different compositions in the $\boldsymbol{MA/FA - Pb - Br/I}$ compositional space, (e) single crystal of $\boldsymbol{FAPbBr_3}$, (f) single crystal of $\boldsymbol{MAPbBr_3}$ and (g) colloidal nanocrystals of $\boldsymbol{MAPbX_3}$ $(\boldsymbol{X = Cl, Br, I})$ perovskites [4].

2.5 Doping of perovskite materials

Doping is regarded as intentional introduction of a small amount of 'impurities' into an otherwise pure material (host) to tune its electronic properties (e.g. hole or electron transport) [43].

Certainly, dopants engineering has emerged as one powerful strategy to tailoring the properties of halide perovskites, making this prominent material even more attractive for practical applications.

Doped halide perovskites exhibit diverse optical and electronic properties with respect to undoped counterparts, with principal characteristics including enhanced stability, high quality thin films with enlarged grain size, improved photoluminescence quantum yields, new emission characteristics, reduced defect state density, thus leading to excellent optoelectronic performance of devices that were constructed by using the doped perovskites as active layers.

Various dopants, including main group metals (e.g., Bi, Rb, K, Sr, Al), transition metals (e.g., Mn, Zn, Cd), and rare earth metals (e.g., Ce, Yb, Er), have been successfully doped into halide perovskite polycrystalline films, single crystals, and nanocrystals, giving rise to a wide variety of exotic properties different from those of the mother compounds. Also, Mojtaba abdi-jalebi et al. found that Na^+, Cu^+, and Ag^+in NaI, $CuBr$ (or CuI), and AgI cation halide based salts, respectively, have ionic radii similar to Pb^{2+} and can be doped into the perovskite absorption layer to regulate the morphology and photophysical properties of perovskite to improve the photovoltaic performance of perovskite thin films [44].

The metallic elements, including main group metal cations, transition metal cations, and rare earth metal cations that have been doped in halide perovskites, are marked in the periodic table (Figure 2.5). The orange, blue, green, and yellow colors denote the metal dopants for optoelectronic performance control, crystal growth control, structural stability control, and light conversion in halide perovskites, respectively [45].

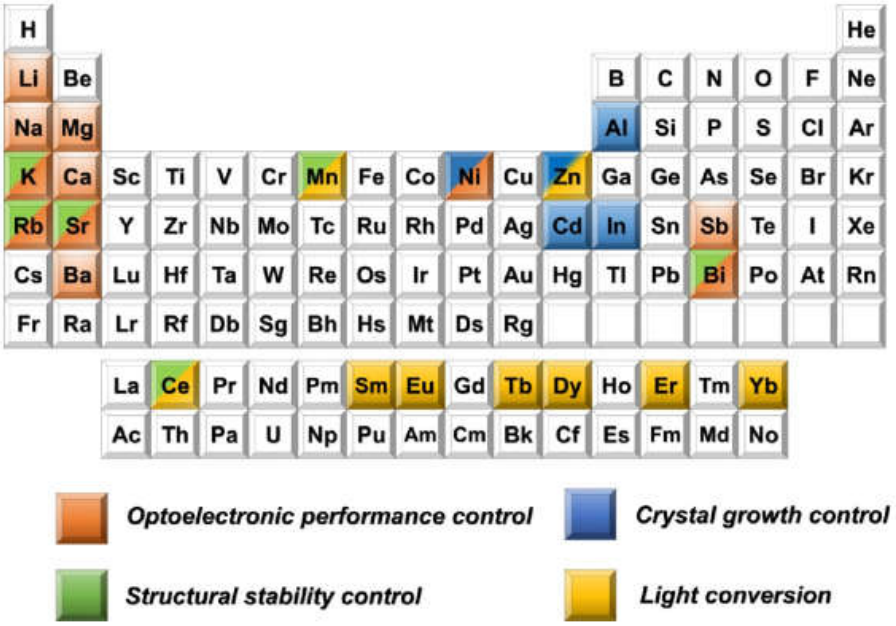

Figure 2. 5: Doping materials in halide perovskites [39].

Furthermore, Yin et al. and Wang et al. [46] showed experimentally and theoretically, respectively, that HOIPs may be possibly self-doped as a result of crystal defects engineering [43]. It has been proposed recently that perovskite solar cells represent p-i-n devices where p-type doping is induced by the presence of lead and methyl ammonium vacancies (V_{Pb} and V_{MA}), while n-doping results from the presence of iodide vacancies (V_I) as it follows from the theoretical calculations. It is believed that doping can be achieved in $MAPbI_3$ by using different MAI and PbI_2 ratios in the precursor solutions [47].

2.5 Properties of organic-inorganic hybrid perovskites

Perovskite materials have many advantages as light absorber, such as:

- Strong absorption coefficients, low non-radiative carrier recombination rates and small effective masses of electrons and holes [38]
- The perovskites are direct band gap semiconductors [39].

- The electron/hole diffusion lengths are observed to be longer than 100 nm. and low energy loss [39].
- Low temperature solar cell processing preferably via the printing techniques [31], which makes it possible to be deposited on a flexible substrate (Figure 2.6).
- Low payback time due to the low cost of production and the high performance [48].

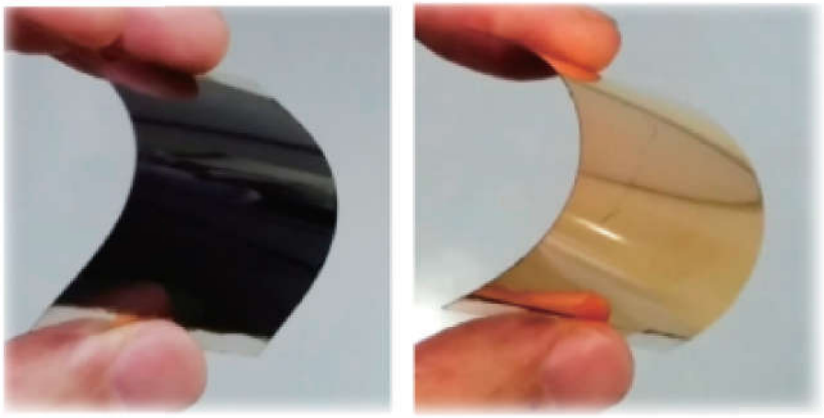

Figure 2. 6: Photograph shows a large plastic film perovskite device (left: perovskite side, right: gold electrode side) fabricated by the low temperature coating methods.

- Photovoltaic properties of perovskite are benign to defect formation. Because, ionic vacancies form trap states that reside within VB and CB or exist as shallow defects near VB and CB. Carriers trapped by very shallow defects can be detrapped easily and can contribute to current generation [40].
- Mobility of carriers in $\boldsymbol{CH_3NH_3PbI_3}$ is ambipolar, exhibiting similar effective mass for both electron and hole (0.23 and 0.29, respectively) which agrees with the concept that the perovskite is an intrinsic semiconductor unlike Si and GaAs [40].

Moreover, perovskite materials have been attracted attention due to their interesting characteristics of the inorganic components, which include: thermal stability and the high degree of structural order and also due to the properties of the organic component such as the functional versatility, mechanical flexibility and low-cost processability [48].

2.6 Deposition methods of perovskite films

Many scientific researches and potential applications concerning organic-inorganic hybrid materials strongly depend on accessibility and reliability of simple fabrication techniques. Fabrication of hybrid materials faces some difficulties such as decomposition of the organic components and finding an appropriate solvent because the chemical and physical properties of organic and inorganic components, in addition the unfavorable characteristics of some substrates make the deposition inhomogeneous [49]. Despite these difficulties, preparation of perovskite layers became essential for fabricating high efficiency devices. Generally, accurate control of the stoichiometry, crystallographic phase, and grain structure of the perovskite material is required to fabricate high efficiency perovskite solar cells [4]. These parameters can be controlled by four primary deposition methods: one-step solution process, two- steps solution process, vapor-assisted solution process and thermal evaporation process.

2.6.1 One step solution process

The one-step solution process was the first used method to fabricate perovskite films. And now it is the most used and adopted technique in preparing perovskite materials due to its simplicity. In this method, methylammonium iodide (CH_3NH_3I) and lead iodide (PbI_2) are taken in 3:1 molar ratio, and dissolved in an aprotic polar solvent, such as dimethylformamide (DMF), gamma-butyrolactone (GBL), dimethyl sulfoxide (DMSO), N-2- methyl pyrrolidone, or a mixture of them to form a homogenous precursor solution. The solution is then spin coated on the substrate and dried and heated at mild temperatures (70 °C – 100 °C) until the film turns into black color which indicates that $CH_3NH_3PbI_3$ film is formed [50-51], the method is illustrated in figure 2.7. Films prepared using the single-step solution method exhibited highly porous morphologies consisting of perovskite crystallites in spherical and polygonal shapes (with GBL) or needle shape (with DMF) [4]. The spinning rate, drying process, and temperature are expected to affect the $CH_3NH_3PbI_3$ morphology [51]. Additionally, the environmental conditions (e.g., oxygen and humidity), morphology of the substrates, can also influence the uniformity, crystallinity, phase purity, surface morphology, and interface properties of the perovskite films [4]

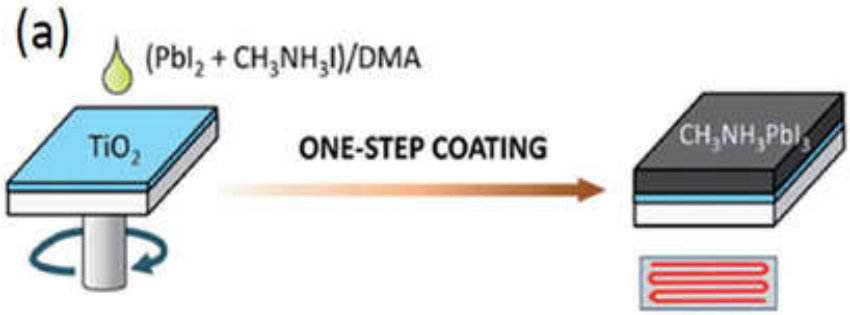

Figure 2. 7: Perovskite film deposition by one step procedure.

2.6.2 Sequential two steps solution process

Devices prepared by one step solution process exhibited a poor surface coverage of perovskite films [4]. To surmount this, Burschka et al. developed the two steps solution deposition method to prepare uniform $MAPbI_3$ on a mesoporous TiO_2 layer. The two steps method is illustrated in Figure 2.8. In this technique, PbI_2 salt is dissolved in DMF and is deposited on a glass substrate using vacuum evaporating or spin coating method followed by dipping the slide into $CH_3NH_3I(MAI)$ solution or spin coating the MAI solution on PbI_2 film. The films then are dried in mild temperature for while. The black color of the films gives a visual confirmation of the $CH_3NH_3PbI_3$ thin film formation [40-4]. The films prepared by the two-step method were dense and conformal [4]. The dipping time and concentration of the PbI_2 precursor solution were found to affect photovoltaic performance [51].

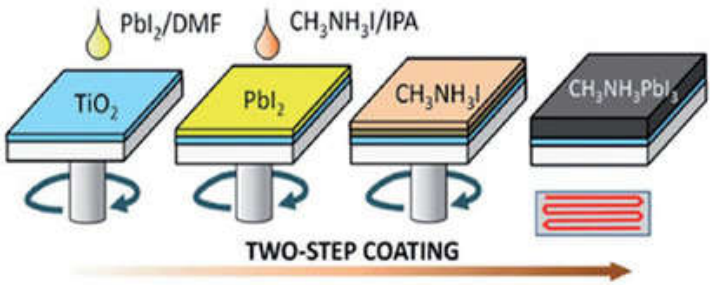

Figure 2. 8: Perovskite film deposition by two steps procedure.

2.6.3 Vapor Assisted Solution Process

Developing the two steps solution deposition to vapor deposition of MAI is known as vapor assisted solution process. A uniform and conformal $MAPbI_3$ films with high phase purity was fabricated by Chen et al. using this method [4]. In vapor assisted solution process presented in Figure 2.9, the germ layer of PbI_2 is spin coated than exposed to MAI vapor generated from heating MAI powder at 150 $c°$ in an inert environment. This method produces perovskite films with a full conversion of PbI_2 and a conformal, uniform and smooth film with large sized grains up to the micrometer scale. In the other hand, vapor assisted solution process is limited by the slow incorporation process of MAI into PbI_2 framework which needs a several hours to complete conversion [4].

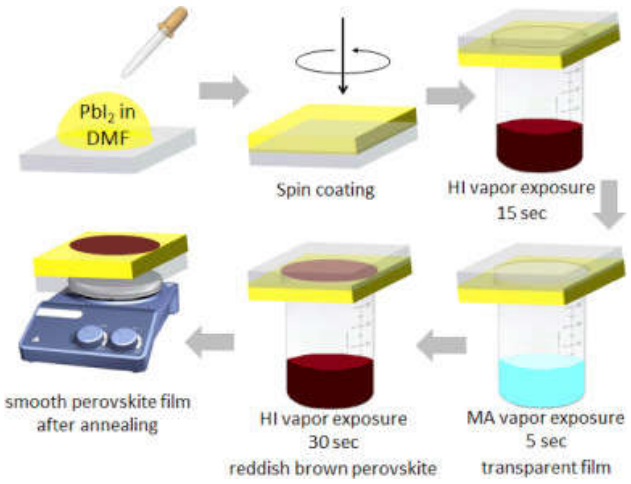

Figure 2. 9: Perovskite film deposition by vapor assisted solution process.

2.6.4 Thermal Vapor Deposition

Smooth, conformal and uniform $MAPbI_{3-x}Cl_x$ perovskite films were resulted from co-evaporation of $PbCl_2$ and MAI then annealing by Snaith et al. in 2013 [4]. Alternative vapor deposition methods were developed such as the layer-by-layer vacuum evaporation, chemical vapor deposition and flash evaporation. Vapor deposition method results uniform and pinhole-free perovskite films compared to solution processed films (Figure 2.10). The benefits of this technique are that it is possible to precisely control the thickness and smoothness of the thin-film surfaces [49]. However, only few research

groups have fabricated high efficiency devices using this method, because it is difficult to control temperature during deposition due to the low thermal stability of both the precursor and the products.

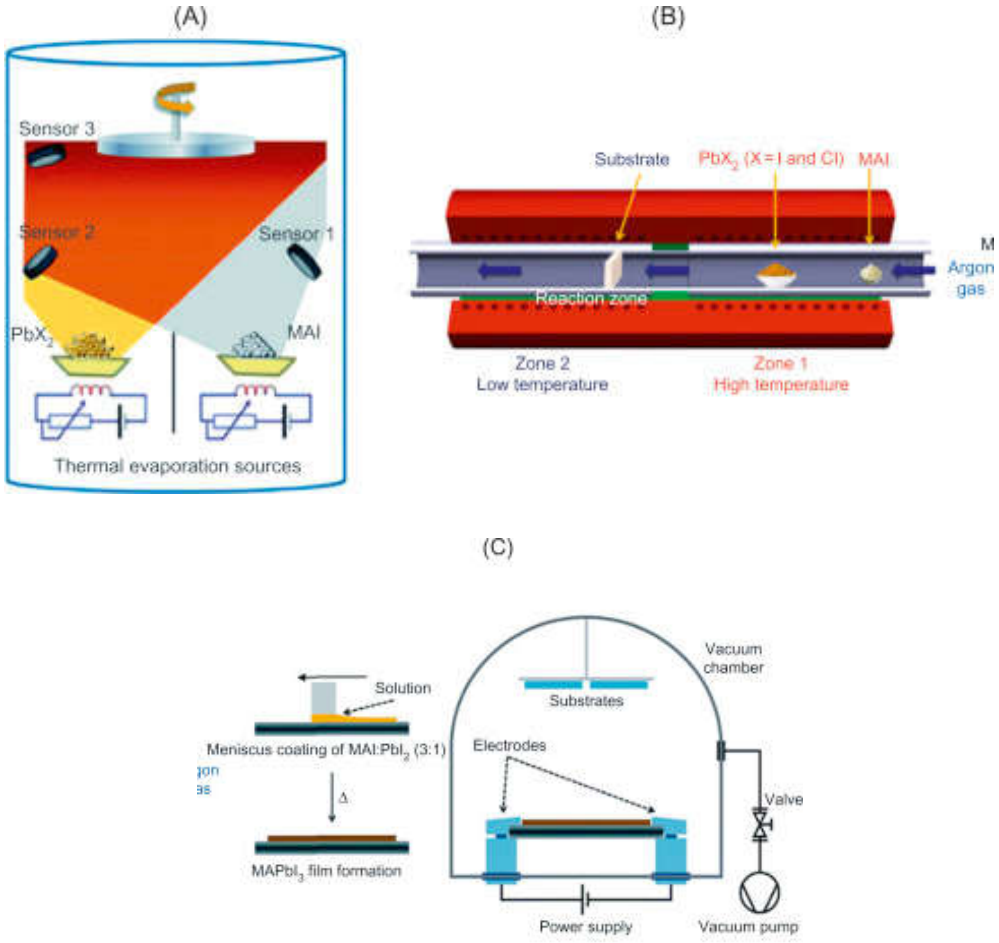

Figure 2. 10: (a) dual source evaporation, (b) chemical vapor deposition, and (c) flash evaporation.

2.7 Applications of organometal halide perovskites

Optical and electrical properties as well as low processing cost of organic-inorganic perovskites have got researches attention due to its electronic structure. These properties could to adapt the new requirements of scientific studies and technical developments [49]. A variety of technologies can benefit from the special properties of these promising materials.

2.7.1 Solar cells

Because of promising potential to transfer renewable solar energy to electric energy, solar cells based on perovskites are one of the most attractive optoelectronic applications. Advances in the design of device architecture are one of the most important factors that drove the evolution of perovskite solar cells [4]. The first solar cells based on lead iodide based perovskite sensitizers were reported by kojima et al. in 2009. Where, they constructed a $CH_3NH_3PbX_3/TiO_2$ (X: I or Br) liquid sensitized solar cell. The obtained power conversion efficiency were found to be 3.13% and 3.81% for $CH_3NH_3PbBr_3$ and $CH_3NH_3PbI_3$ based solar cells, respectively [33]. Also, they concluded that using a series of hybrid perovskite materials $CH_3NH_3MX_3$ (M: Pb, Sn; X: $halogen$) with a different energy gaps can optimize the perovskite solar cell performance [33]. Replacing the liquid electrolyte with a solid hole transport material overcame the instability issue associated with the liquid electrolyte [4]. Hybrid organic inorganic perovskites are ideal candidates for tandem solar cells due to their tunable bandgap that ranges of 1.2 – 2.3 eV and versatility in the device configurations [4].

Furthermore, perovskites based solar cells can be optimized by using appropriate contacts to make photogenerated charges efficiently extracted [41]. In current designs, as it will be more detailed in the next paragraphs, the perovskite is sandwiched between two different materials; the electron and the hole transport layers.

2.7.2 Multi-junction photovoltaics

The efficiency of a single-junction solar cell is limited by the Shockley– Queisser limit, which includes losses from transmitted below-band-gap photons and from thermalization of hot photogenerated carriers [41]. The tandem design can better utilize the solar energy so that high-energy photons are absorbed by the upper wide bandgap subcell, while those in longer wavelength region are harnessed by the bottom narrow bandgap subcell [52]. The designs of the multi-junction concept can be divided into four configurations: two-terminal (2-T) monolithically integrated (two stacked cells that are connected electrically in series) and four-terminal (two mechanically stacked cells that are electrically independent represented in Figure 2.11.a), the spectral splitting systems and four-terminal reflective tandem [41-52-53].

The monolithically integrated two-terminal perovskite/silicon tandem architecture consists of a perovskite top cell, which is deposited onto the silicon bottom cell. The two subcells are then electrically connected in series, through a recombination layer or tunnel junction.

The four-terminal tandem (Figure 2.11.b) is the most simple tandem device architecture. The two subcells are fabricated independently, mechanically stacked on top of each other and contacted individually.

A four-terminal spectral splitting tandem device consists of a dichroic mirror, which splits the light toward the high and low bandgap cells, as illustrated in Figure 2.11c. In four-terminal reflective tandem configuration, the PV Mirror concept is used which is a concentrating mirror, spectrum splitter, and light-to-electricity converter all in one: It consists of a curved arrangement of cheapest subcells that absorb part of the solar spectrum and reflect the remainder to their shared focus, at which a second solar converter is placed illustrated in Figure 2.11.d [53].

Stacking perovskite cells on well-established photovoltaic cells, such as those made from crystalline Si ($c-Si$), $GaAs$, $CIGS$, or $CdTe$ could maintain high efficiencies. Where, the perovskite cell can be used as the top cell because its band gap can be tuned to transmit sufficient light to the bottom cell. Also, producing perovskite cells on top of other cells does not damage them because of low-temperature processing of the hybrid perovskite cells [41].

In 2017, a power conversion efficiency is obtained for the monolithically integrated two-terminal solar cell $CsFAPbI_{3-x}Br_x$ /SHJ (SHJ: Silicon heterojunction) reached 23.6 % and 26.4% for mechanically stacked four-terminal $RbCsMAFAPbI_{3-x}Br_x/IBC$ (IBC: interdigitated back contact solar cell) [53]. A 23.4% conversion efficiency is achieved for the $CH_3NH_3PbBr_3/Si$ $PERL$ system in spectral splitting configuration [54].

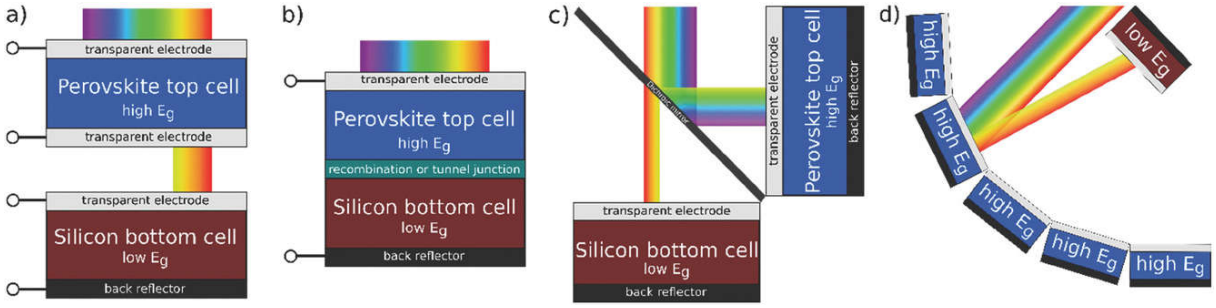

Figure 2. 11: Schematics of several perovskite/silicon tandem architectures: a) 4-terminal mechanically stacked; b) 2-terminal monolithically integrated; c) 4-terminal optical spectral splitting; d) 4-terminal reflective tandem.

2.7.3 Building-integrated photovoltaics

Building-integrated photovoltaics are an attractive concept for economic generation of solar power [41-55]. Neutral color tinted windows with controllable levels of transparency is more demanded for novel applications in windows, cladding of buildings and vehicles [55-56];and combination between tunable semi-transparency and high-power-conversion efficiency could be delivered by perovskites [41].

Giles et al. fabricated microstructured perovskite solar cells with a discontinuous active layer. The perovskite layer was formed as islands with the spiro-OMeTAD infiltrating the spaces between and also coating the islands with a thin layer. They found that, incorporation of a dye or pigment into the regions where light passes through modifies optically the semitransparent cells as shown in Figure 2.12[55].

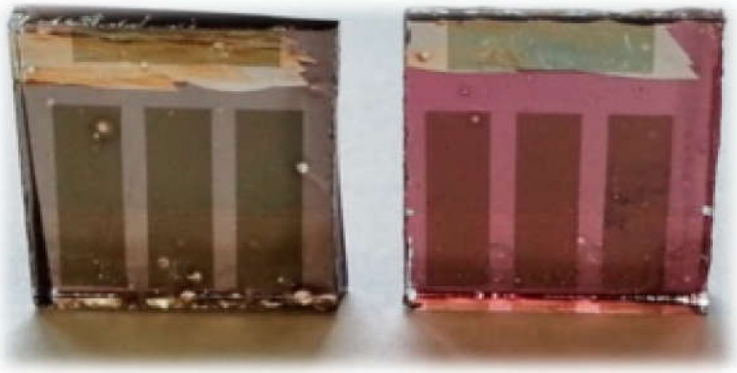

Figure 2. 12: Picture of semitransparent perovskite solar cells without (left) and with (right) D102 dye included in the spiroOMeTAD layer, with 10 nm gold electrodes [55].

Recently, a $1.3m \times 0.9m$ perovskite photovoltaic panel made by Construction company Skanska's Warsaw contains 52 modules and seeks to cover the energy needed to light one employee's workspace for eight hours [57]. Saule uses ink-jet printing. The inks were formulated so that every layer of different material in the cell has the right properties to produce and transport electrons when light is shone on them (Figure 2.13) [57].

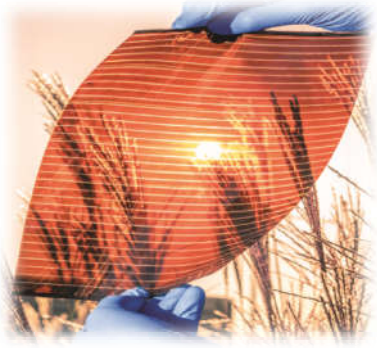

Figure 2. 13: A flexible, ultrathin, ultralight and semitransparent perovskite film produced by Saule Technologies [57].

2.7.4 Light emitting diodes

Light-emitting diodes (LEDs), a kind of solid-state lighting device based on inorganic semiconductors could provide highly efficient and convenient light point sources of different colors. Organometal halide perovskites have the potential to produce highly efficient light emission spanning the visible spectrum and exceptional color quality at low cost, resulting from their extraordinary optical property and compatibility with roll-to-roll solution processed techniques [58]. Most recently, high brightness perovskite LEDs (PeLEDs) with panchromatic colors covering the entire visible spectra has been realized from organometal halide perovskites $CH_3NH_3MX_3$ ($M = Pb$ or Sn, $X = Cl, Br$ or I) at room temperature, which potentially opening up a wide range of optoelectronic applications in addition to solar cells [59].

At 2014, a green and red electroluminescence from $CH_3NH_3PbBr_3$ and $CH_3NH_3PbBr_2I$ based PeLEDs, respectively were reported by Tan et al. as showed in Figure 2.14 [60]. The green PeLED achieved a luminance of 364 $cd\ m^{-2}$ at a current density of 123 $mA\ cm^{-2}$, giving external quantum efficiency of 0.1%, while a luminance

of 16.2 $cd\ m^{-2}$ was achieved at a current density of 55 $mA\ cm^{-2}$ and external quantum efficiency of 0.018% or 0.03 $cd\ A^{-1}$ was achieved at 5.7 V for red PeLED [60].

Also, Nana et al. have reported a green perovskite light emitting diode based on $MAPbBr_3$ perovskites, with a low turn-on voltage of 2 V and an external quantum efficiency of 0.43% at a brightness of 5000 $cd\ m^{-2}$ [61].

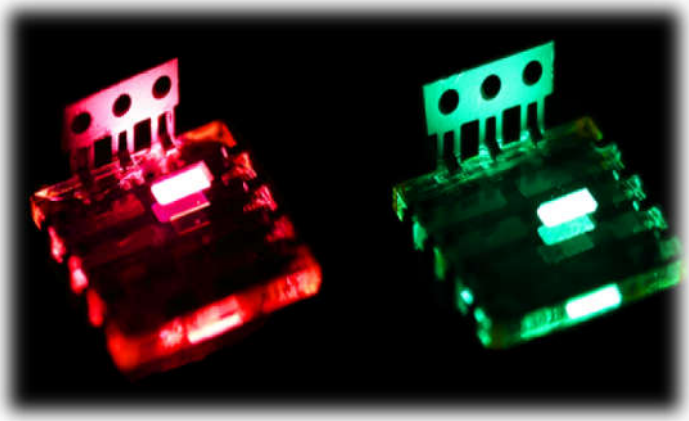

Figure 2. 14: Green and red perovskite LEDs [60].

Most recently, Zhao, X and Zhi-Kuang Tan has developed high-efficiency, near-infrared LEDs that can cover an area of 900 mm^2 using low-cost solution-processing methods. Using $FAPbI_3$ perovskite, they reported a 799 nm near-infrared PeLED that operates with an external quantum efficiency (EQE) of 20.2%. (Figure 2.15). Note that, infrared LEDs are useful for optical communications and convert illumination, and are commonly found in remote controls and security camera setups [62].

Figure 2. 15: Photograph of near infrared flexible PeLED with large-area [62].

2.7.5 Solar water-splitting

The conversion of sunlight directly into chemical fuels is a process called artificial photosynthesis using a splitting solar cell. Perovskite solar cells have already been used to split water into $O_2$and H_2.Generally the output voltage for $CH_3NH_3PbI_3$ solar cells at maximum power point is around $0.9\,V$, so tandem cells are needed in water photolysis [56]. The structure of solar water-splitting is based on two perovskite solar cells connected in series as illustrated in figure 2.16. Perovskite tandem solar cell is used to achieve the photovoltage necessary to overcome the thermodynamically required minimum voltage of $1.23\,V$ for splitting water and the additional 0.1 and $0.3\,V$ for kinetically driving the $H_2$and O_2evolution reactions [41].

Luo et al. connected two $CH_3NH_3PbI_3$ solar cells (outside the electrolyzer vessel) in series to split water and achieved a solar-to-hydrogen conversion efficiency of 12.3% [56], which is close to the most notable example of water-splitting using GaInP/GaAs tandem cells that achieved 12.4% [41].

Most recently, Mohite, A. et al. developed a water splitting system for H_2 fuel production using low-cost abundant materials (Figure 2.16). The Device was constructed of $>20\%$ efficient perovskite solar cells with >1500 hrs stability in operation [63].

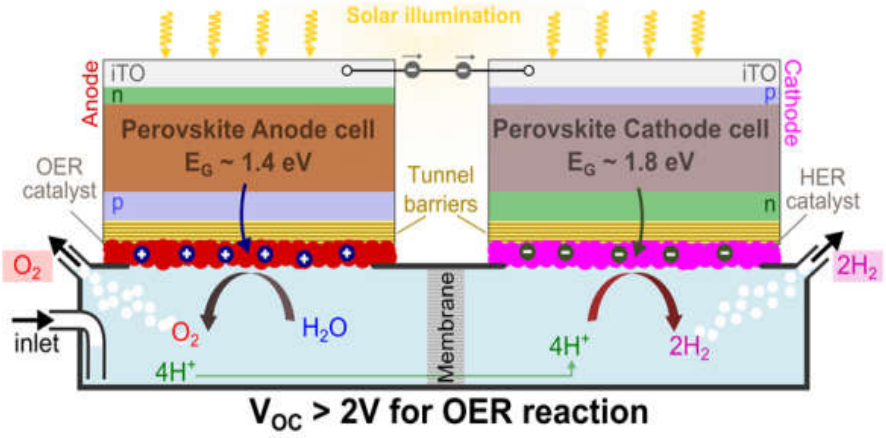

Figure 2. 16: Water splitting system structure based on perovskite solar cells [63].

2.7.6 Space applications

Solar cells for space applications have to be resistant to harsh environmental conditions (Figure 2.17). Especially, tolerance against radiation and charged particles is mandatory [64].

Low-energy protons can cause higher performance degradation than high-energy protons because they are more likely to be stopped in shallower regions. Nevertheless, flexible perovskite cells exhibited exceptional resistance (equating several years in space) and showed significant potential for power generation in space-related applications [64].

Recently, Olga et al. fabricated a flexible perovskite solar cells with $/ITO/PEDOT{:}PSS/perovskite/PCBM/BCP/metal\ configuration$. The solar cell irradiated with $100\ keV$ protons (fluence from $\sim 3 \times 10^{10}$ to $\sim 3 \times 10^{12}$ protons/cm^2, equating several years in space). Flexible PSCs exhibited a good radiation tolerance and did not show color center formation, revealing their outstanding resistance against low-energy proton radiation. They denoted that this can be credited to the combined effect of intrinsically large carrier diffusion length exceeding the thin absorber film thickness and the defect tolerance of perovskite crystals [64].

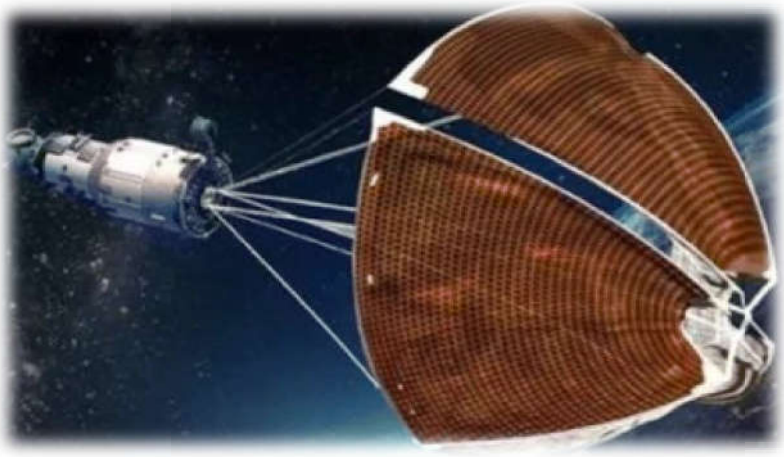

Figure 2. 17: Perovskite solar cells for space applications [64].

2.8 Perovskite Solar Cell Device Architecture

Perovskites solar cells have two main structures. In general, the most adopted structure by researchers all around the world is the "regular" structure. The regular perovskite solar cell is formed of a mesoporous oxide layer (as a wide band gap window layer), a lead halide layer penetrated into the porous of the oxide layer (as a light absorbing layer), hole transport material HTM (an efficient hole conductor) and an ohmic contact (as a hole collector) (Figure 2.18.a) [31].

Getting the mesoporous oxide layer thinner in regular structure until removing it eventually, led to another architecture of perovskite solar cells. Similar to inorganic thin film solar cells, the planar n-i-p heterojunction structure is comprised of a TCO cathode, an n type ETM, an intrinsic perovskite layer, a p type HTM and a metal anode (Figure 2.18.b).

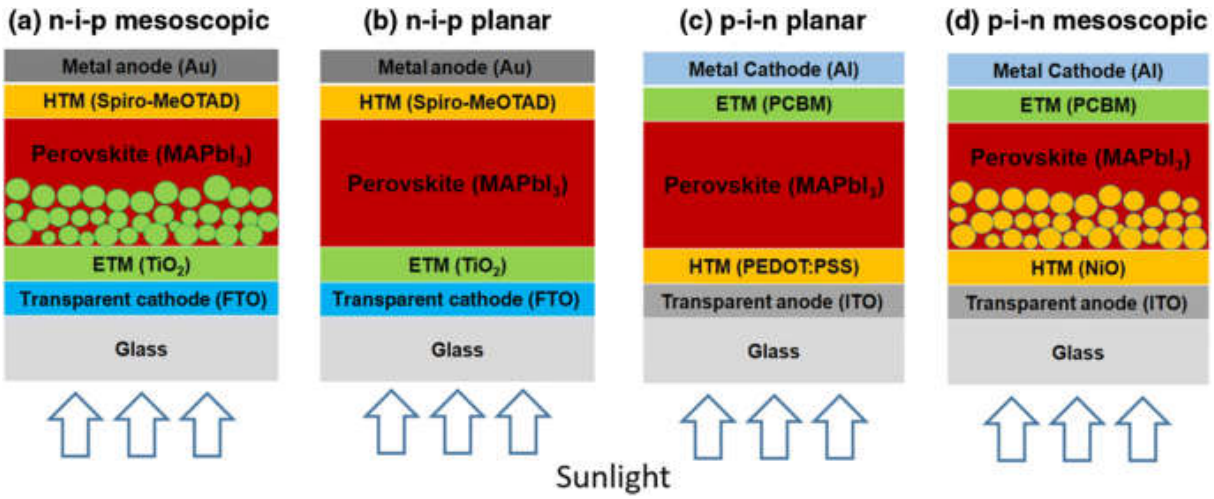

Figure 2. 18: Regular perovskite solar cell structures.

An opposite sequence of HTM and ETM configuration is used in planar p-i-n heterojunction structure (inverted structure).The p-i-n structure is comprised of a TCO anode, a p type HTM, an intrinsic perovskite layer, an n type ETM and a metal cathode.
The p-i-n heterojunction structure exhibited excellent photon to electron conversion rate and enhanced device stability maintained ~90 % in PCE after 30 days of exposure to ambient condition [32].

2.9 Working mechanisms of perovskite solar cells

Both mesoscopic and regular structures contain generally a thin compact TiO_2 layer, where photo-generated electrons in perovskites were injected through it. The balanced electron and hole diffusion lengths made $CH_3NH_3PbI_3$ material appropriate in p-n and p-i-n (or n-i-p) planar structures.

Certainly, perovskite provides electron and hole path-ways planar structure, while in the mesoscopic structure it provides electron and hole path-ways in both of perovskite and oxide layers (see Figure 2.19) [51].

Minemoto et al. [65] and Tanaka et al. [66-36] have observed that the dominant charge carrier in lead halide perovskite is a typical Wannier- type exciton. This is similar to the type of charge carriers observed in inorganic materials [65-66]. Therefore, lead halide perovskite solar cells (thin film and/or inert mesoporous configuration) operate generally as p–i–n (or n-i-p) junction [67].

The perovskite material serves as active layer (absorber), while the n-type material serves as the electron transporting material (ETM) and the p-type material as the hole transporting material (HTM). The photo-generated carriers at the –i- layer are then transported towards the contacts across the n and p layers [48].

Device structure affects working mechanism of the device. Also, the solar cell performance is dependent mainly on the quality of perovskite layer regardless on the device structure [51].

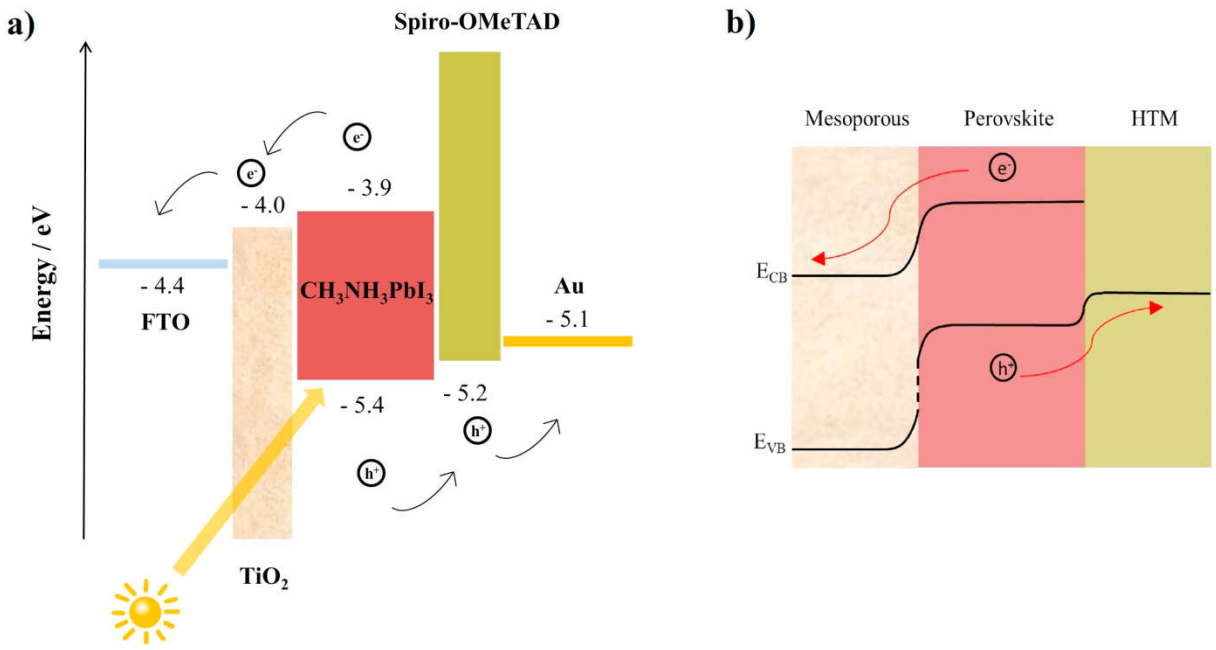

Figure 2. 19: Working mechanisms of perovskite solar cells.

2.10 Excitonic effects

Excitons are electron-hole pairs that are bound by coulombic interactions. Excitons existing in the semiconductors and insulators are created after absorbing photons by inter-band transitions. Where, the electron is in the conduction band (LUMO band) and the hole is in the valence band (HOMO band) [49]. Excitons have an important role in optoelectronic devices because they govern some characteristics of materials. There are two main types of excitons that have been identified in crystalline materials: Wannier-Mott and Frenkel excitons.

2.10.1 Wannier-Mott excitons

They are found in inorganic semiconductors which the dielectric constant is relatively large. Also, they are usually larger than single unit cells because of small coulombic interactions. Wannier-Mott excitons have a large Bohr radius (The distance between the electron and hole [68]) that encompasses many atoms which make it highly delocalized and can move freely throughout the crystal, hence they get the other name of "free" excitons as illustrated in Figure 2.20.a).

2.10.2 Frenkel excitons

These excitons are highly localized and they are comparable to a few unit cells in size in organic molecules (Figure 2.20.b). They have to move through the crystal by hopping from one atom site to another [49]. The Frenkel excitons have a much smaller Bohr radius which is comparable to the size of the unit cell.

In $CH_3NH_3PbI_3$ perovskites, because of the organic barriers, the excitons are confined in inorganic sheets. The Bohr radius is about a_B~0.05 nm [69] and the exciton binding energy has been calculated to be about 50 meV, but it could be even as low as 2 meV, indicating that at room temperature, and especially at the higher operating temperatures of a solar cell, the majority of charge carriers are free electrons and holes [70].

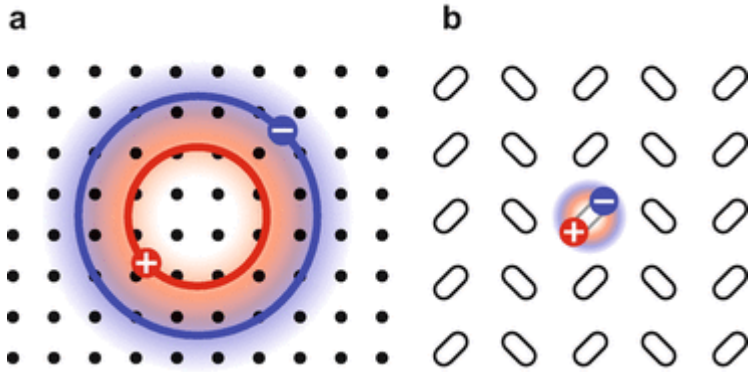

Figure 2. 20: Types of excitons in crystalline materials, (a) Wannier-Mott and (b) Frenkel excitons.

2.11 Challenges in perovskite solar cells

Two of the main issues for commercialization of perovskite photovoltaic technology are (i) strong current–voltage (J–V) hysteresis, (ii) relatively fragile stability of PSCs. These drawbacks will be discussed in next paragraphs.

2.11.1 Hysteresis of perovskite solar cells

The so-called current (J)–voltage (V) hysteresis is a mismatch of current measured between forward scan (voltage biased from 0 V to V_{oc}) and reverse scan (voltage biased from V_{oc} to 0 V) [71]. Consequently, the resultant photovoltaic parameters vary

depending on the direction and rate of the scan as shown in Figure 2.21 [72]. Therefore, hysteresis imposes a serious problem on determination of perovskite solar cell efficiencies and long term device operational stability [73].

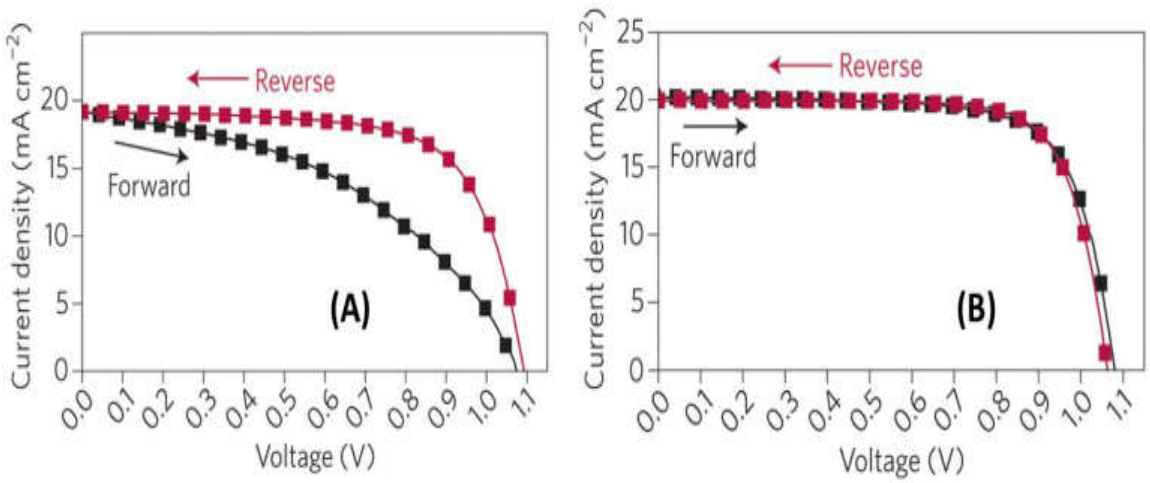

Figure 2. 21: (A) The current–voltage (I-V) response with hysteresis; and (B) negligible hysteresis of PSCs [74].

Many possible theories elucidating the origin or mechanism of hysteresis in PSCs have been proposed. These proposed origins are discussed in next paragraphs.

2.11.1.1 Trapping of electronic carriers at the perovskite interfaces

It is known that methods used in synthesis of perovskite materials create defects states within perovskite material. Also, migration of ions can create traps and lead to interfacial charge accumulation. Furthermore, it was revealed that all vacancies generate shallow traps or slightly perturbed states in the band and resonances (deep localized states hybridized with conduction or valence band states), indicating that carriers could still relax easily to VBM and CBM. Deep electronic states inside the band gap can be formed by interstitials and antisites associated with Pb and I. Reports have shown that grain boundaries and imperfections on the perovskite surface may introduce localized states, which could serve as trap centers for photogenerated carriers [72].

2.11.1.2 Ion migration

According to Frolova et al., $MAPbI_3$ perovskite represents an electrochemically active system with the mobile hydrogen (methylammonium) cations and iodine anions. Where

the perovskite films suffer from decomposition under the applied electric field, and the electrochemical degradation of the perovskite films is almost irreversible [68].

Migration of ions/vacancies under electric field through the perovskite layer plays an important role in the hysteresis. It was estimated that the motion of up to 3.7% of I with diffusion coefficient of $10^{-12}\text{cm}^2\text{s}^{-1}$ contributes to the hysteresis. Ion migration can cause the device degradation by reducing the built-in electric field which cannot be prevented by encapsulation [68].

2.11.1.3 Ferroelectric polarization

Theoretical calculations suggested the possibility of ferroelectricity of $MAPbI_3$ where the ferroelectric material is capable of sustaining a permanent polarization in the absence of an applied electric field. The existence of a polar molecule (organic cation) at the center of the perovskite cage has also been suggested to be one of the possible causes of orientational disorder and polarization [72].

2.11.1.4 Capacitive effects

The nature of charge distribution and kinetics of the charging processes are addressed by analyzing capacitive responses. Park and co-workers found that large $CH_3NH_3PbI_3$ crystal and presence of mesoporous TiO_2 significantly reduce the I–V hysteresis. They also reported that the capacitive charges tend to get stored in smaller crystals and planar structure. When the crystal size increases the chemical capacitance of the device increases [72].

Kim et al. reported that the normal structure with cp-TiO_2 and spiro-OMeTAD demonstrates severe I-V hysteresis, whereas the inverted planar layout with (PEDOT:PSS) and (PCBM) is a typical hysteresis-free structure showing almost no capacitive current at room temperature [74]. Also, they revealed that replacing both cp-TiO_2 and spiro-OMeTAD with other selective contact layers substantially reduce the capacitance along with a considerable shift of the electrode polarization domain toward higher frequency [74].

2.11.2 Degradation of perovskite materials

Degradation of perovskite materials is one of the most issues that affect existence, availability and commercialization of PSCs. Stability is evaluated as per standard of International Electrotechnical Commission damp heat test (at $85°C$, 85% relative humidity). Stable devices can maintain its performance with less than 10% reduction of PCE after 1000 h of exposure while PSCs can maintain only 80% of initial efficiency after 500 h [75].

The physical origin of the hysteresis was attributed to several processes which are discussed in following paragraphs and illustrated in Figure 2.22.

Perovskite decomposition represents electrolysis process producing H_2, CH_3NH_2 and PbI_2 (Figure 2.22). Where, oxidation of I^- anions (free or incorporated with PbI_3^-) liberates molecular iodine which can be trapped in the form of triodide (I_3^-) or partially evolve from the films (Equation 2.1). Simultaneously, reduction of hydrogen ions (individual or incorporated with MA^+) leads to releasing molecular hydrogen (Equation 2.2) [47].

Anode process:

$$2(PbI_2)^*I^- \longrightarrow 2PbI_2 + I_2 + 2e^- \qquad 2.1$$

Cathode process:

$$2(CH_3NH_2)^*H^+ + 2e^- \longrightarrow 2CH_3NH_2 + H_2 \qquad 2.2$$

Overall reaction:

$$2CH_3NH_3PbI_3 \xrightarrow{electrolysis} I_2 + H_2 + 2CH_3NH_2 \qquad 2.3$$

Furthermore, moisture has been proposed to be one of the most prominent factors for perovskite degradation. $MAPbI_3$ perovskite films usually change color from dark brownish to yellow when exposed to air, indicating degradation and PbI_2, CH_3NH_2 and HI were formed; in the presence of oxygen, HI could further degrade to iodine (I_2) and

H_2 by a redox reaction. Other factors were examined, such as oxygen, light illumination, and thermal stress [76].

Superoxide (O^{2-}) generated through electron transfer from $MAPbI_3^*$ to O_2attacks the perovskite absorber leading to the formation of methylamine (CH_3NH_2), lead iodide, iodine, and water as degradation products [77]. Under light illumination, PbI_2 could further decompose to generate I_2 [76]. Also, during annealing at 85 °C for a $MAPbI_3$ perovskite sample, it was found that $MAPbI_3$ decomposed to PbI_2 and I_2 [76].

Despite the solutions used to encapsulate and isolate the material from moisture, the material was still degrading. These studies strongly suggest that there could be a self-degradation pathway for perovskite solar cells [76].

Wang et al. reported that at room temperature the relatively high vapor pressure of I_2, is expected to diffuse easily to non-degraded perovskite regions just when it is generated. I_2 could also induce degradation of other iodide based perovskites (such as $FAPbI_3$ and $FA_{0.8}Cs_{0.2}PbI_3$), suggesting the generality of I_2-induced degradation [76].

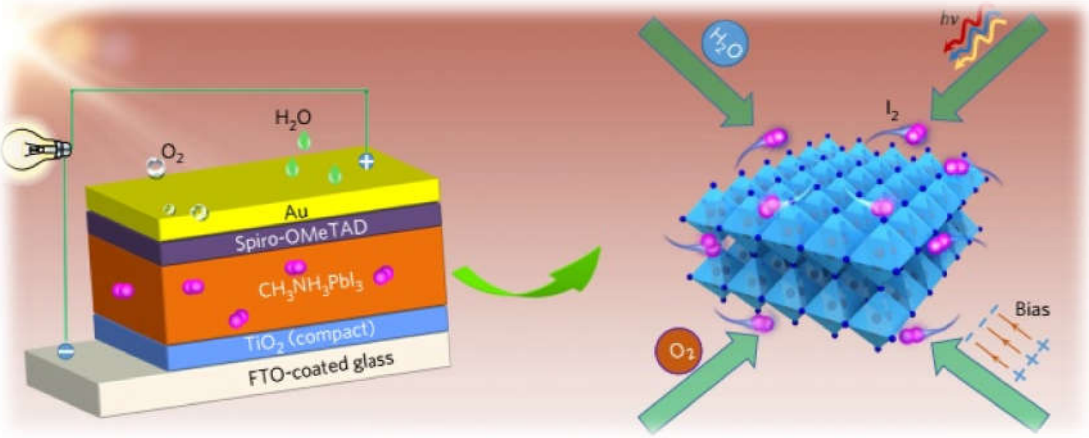

Figure 2. 22: Hysteresis factors of perovskite materials.

Chapter 3

Study and optimization of MAPbI perovskite solar cell

3.1 Introduction

Studying the behavior of real device or an imaginary system and analyzing it using computer application is based on mathematical model adapted to the studied system. Numerical modeling is now widely agreeable practice by scientific community. It simplifies understanding work principles of solar cells and also helps identification of the major parameters which affect the performance of the cell [78]. It also helps to reduce processing cost and time spent on solar cell device fabrication by providing useful information on how to vary the production parameters to improve the device performance.

Over the years several modeling tools specific to thin-film PV devices have been developed. A number of these tools have reached a mature status and are available to the PV community. Among them:

- **AMPS** (**A**nalysis of **M**icroelectronic and **P**hotonic **S**tructures), It is a one-dimensional (1D) device physics code which is applicable to any two terminal device including photovoltaic device. AMPS was developed by Prof. Stephen Fonash and a number of his students at The Pennsylvania State University [79].
- **wxAMPS** is an update of AMPS. The user interface of wxAMPS uses a cross-platform library and provides quick data entry and improved visualization. It is designed at the University of Illinois at Urbana Champaign, in collaboration with Nankai University of China [80].
- **PC1D** (**P**ersonal **C**omputer One **D**imensional) is very used in the simulation of solar cells. This software was developed in Australia at the university South Wales of Sydney. It allows simulating the behavior of photovoltaic devices based on semiconductor by respecting to one-dimensional (axial symmetry) [81].
- **AFORS-HET** (**A**utomat **For S**imulation of **Het**erostructures)is a one dimensional numerical computer program for modeling multi layer homo- or Heterojunction solar cells as well as some common solar cell characterization methods [79].
- **ASA**(**A**dvanced **S**emiconductor **A**nalysis) is designed for the simulation of devices based on amorphous and crystalline semiconductors. It has been developed by the group of Prof. Miro Zeman at the Technical University of Delft in the Netherlands [79].

- **SCAPS-1D** (**S**olar **C**ell **C**apacitance **S**imulator)is a one-dimensional solar cell simulation program developed at the Department of Electronics and Information Systems (ELIS) of the University of Gent, Belgium [82].

3.2 The basics of SCAPS-1D

SCAPS-1D has been developed to simulate the operation of thin-film solar cells. SCAPS is originally developed for cell structures of the $CuInSe_2$ and the CdTe family. Several extensions however have improved its capabilities so that it is also applicable to crystalline solar cells (Si and GaAs family) and amorphous cells (a-Si and micromorphous Si) [82]. SCAPS is a Windows-oriented program, which is opened with the 'Action Panel' (Figure3.1).

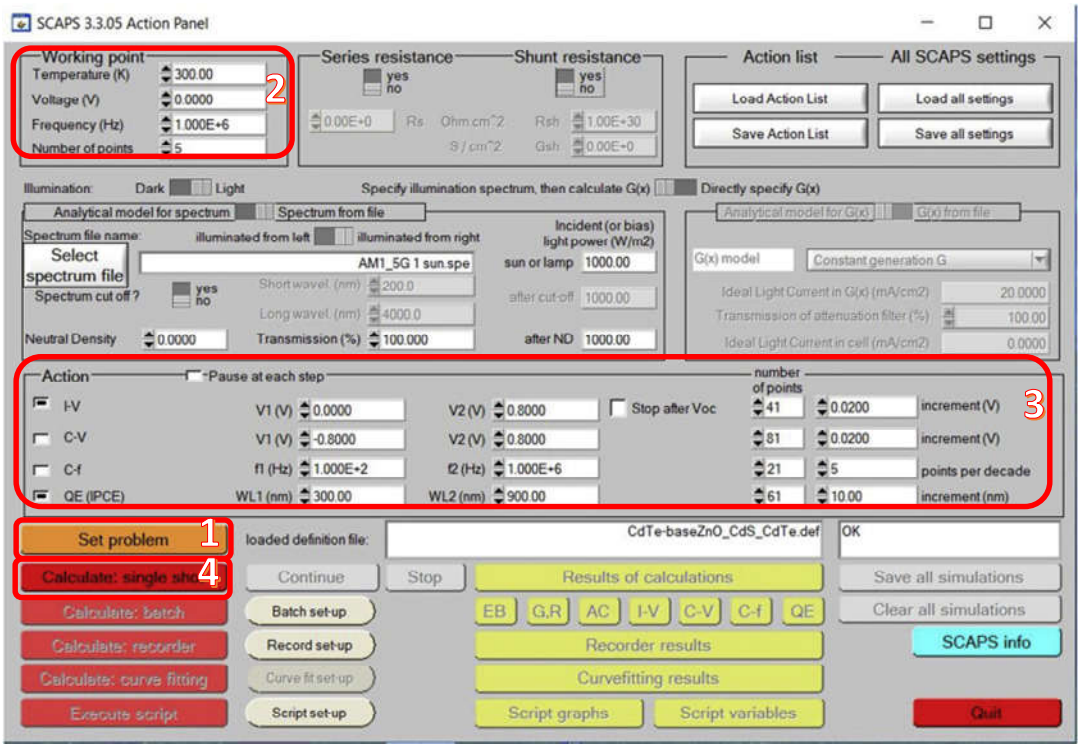

Figure 3. 1: The SCAPS start-up panel: the Action panel or main panel.

3.2.1 Definition of the problem

By clicking the button set problem (Figure 3.2.a) in the action panel, we can chose load in the lower right corner of the new opened panel (Figure 3.2.b) to select an example to study which can be modified in the cell properties [82].

Figure 3. 2: (a) Defining problem panel and (b) selecting an example.

3.2.2 Define the working point

The working point specifies the parameters which are not varied in a measurement simulation, and which are relevant to that measurement (Figure 3.3). Thus:

- Temperature (T): Necessary for all measurements.$N_c(T)$, $N_v(T)$, the thermal velocities, the thermal voltage $K_BT$and all their derivatives are the only variables which have anexplicit temperature dependence. These parameters must be inserted manually for each temperature [82].
- The voltage$V$: is unnecessary in $I-V$and $C-V$simulation, but it is taken as the dc-bias voltage in $C-f$ simulation and in $QE(\lambda)$ simulation. SCAPS always starts at 0 V, and proceeds at the working point voltage in a number of steps that also should be specified [82].
- The frequency f: is neglected in$I-V$, $QE(\lambda)$ and $C-f$simulation. But in $C-V$ measurement is taken into account [82].
- The illumination: is used for all measurements. For the $QE(\lambda)$ measurement, it determines the bias light conditions. The basis settings are: dark or light, choice of the illuminated side, choice of the spectrum. The default is one sun ($= 1000\ W/m^2$) illumination with the 'air mass 1.5, global' spectrum, but there is a large choice of monochromatic light and spectra for specialized simulations [82].

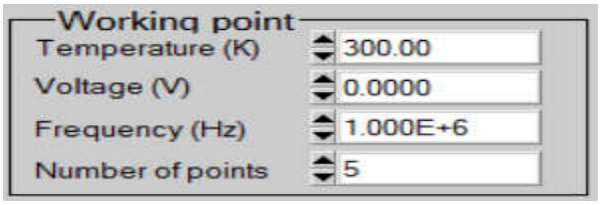

Figure 3. 3: Define the working point.

3.2.3 Selection of the measurement(s) to simulate

In the action-part of the Action Panel, the following measurements: $I-V$, $C-V$, $C-f$ and $QE(\lambda)$ can be simulated [82]. Adjust if necessary the start and end values of the argument, and the number of steps (Figure 3.4).

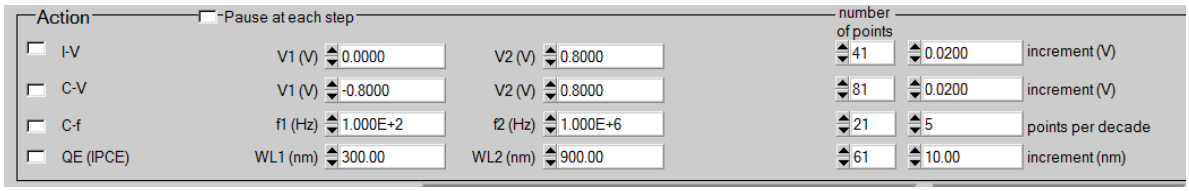

Figure 3. 4: Select the measurement(s) to simulate.

3.2.4 Starting the calculation(s)

By clicking the button calculate: single shot in the action panel. The Energy Bands Panel opens, and the calculations start. Meanwhile, SCAPS offers a free movie how the conduction and valence bands, the Fermi levels and the whole caboodle are evolving [82].

3.2.5 Displaying the simulated curves

After the calculation(s), SCAPS switches to the Energy band panel (or the AC-band panel) in which the band diagrams, carrier densities, current densities are shown. The results (buttons save graphs, show data (the numbers are shown on screen) or save data (the numbers are saved to a file). One of specialized output panels can be switched (Figure 3.5) [82].

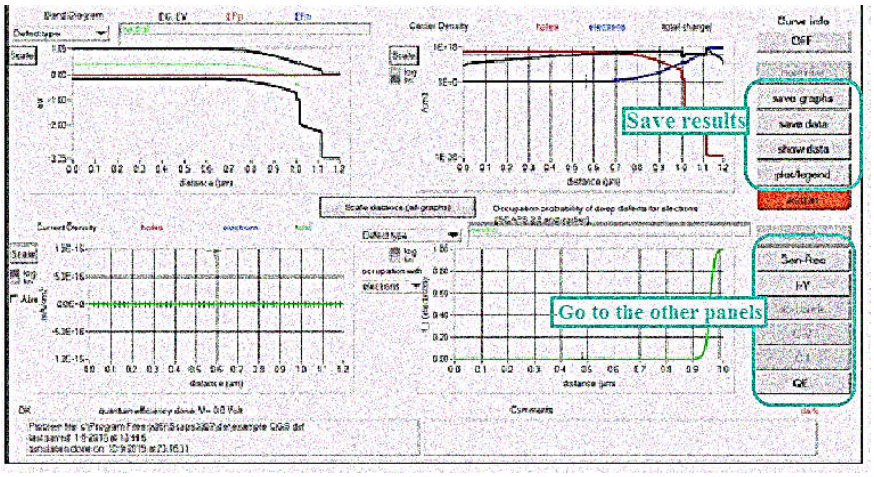

Figure 3. 5: Results panels.

Simulation procedure using SCAPS software can be summarized by the scheme presented in Figure 3.6.

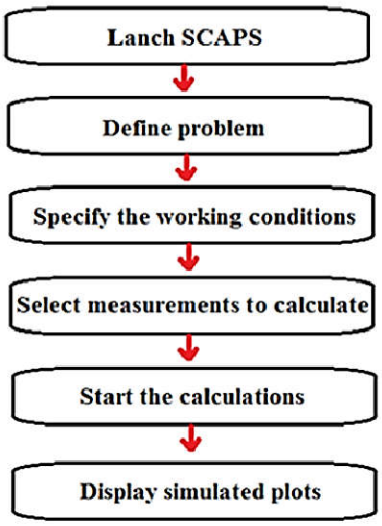

Figure 3. 6: Simulation procedure using SCAPS software.

3.3 Solar cell definition

Definition of the solar cell structure is done using graphical user interface (Figure 3.7.a). Layer, contact and interface properties can be edited in solar cell definition panel.

3.3.1 Editing a solar cell structure

The 'Solar cell definition' panel resulting in setting problem panel allows to create or edit solar cell structures and to save or load those from definition files [82].Layer properties are defined in layer panel where, it is impossible to define unrealistic situations (Figure 3.7.b).

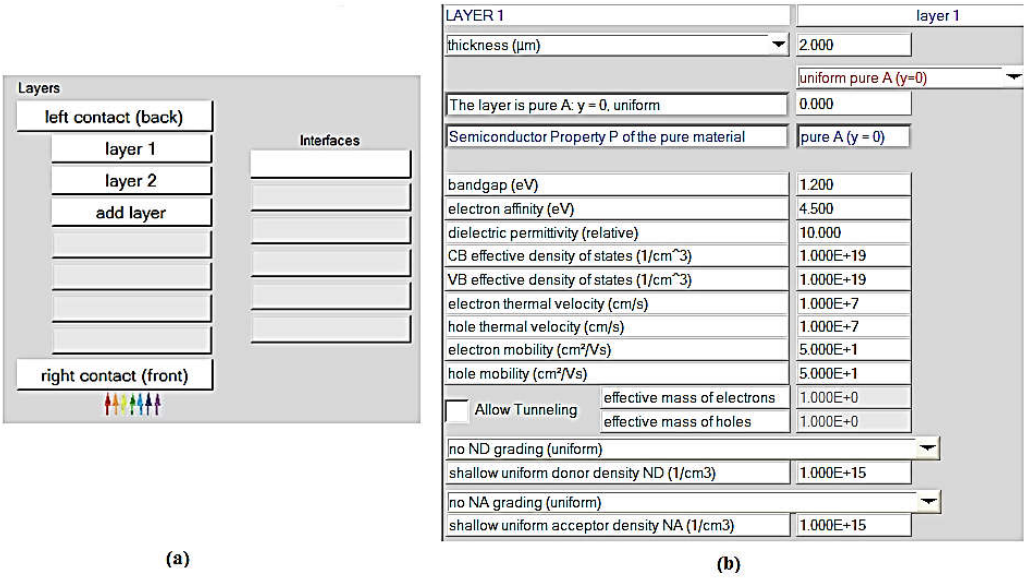

Figure 3. 7: Definition solar cell structure panel.

3.3.2 Reference Conventions for Illumination, Voltage and Current

The illuminated side and the applied voltage and current are optional as it is shown in Figure 3.8.Internally in SCAPS, only the default reference is used (voltage applied at the left contact, current reference arrow from left to right, resulting in a reference as a consumer) [82].

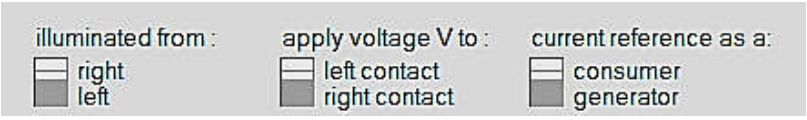

Figure 3. 8: Reference Conventions for illumination, voltage and current.

3.3.3 Contacts

The front and back contacts properties can be set by 'contact properties panel' (Figure 3.9). The metal work function Φ_m (for majority carriers) can be inputted. However, the option *"flat bands"* can be chosen. In this case, SCAPS calculates for every temperature the metal work function Φ_m in such a way that flat band conditions prevail. At the contacts a (wavelength dependent) reflection/transmission can be set. These can be set either as a constant value (wavelength independent) or as a filter file. These filter files are standards provided with SCAPS installation or can be constructed [82].

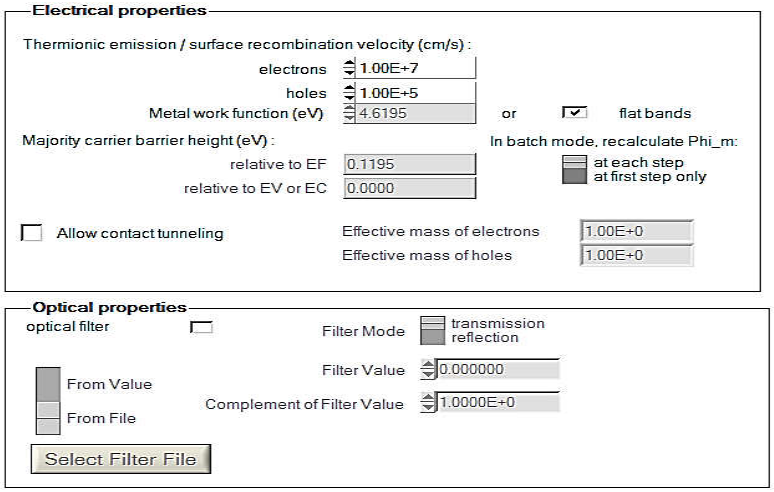

Figure 3. 9: Contact properties panel.

3.3.4 The optical absorption constant $\alpha(\lambda)$ or $\alpha(h\nu)$ of a layer

The optical absorption constant determines to what extent a particular wave length penetrates into material. Light is poorly absorbed in the material when the absorption coefficient is low and vice versa. Since the absorption coefficient curve of semiconductors has a sharp edge, the light with energy below the band gap will not be absorbed and the electron can't be excited to the conduction band [5].

The absorption of such layer can be set from a file or from a model used by SCAPS simulator (Figure 3.10). When it is set from a model, the absorption coefficient $\alpha(\lambda)$ is given by Equation 3.1

$$\alpha(h\nu) = \left(\alpha_1 + \beta_1 \frac{E_{g1}}{h\nu}\right) . \left(\frac{h\nu}{E_{g1}} - 1\right)^n \quad 3.1$$

$h\nu$ is the photon energy and E_g the band gap.α_1 and β_1 are the model parameters (have the dimension of absorption constant ($1/cm$ or $1/m$) regardless of the value of the exponent n) [83].

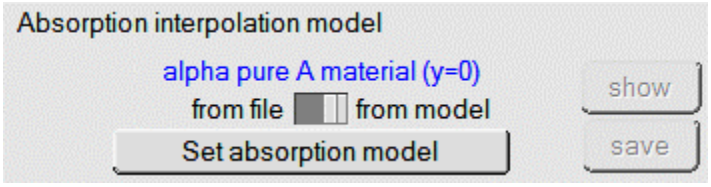

Figure 3. 10: Optical absorption constant of a layer.

3.4 Principal of Numerical Simulation

Researches in physics of devices based on semiconductors led to the realization of a mathematical model. This model is capable to operate in virtually any device based on semiconductor. It consists of a fundamental caboodle of equations which gather the electrostatic potential and density of charge carriers in well specified domain of simulation [28]. These equations are derived from Maxwell equations [84].

3.4.1 Poisson's equation

Poisson equation which presents the relationship between electric field of a p-n junction (E) and the space charge density (ρ) is given by Equation 3.2:

$$div(\varepsilon \mathrm{E}) = \rho \quad 3.2$$

Where, the electric field is given by:

$$E = -grad(\psi) \quad 3.3$$

From Equations 3.2 and 3.3:

$$\frac{\partial^2 \psi}{\partial^2 x} = -\frac{\partial E}{\partial x} = -\frac{\rho}{\varepsilon} = -\frac{q}{\varepsilon}[p - n + N_D^+(x) - N_A^-(x) \pm N_{def}(x)] \quad 3.4$$

Where, ψ is the electrostatic potential,q is elementary charge,ε is the electric permittivity ($\varepsilon = \varepsilon_0 \varepsilon_r$, ε_0 is the vacuum permittivity and ε_r is the substance permittivity), n(p) is the electron (hole) density, $N_D^+(N_A^-)$ is the density of ionized donors (acceptors) and $N_{def}$is the possible defect (Acceptor or donor) density [85].

3.4.2 Continuity equations

The continuity equations describe the variation speed of density of carriers in function of time. These equations are in two folds, electrons and holes equations. And they are given by Equation .3.5 and 3.6 [28]:

For electrons:

$$\frac{\partial n}{\partial t} = \frac{1}{q} div J_n + G_n - R_n \qquad 3.5$$

For holes:

$$\frac{\partial p}{\partial t} = -\frac{1}{q} div J_p + G_p - R_p \qquad 3.6$$

G_n and G_p are generation rates of electrons and holes by external agents. R_n and R_p are recombination rates (interne) of electrons and holes, respectively. J_n and J_p are current density of electrons and holes [85].

3.5.3 Carrier transport equations

There are two main carrier transport mechanisms in semiconductor devices which are Drift and Diffusion. This movement of charge carriers generates current in the device.

Drift current is the current generated by the movement of charge carriers due to an applied electric field E (first term in Equations 3.7 and 3.8), and diffusion current is due the diffusion of charge carriers (second term in Equations 3.7 and 3.8) [28]:

$$J_n = qn\mu_n E + qD_n \frac{dn}{dx} \qquad 3.7$$

$$J_p = qp\mu_p E - qD_p \frac{dp}{dx} \qquad 3.8$$

Where,D_n, D_p , μ_n and μ_p are the coefficient of diffusion and mobilities of electrons and holes, respectively [28].

In this study, a one-dimensional modeling of conventional and inverted perovskite solar cells was performed using SCAPS simulator (version 3.3.07).This work is focused on designing a $CH_3NH_3PI_3$ perovskite based solar cell and extracting its output

parameters. Moreover, it studied the effect of changing electron and hole transport layers (ETL and HTL, respectively), on the performance of the cell. We did not take into account the effects of reflection on the front and back surfaces, series resistance and shunt resistance. The simulation is performed at AM1.5G solar spectrum with an incident power density of 100 mW/cm^2 at room temperature (300 K).

3.6 Device structure

The designed solar cell using SCAPS simulator is illustrated in Figure 3.11. Where the chosen structures are n-i-p and p-i-n planar architectures, and the input parameters of each layer are summarized in Table1. With 0.05 µm of n type electron transport layer (Indium tin oxide ITO) and 0.05µm of p type hole transport layer [$PEDOT:PSS$ (Poly(3,4-ethylenedioxythiophene)-poly(styrene sulfonate))] and 0.4 µm of intrinsic perovskite ($CH_3NH_3PI_3$). The conventional (n-i-p) and converted (p-i-n) solar cells are represented in Figure 3.11with FTO/ITO/Perovskite/PEDOT:PSS/Au and FTO/PEDOT:PSS/Perovskite/ITO/Au configurations, respectively.

Figure 3. 11: Solar cell structures (n-i-p at left and p-i-n at right).

3.7 Absorption coefficient of MAPbI perovskite material

According to P. Löper and co-workers [86], the most prominent feature in the optical spectra of MAPbI perovskite materials is the well known absorption edge at ~ 1.55 eV, seen as a sharp drop in transmittance at a wavelength of ~ 800 nm. The absorption coefficient of perovskite material was extracted from [86] and plotted in Figure 3.12.

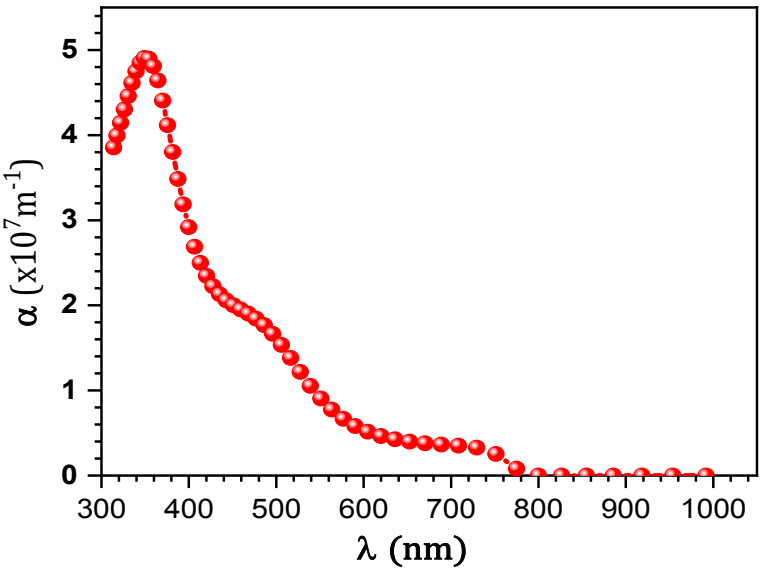

Figure 3. 12: Absorption coefficient of $CH_3NH_3PbI_3$ perovskite.

3.8 The layers input parameters

The input parameters of ITO are extracted from the work of Pandey et al.[87] while, the perovskites and PEDOT:PSS parameters are taken from the work of Minemoto et al. [88] and Mandadapu et al. [89], respectively. These parameters are summarized in Table 3.1:

Parameter	Term	ETM (ITO)[87]	Perovskite[88]	HTM (PEDOT:PSS)[89]
$d(\mu m)$	*Thickness*	0.05	0.4	0.05
$E_g(eV)$	*Band gap*	3.65	1.55	2.20
$\chi\ (eV)$	*Affinity*	4.8	3.9	2.9
ε_r	*Permittivity*	8.9	6.5	3.00
$N_c\ (cm^{-3})$	*Effective density of states at CB*	5.8×10^{18}	2.2×10^{18}	2.2×10^{15}
$N_v\ (cm^{-3})$	*Effective density of states at VB*	1×10^{18}	1.8×10^{19}	1.8×10^{18}
$\mu_n\ (cm^2/V\,s)$	*Mobility of electrons*	10	2	2×10^{-2}
$\mu_p\ (cm^2/V\,s)$	*Mobility of holes*	10	2	2×10^{-4}
$N_d\ (cm^{-3})$	*Density of n-type doping*	1×10^{20}	5.21×10^{9}	0.0
$N_a\ (cm^{-3})$	*Density of p-type*	0.0	5.21×10^{9}	3.17×10^{14}

	doping			
N_t (cm^{-3})	*Density of defects*	1×10^{19}	2.5×10^{13}	1×10^{15}

Table 3. 1: Device parameters used in simulation.

3.9 MAPbI Perovskite Solar cell performance

As mentioned in the previous section, the one-dimensional modeled n-i-p and p-i-n planar perovskite solar cells were simulated under AM1.5G solar spectrum with an incident power density of 100 mW/cm^2 at room temperature (300 K). The extracted current-voltage characteristic was calculated from 0 V to 1.3 $V$and the quantum efficiency from 360 nm to900 nm. Effects of reflection on the front and back surfaces, series resistance and shunt resistance were neglected.

3.9.1 The band gap energy diagram at equilibrium

The band diagrams of the n-i-p and p-i-n PSC at equilibrium are shown in Figures3.13. In the conventional PSC, an energy barrier of 0.9 $eV$is present between the conduction band minimum (E_c) of the ITO and the lowest unoccupied molecular orbital (LUMO) of the absorber $CH_3NH_3PbI_3$ material, and an offset about 0.35 eV between the highest occupied molecular orbitals (HOMO) of both absorber material and HTL. However, in inverted PSC, an offset about 0.34 eV formed between Ev of HTL and HOMO of the absorber material and an energy barrier of 0.76 eV is between E_c of ETL and LUMO of the absorber.These bands alignment led to poor performance of the modeled solar cells.

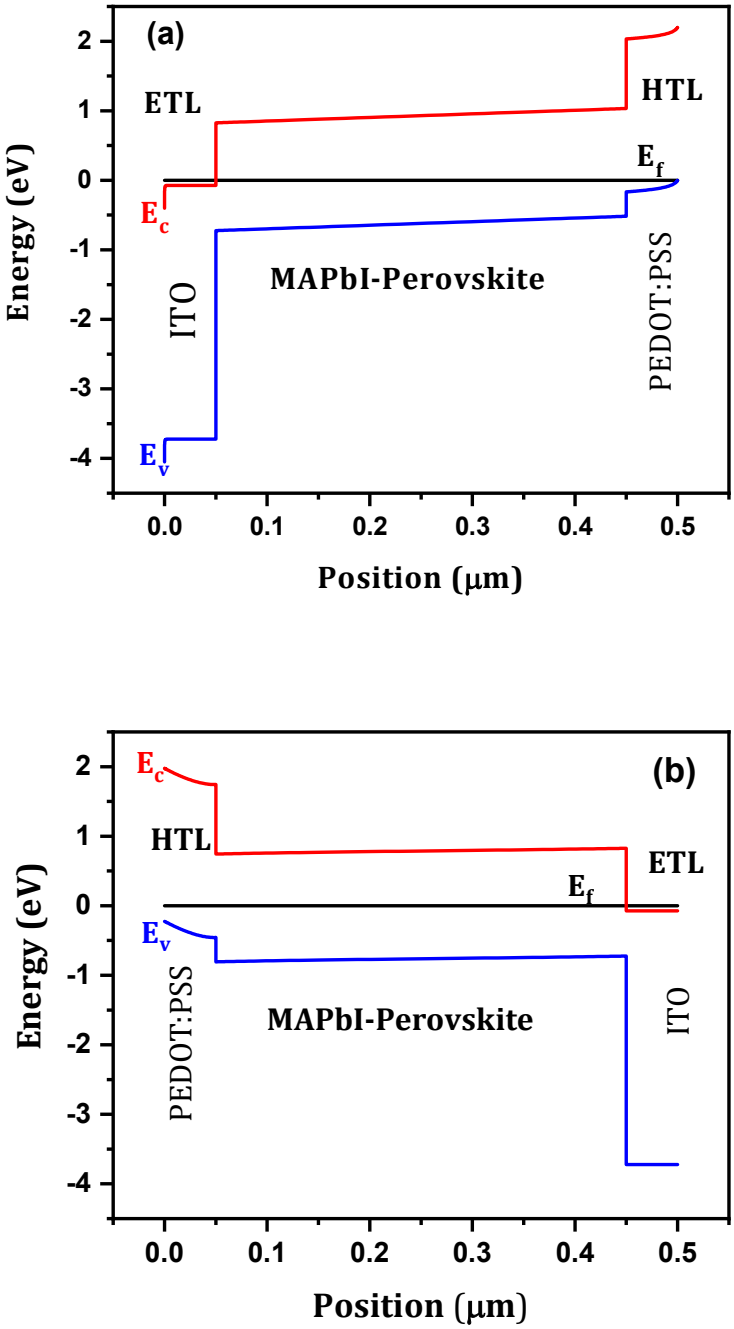

Figure 3. 13: Energetic band diagram of: (a) conventional n-i-p and (b) inverted p-i-n; perovskite solar cell.

3.9.2 The Current density-Voltage characteristic

The obtained current density-voltage characteristic curves and external quantum efficiency are shown in Figures 3.14 and 3.15, respectively. The extracted electrical

output parameters of the conventional solar cell are inserted in Figure 3.15. The cell exhibited a lightly low fill factor (~50.09 %)but a good short circuit current $J_{sc} = 21.87\ mA/cm^2$ and a remarkable open circuit voltage $V_{oc} = 1.27\ V$(compared to the band gap energy 1.55 eV of the absorber layer). These extracted parameters gave a power conversion efficiency of ~13.94 %.

A suitable quantum efficiency of ~70 – 87 % is obtained in the visible range and is related to the good current density $J_{sc} = 21.87\ mA/cm^2$.

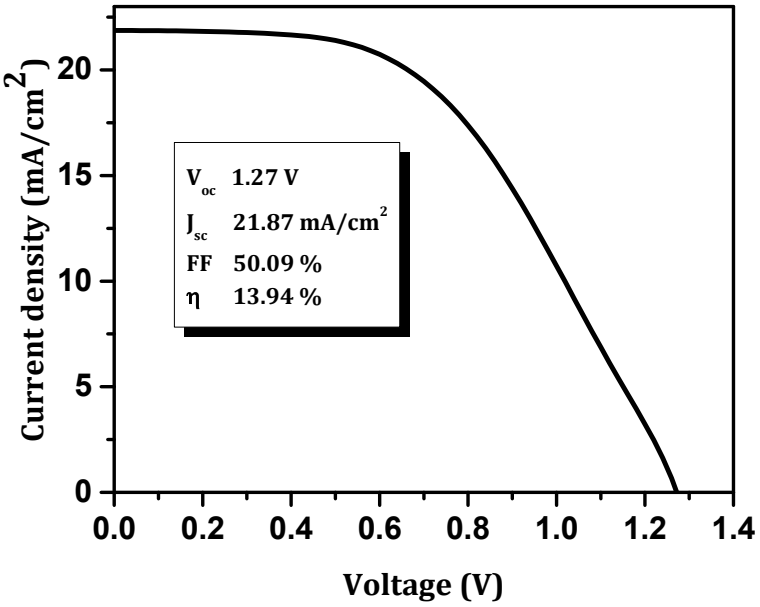

Figure 3. 14: Current density- Voltage characteristic of conventional PSC.

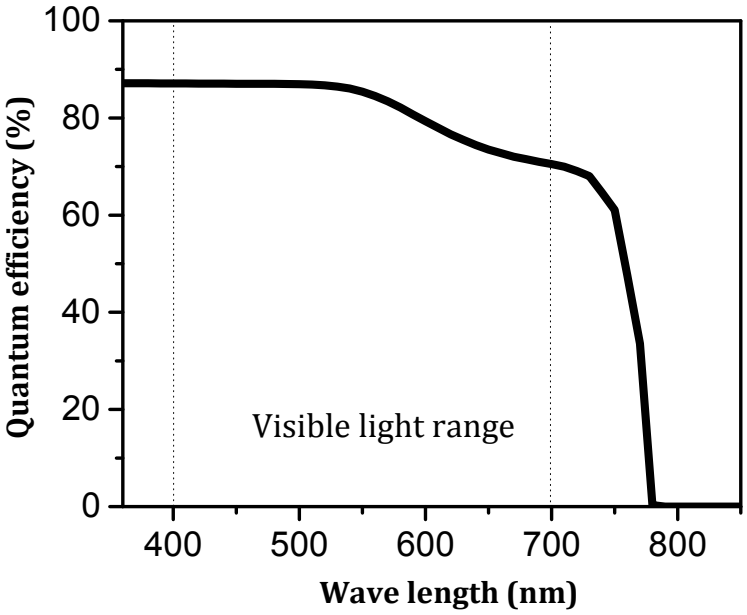

Figure 3. 15: Device quantum efficiency characteristic of conventional PSC.

For the inverted perovskite solar cell, the extracted electrical output parameters are inserted in Figure 3.16. Also, this cell exhibited a low fill factor (~39.57 %) but a good short circuitcurrent $J_{sc} = 21.83\ mA/cm^2$ and a notable open circuit voltage $V_{oc} = 1.27\ V$. These extracted parameters gave a power conversion efficiency of ~10.99 %.

Particularly striking in both solar cells is the remarkably high open-circuit voltage V_{oc} (up to $1.27\ V$) compared with its bandgap E_g (~ $1.55\ eV$). Quite generally, the bandgap-voltage offset $\{(E_g/q) - V_{oc}\}$, where q is the elementary charge, is a useful measure to assess the electronic quality of the absorber in the solar cell [90]. The small difference between E_g/q of the absorber material and V_{oc} of the corresponding solar cell indicates a low non-radiative recombination and long diffusion lengths of charge carriers due to the low exciton bounding energy [32].

An acceptable quantum efficiency of $\sim 62 - 74$ % is obtained in the visible range (Figure 3.17).

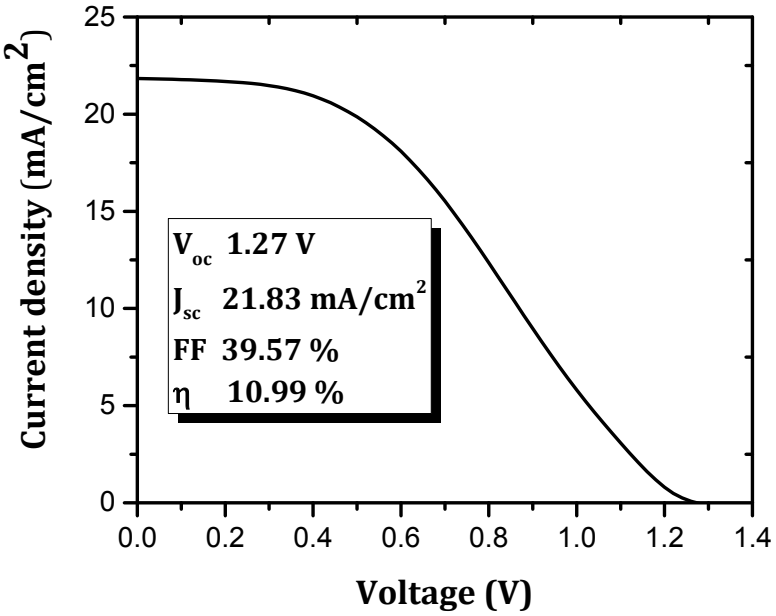

Figure 3. 16: Current density- Voltage characteristic of inverted PSC.

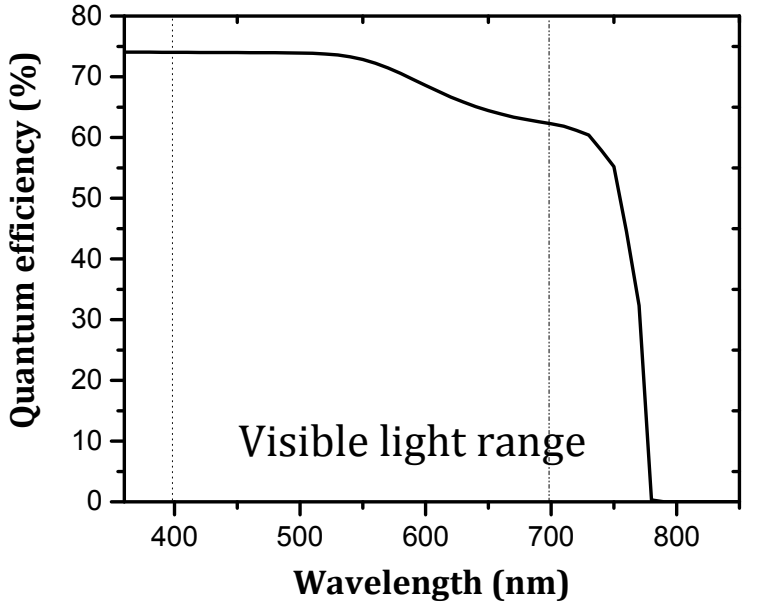

Figure 3. 17: Device quantum efficiency characteristic of inverted PSC.

The low doping density of $PEDOT:PSS$ ($10^{14} cm^{-3}$) lead to an increased depletion region at HTL of the device (which is a thin layer).This phenomena produces a bulk resistance of the p type material and an interfacial contact resistance between rear contact and the p type layer.

This effect can be observed by the deviation of the J-V curve from the quadratic shape of an ideal solar cell J-V characteristic.

However, the strong acidity of PEDOT:PSS used in solar cells as an (HTL) material can cause the degradation of the close perovskite or electrode and lead to inferior perovskite crystal quality [41-91]. Furthermore, the hygroscopic PEDOT:PSS attracts ambient humidity and enables its diffusion under the electrodes. The release of this absorbed water towards the highly reactive metal cathode leads to the rapid oxidation of the cathode [92].

On the other hand, the ITO has disadvantages should be taken into the consideration; the price, the brittleness (which is an issue for flexible devices) and the possibility of indium's diffusion into organic materials. These drawbacks are strong reasons to find alternative transparent electron transport materials [93].

As a solution for these issues, alternatives of the ETL and the HTL are studied to improve the performance of these solar cells.

3.10 Effect of electron transport layer

In this section the aim is to obtain a better performance of the perovskite solar cell with n-i-p and p-i-n structures and to determine suitable materials working as an electron and hole transport layers (ETL and HTL, respectively).

3.10.1 Input parameters of ETL materials

In this part, a 0.05 μm of organic fullerene derivative [6,6]-phenyl-C_{61}-butyric acid methyl ester ($PCBM$), indium gallium zinc oxide ($IGZO$), tin dioxide (SnO_2), titanium dioxide (TiO_2) and zinc oxide (ZnO) are used as an ETL, respectively.; and compared to the solar cell with ITO window layer. The input parameters of these materials are summarized in Table 3.2.

Parameters	$PCBM$ [94]	$IGZO$[95]	SnO_2[89]	TiO_2[88]	ZnO[87]
$E_g(eV)$	2	3.05	3.5	3.2	3.3
$\chi\ (eV)$	3.9	4.16	4	3.9	4.1
ε_r	3.9	10	9	9	9
$N_c\ (cm^{-3})$	2.5×10^{21}	5×10^{18}	2.2×10^{17}	1×10^{21}	4×10^{18}

$N_v\ (cm^{-3})$	2.5×10^{21}	5×10^{18}	2.2×10^{16}	2×10^{20}	1×10^{19}
$\mu_n(cm^2/Vs)$	0.2	15	20	20	100
$\mu_p(cm^2/Vs)$	0.2	0.1	10	10	25
$N_d\ (cm^{-3})$	2.93×10^{17}	1×10^{18}	1×10^{17}	1×10^{19}	1×10^{18}
$N_a\ (cm^{-3})$	0.0	0.0	0.0	1.0	1×10^{5}
$N_t\ (cm^{-3})$	1×10^{15}	1×10^{15}	1×10^{15}	1×10^{15} neutral	2×10^{17} Donor, uniform 1.7 eV above E_v

Table 3. 2: Electron transport materials parameters for simulation.

3.10.2 Current density- Voltage characteristic

The obtained J-V characteristic and quantum efficiency of n-i-p PSC are shown in Figures 3.18 and 3.19 respectively; and the extracted output parameters are summarized in Table 3.3.

According to the obtained results for the conventional solar cell, the $PCBM$ material presents the lowest current density J_{sc}~18.47 mA/cm^2compared to the other materials and lowest quantum efficiency (QE). This performance may be due to its low electron and holes mobilities ($2\times10^{-1}cm^2/Vs$) which affect the charge collection. On the other hand, the $PCBM$ exhibited the highest fill factor ($FF\sim 74.98\ \%$) and a high $V_{oc} = 1.26\ V$.These parameters lead to a power conversion efficiency of 17.39 %.

The indium gallium zinc oxide ($IGZO$) and tin dioxide (SnO_2) showed acceptable and comparable improvement in the efficiency (19.51% and 19.88%, respectively) and a high QE. It is known that the power conversion efficiency is defined by:

$$\eta = (V_{oc}\times J_{sc}\times FF)/P_{in} \qquad 3.9$$

Where P_{in} is the incident power, and both of$IGZO$ and SnO_2 have almost the same values of open circuit voltage, short circuit current density and fill factor ($V_{oc}\sim 1.27\ V$, $J_{sc}\sim 21\ mA/cm^2$and $FF\sim71\%$). These close values led to conversion efficiency of about 19%.

Zinc oxide (ZnO) and titanium dioxide (TiO_2) seem to be the best candidates for ETL. With an optimum compromise between the three extracted output parametersJ_{sc}, V_{oc}, FF, the ZnO and TiO_2 ETL give a better conversion efficiency of about 20%. This is probably due to the adequate bands alignment between the conduction band of $ZnO$and $TiO_2$and the LUMO of the perovskite as presented in Figure 3.22. Also, noting that some of their input parameters seem to be similar. For example, mobility of electrons is greater in zinc oxide than in titanium dioxide (100 cm^2/Vs and20 cm^2/Vs, respectively). But, this has been compensated by the defects density which is greater in zinc oxide than in titanium dioxide ($2\times10^{17}cm^{-3}$ and $1\times10^{15}cm^{-3}$, respectively).

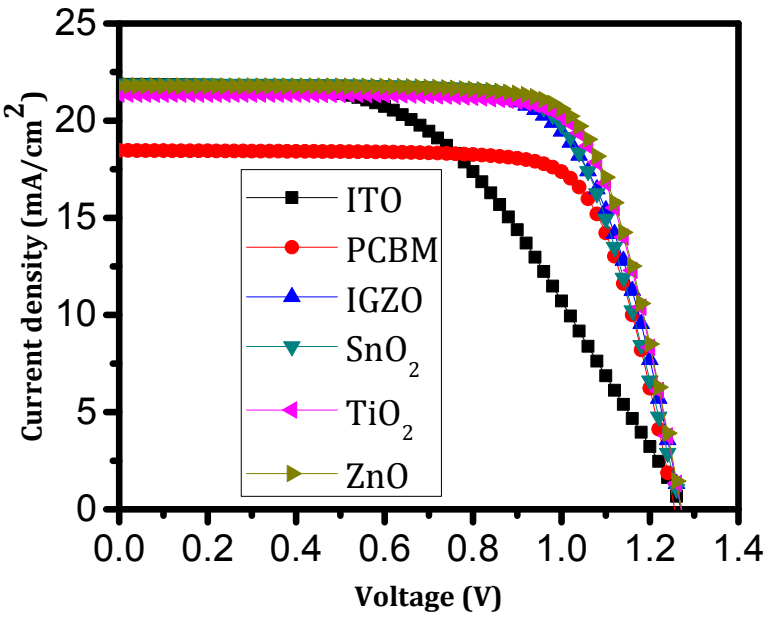

Figure 3. 18: Effect of ETL layer on Current density-Voltage characteristic for n-i-p PSC.

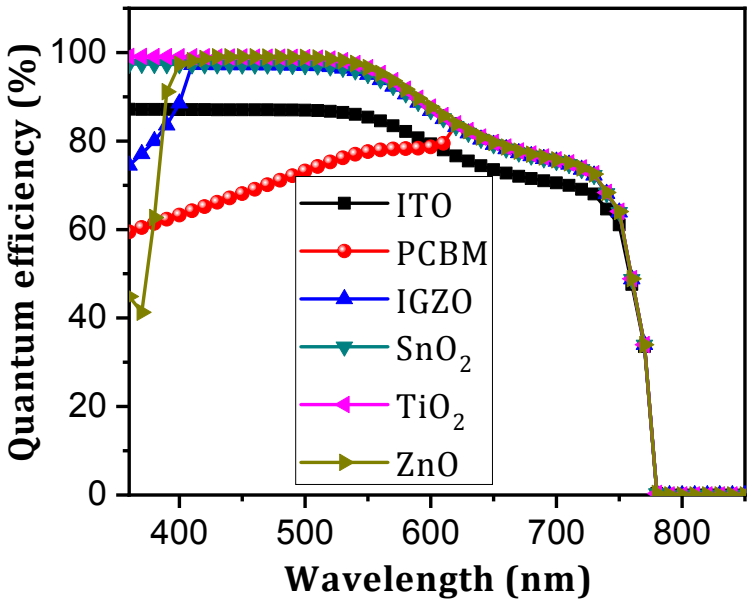

Figure 3. 19: Effect of ETL on quantum efficiency for n-i-p PSC.

Parameter	ITO	PCBM	IGZO	SnO_2	TiO_2	ZnO
$V_{oc}(V)$	1.27	1.26	1.27	1.27	1.27	1.27
$J_{sc}(mA/cm^2)$	21.87	18.47	21.59	21.89	21.36	21.78
FF (%)	50.09	74.98	71.08	71.43	74.66	74.53
η (%)	13.94	17.39	19.51	19.88	20.26	20.64

Table 3. 3:Effect of ETLs on output parameters for n-i-p PSC.

As for the inverted structure, all the ETL materials exhibited close values of open circuit voltages (Voc~1.27 eV)and current densities (Jsc~21.9$mA/cm2$) but different fill factors and power conversion efficiencies (Figure 3.20). Obtained output parameters were summarized in Table 3.4. The$IGZO$ material showed the lowest power conversion efficiency of 16.3%, and lowest quantum efficiency (QE) (Figure 3.21).

$SnO_2, PCBM, ZnO$ and TiO_2 showed acceptable and comparable improvement in the efficiency (~19.20%) and a high QE.

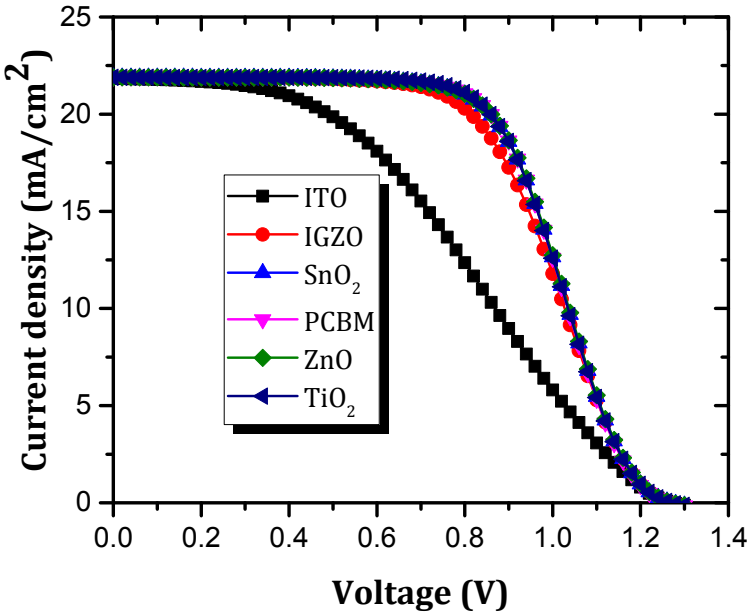

Figure 3. 20: Effect of ETL layer on Current density-Voltage characteristic for p-i-n PSC.

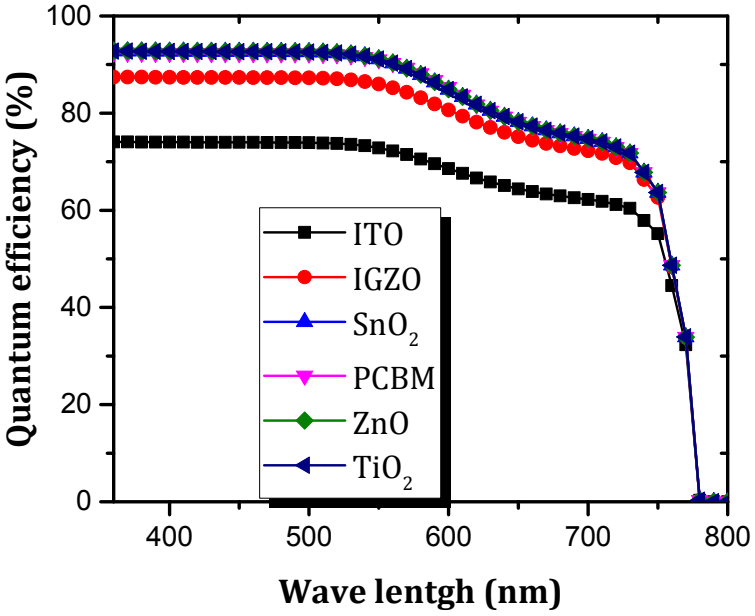

Figure 3. 21: Effect of ETL on quantum efficiency for p-i-n PSC.

Figure 3.20 shows a decline in ZnO quantum efficiency at wave lengths $\lambda < 400\ nm$ for the conventional solar cell. This may be explained by a considerable recombination at the front surface (i.e. high defects density $10^{17} cm^{-3}$) which affects the "violet and ultraviolet" portion of the spectrum, where charge carriers are not able to move into an

external circuit. But this decline is not existed in inverted solar cell's quantum efficiency because it is in the back of the device.

Parameter	ITO	$IGZO$	SnO_2	$PCBM$	ZnO	TiO_2
$V_{oc}(V)$	1,27	1,27	1,27	1,27	1,27	1,27
$J_{sc}(mA/cm^2)$	21,83	21,89	21,89	21,93	21,89	21,89
FF (%)	39,57	58,55	61,69	61,86	61,79	61,90
η (%)	10,99	16,30	17,16	17,20	17,20	17,21

Table 3. 4: Effect of ETLs on output parameters for p-i-n PSC.

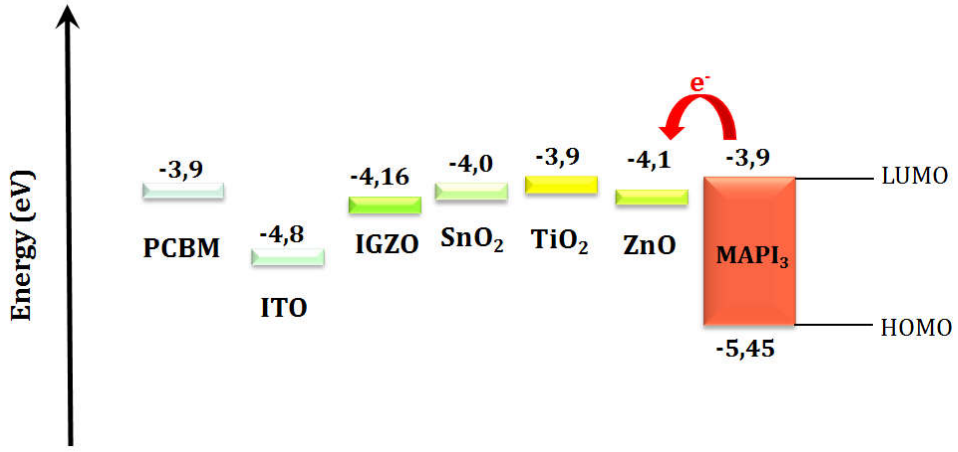

Figure 3. 22: Bands alignment between ETL materials and perovskite.

Therefore, in conventional and inverted PSC the appropriate materials that could be used as an electron transport layer are titanium dioxide (TiO_2) and zinc oxide (ZnO).

3.11 Effect of the hole transport layer

After determining the optimum materials working as window and electron transport layer which are TiO_2 and ZnO, the hole transport layer was changed to determine the appropriate p type material working as a hole transporter. A $FTO/\boldsymbol{ETL}/Perovskite/\boldsymbol{HTL}/Au$ and $FTO/\boldsymbol{HTL}/Perovskite/\boldsymbol{ETL}/Au$ configurations using ZnO than TiO_2as an ETL were optimized. A number of organic and inorganic materials are investigated as HTL. A 0.05µm of:$P3HT$[poly(3-hexylthiophène-2,5-diyl)], $Spiro-OMeTAD$ (2,2',7,7'-

tetrakis-(N,N-di-p-methoxyphenyl-amine)-9,9'-spirobifluorene)] , $CuSCN$ [Copper(I) thiocyanate], CuI [Copper(I) iodide] and NiO [Nickel (II) Oxide] are used as a hole transport materials.

3.11.1 Input parameters of HTL materials

The input parameters of these organic and inorganic materials are summarized in Table 3.5.

Parameter	$Spiro-OMeTAD$[88]	$P3HT$[96]	CuI[97]	NiO[98]	$CuSCN$[48]
$E_g(eV)$	3.00	1.85	2.98	3.6	3.4
$\chi\ (eV)$	2.45	3.1	2.1	1.46	1.9
ε_r	3.00	3.4	6.5	11	10
$N_c\ (cm^{-3})$	1×10^{19}	1×10^{22}	2.8×10^{19}	1.6×10^{19}	1.7×10^{19}
$N_v\ (cm^{-3})$	1×10^{19}	1×10^{22}	1×10^{19}	1.1×10^{19}	2.5×10^{21}
$\mu_n(cm^2/Vs)$	2×10^{-4}	1×10^{-4}	1.7×10^{-4}	50	1×10^{-4}
$\mu_p(cm^2/Vs)$	2×10^{-4}	1×10^{-3}	2×10^{-4}	50	1×10^{-1}
$N_d\ (cm^{-3})$	0.0	0.0	0.0	0.0	0.0
$N_a\ (cm^{-3})$	2×10^{18}	3.17×10^{13}	1×10^{18}	1.8×10^{18}	1×10^{18}
$N_t\ (cm^{-3})$	1×10^{15}	1×10^{14}	1×10^{15}	1×10^{14}	1×10^{14}

Table 3. 5: Input parameters of the proposed HTL materials.

3.11.2 Current density-Voltage characteristic

Since the best performance is obtained for conventional PSC based on ZnO as an ETL, the suitable materials used for conventional and inverted PSC as an HTL are studied in this section.

By using 0.05 μm of zinc oxide as an ETL in conventional and inverted PSC then changing hole transport materials, the obtained J-V characteristic curves and quantum efficiency of n-i p PSC are presented in Figures 3.23 and 3.24, respectively. The obtained J-V characteristic curves and quantum efficiency of p-i-n PSC are presented in Figures 3.25 and 3.26, respectively.

The J-V curves show a significant improvement of the n-i-p and p-i-n PSCs performance. Noting that the V_{oc} and J_{sc} were not affected. Also, $HOMO$ or $E_v$calculated

from ($HOMO = \chi + E_g$) indicate that there are good bands alignment between HOMO of both of HTLs and absorber layer (Figure 3.27).

For the conventional PSC, the quantum efficiency is not affected by modifying HTL because the optical absorption of the hole transport layer is negligible since it is located in the back side of the device. Unlike the quantum efficiency of inverted PSC which is affected by changing HTL materials. This goes back to the layer acting as a window that controls the transmittance of light to the active layer.

parameter	***P3HT***	***PEDOT:PSS***	***Spiro – OMeTAD***	***CuI***	***NiO***	***CuSCN***
$V_{oc}(V)$	1.27	1.27	1.27	1.27	1.27	1.27
$J_{sc}(mA/cm^2)$	21.89	21.89	21.87	21.89	21.89	21.89
FF (%)	74.05	74.51	79.58	83.12	83.00	83.70
η (%)	20.61	20.74	22.13	23.14	23.10	23.30

Table 3. 6: Effect of the different HTL proposed materials on output parameters for n-i-p PSC.

The lowest power conversion efficiency is achieved in both solar cells based on P3HT as HTL, because of the difference between the HOMOs reached 0.5 eV.

It is observed that, $CuSCN$ exhibited the best efficiency ($\eta \sim 23.30\%$) even if $Spiro - OMeTAD$ exhibits the best bands alignment as shown in Figure 4.16. This is due to being holes mobility in $Spiro - OMeTAD$ is much smaller than holes mobility in $CuSCN$.

parameter	*PEDOT:PSS*	*P3HT*	*Spiro – OMeTAD*	*NiO*	*CuI*	*CuSCN*
$V_{oc}(V)$	1.27	1.26	1.27	1.27	1.27	1.27
$J_{sc}(mA/cm^2)$	21.89	21.89	21.89	21.88	21.89	21.89
FF (%)	61.78	66.55	83.15	83.08	83.17	83.73
η (%)	17.12	18.39	23.12	23.13	23.16	23.31

Table 3. 7:Effect of the different HTL proposed materials on output parameters for p-i-n PSC.

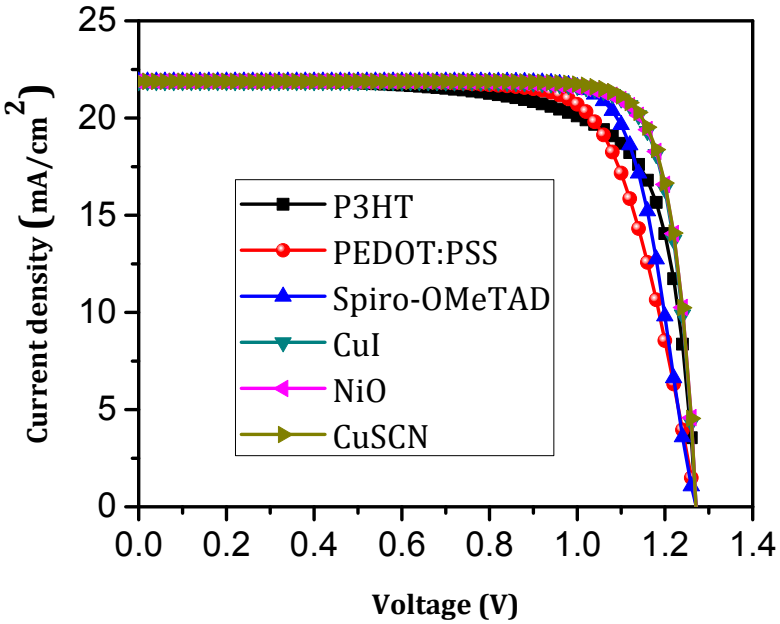

Figure 3. 23: Effect of HTL on J-V characteristic using ZnO as an ETL of n-i-p PSC.

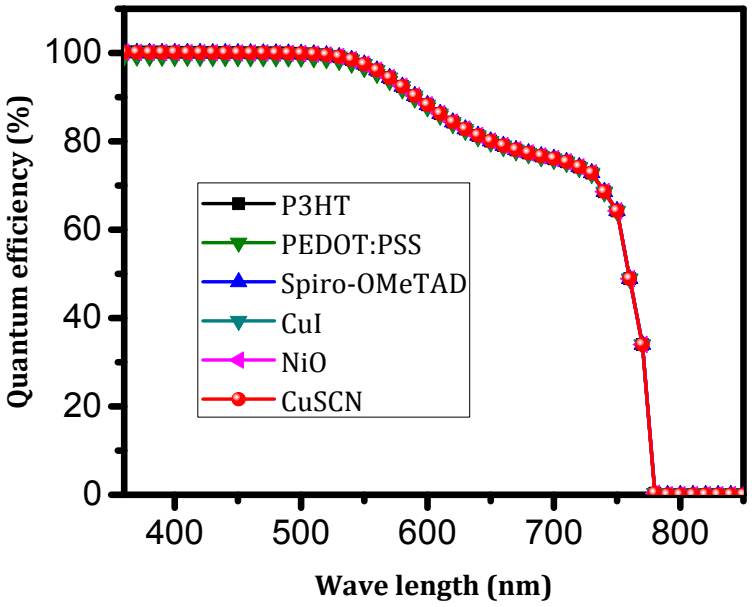

Figure 3. 24: Effect of HTL on quantum efficiency using ZnO as an ETL of n-i-p PSC.

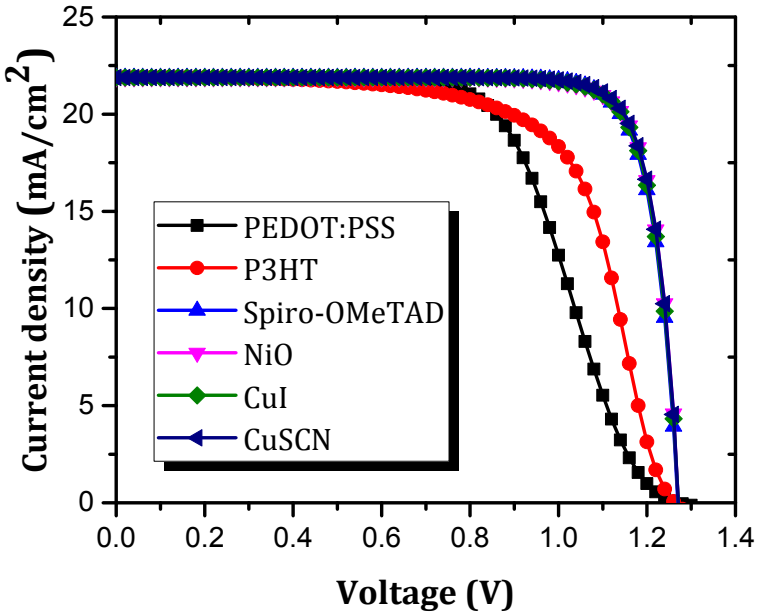

Figure 3. 25: Effect of HTL on J-V characteristic using ZnO as an ETL of p-i-n PSC.

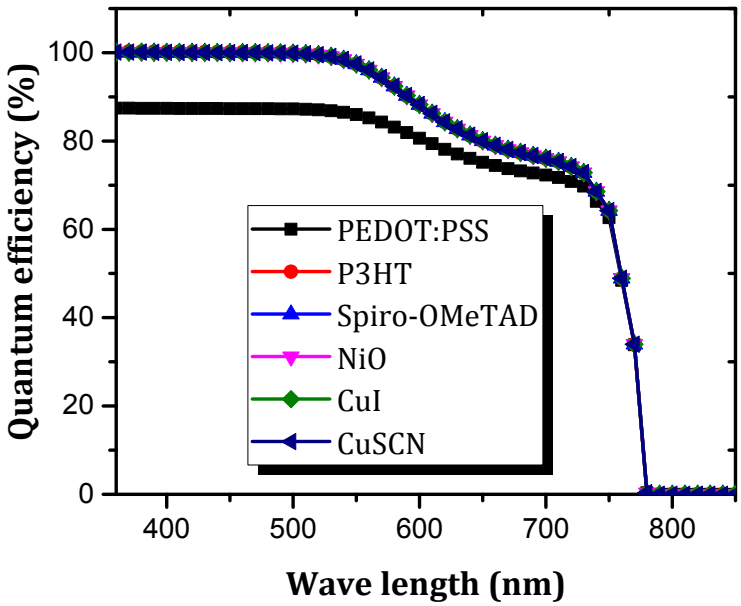

Figure 3. 26: Effect of HTL on quantum efficiency using ZnO as an ETL of p-i-n PSC.

When $CuSCN$ is used as HTL. The solar cell exhibits a conversion efficiency of $\eta\sim$ 23.30 % and a high fill factor of $FF\sim$83.70 % as shown in Table 3.7.

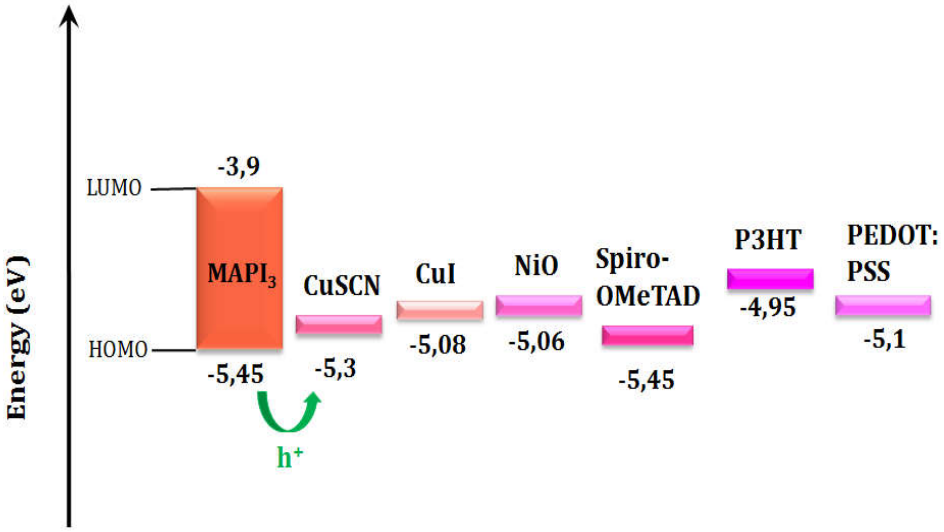

Figure 3. 27: Bands alignment between HTL materials and perovskite.

3.12 Optimization of perovskite solar cell

Since in the previous section it was found that TiO_2 is a good candidate like ZnO as ETL material, we replace ZnO by TiO_2 while preserving $CuSCN$ as HTL. An $FTO/\boldsymbol{TiO_2}/Perovskite/\boldsymbol{CuSCN}/Au$ and $FTO/\boldsymbol{CuSCN}/Perovskite/\boldsymbol{TiO_2}/Au$ solar cells are modeled. The band energy diagram at equilibrium of the n-i-p and p-i-n PSC sare presented in Figures 3.28 and 3.29.

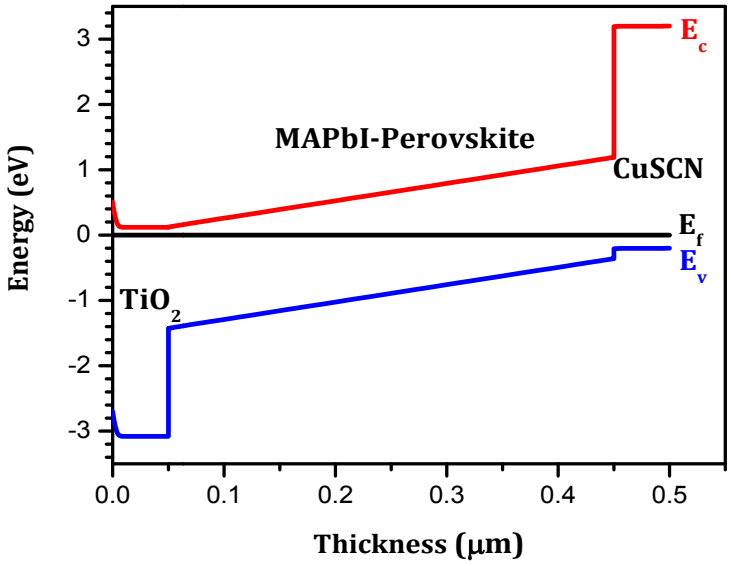

Figure 3. 28: Energetic band diagram of $\boldsymbol{FTO/TiO_2/Perovskite/CuSCN/Au}$ cell.

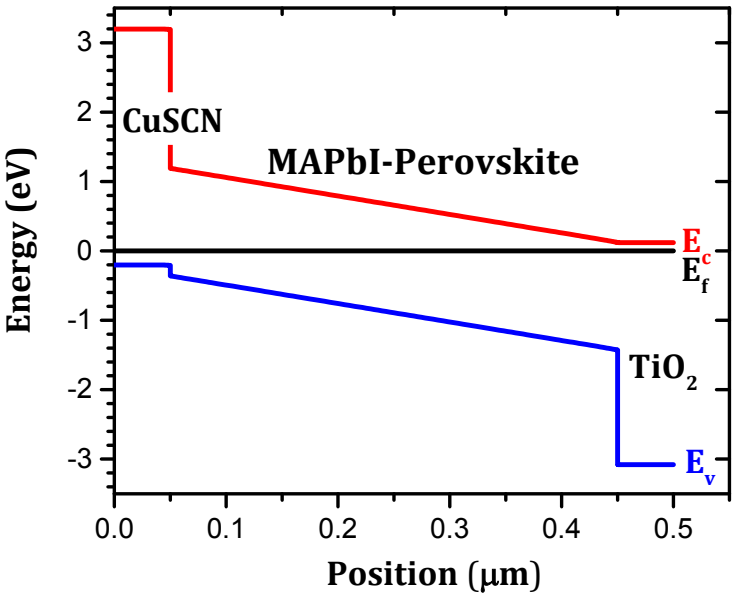

Figure 3. 29: Energetic band diagram of $FTO/CuSCN/Perovskite/TiO\ /Au$ cell.

Tables 3.8 and 3.9 summarize the resulted output parameters in case of TiO_2 as ETL. An enhancement in solar cells performance comparing to the case of using ZnO as ETL about 0.06 % in power conversion efficiency and about 0.34 % in FF for n-i-p PSC and 0.08% in power conversion efficiency and about 0.39 % in FF for p-i-n PSC.

Parameter	***ZnO***	TiO_2
$V_{oc}(V)$	1.27	1.27
$J_{sc}(mA/cm^2)$	21.89	21.89
FF (%)	83.70	84.04
η (%)	23.30	23.36

Table 3. 8: The output parameters of conventional PSC in case of ZnO then TiO_2 as ETL

Parameter	***ZnO***	TiO_2
$V_{oc}(V)$	1.27	1.27
$J_{sc}(mA/cm^2)$	21.89	21.89
FF (%)	83.73	84.12
η (%)	23.30	23.38

Table 3. 9:The output parameters of inverted PSC in case of ZnO then TiO_2 as ETL.

The good performance of the modeled solar cell using TiO_2 as ETL and $CuSCN$ as HTL is associated with the good alignment of the highest occupied molecular orbital (HOMO)level of the $CuSCN$ with the valance band of $CH_3NH_3PbI_3$. Moreover, the energy bands of ETL satisfy the following conditions: (1) Its conduction band (CB) lies under the CB of the active perovskite layer to extract electrons which reach the interfaces afterward. (2) Its valence band (VB) lies much under the VB of the perovskite to reject the holes. (3) ETL VB has a large difference compared to the perovskite VB in order to reject holes, because ETL has a wider band gap (3.2 eV). (4) The electron mobility in ETL is sufficiently high ($\sim$20 $cm^2/V.s$). Similar requirements can also be deduced for HTL.

3.13 Optimization of perovskite thickness

Thickness of a material plays a major role in solar cells performance. So, the active layer thickness is varied from 0.3 μm to 1.2μm for both n-i-p and p-i-n PSC. Figures 3.30 and 3.31 show J-V characteristics and output parameters affected by variation of perovskite thickness for the n-i-p PSC. Figures 3.32 and 3.33 show J-V characteristics and output parameters affected by variation of perovskite thickness for the p-i-n PSC.

For both solar cells, it is observed that increasing the absorber thickness leads to increasing in short circuit current density J_{sc} and decreasing in both open circuit voltage V_{oc} and fill factor FF.

As it is indicated in Figure 3.31, increasing the thickness from 0.3 μm to 0.9μm led to increasing in power conversion efficiency η, which is related to increasing of the short circuit current density J_{sc}. At the thickness 1μm of perovskite layer, the power conversion efficiency reached its highest value 25.02 % and 25.11 % for conventional and inverted PSC, respectively. After, it started in decreasing fairly.

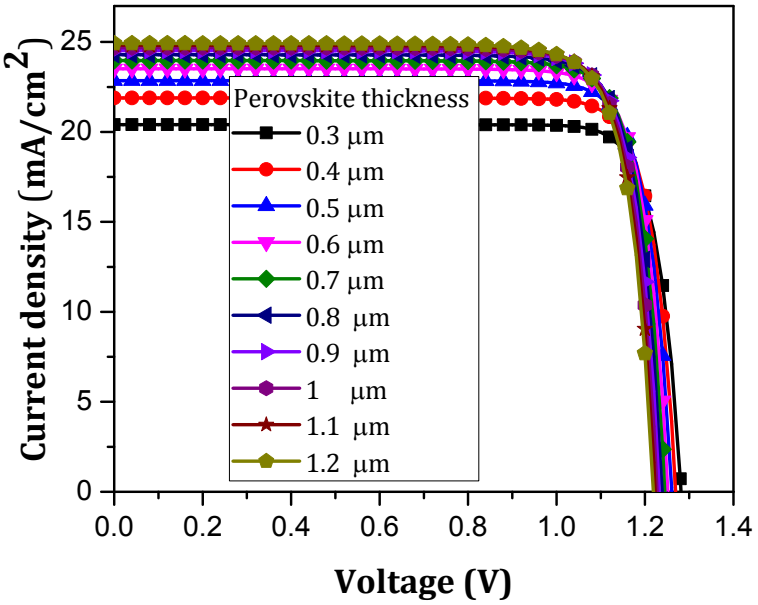

Figure 3. 30: Effect of perovskite thickness on J-V characteristic of n-i-p PSC.

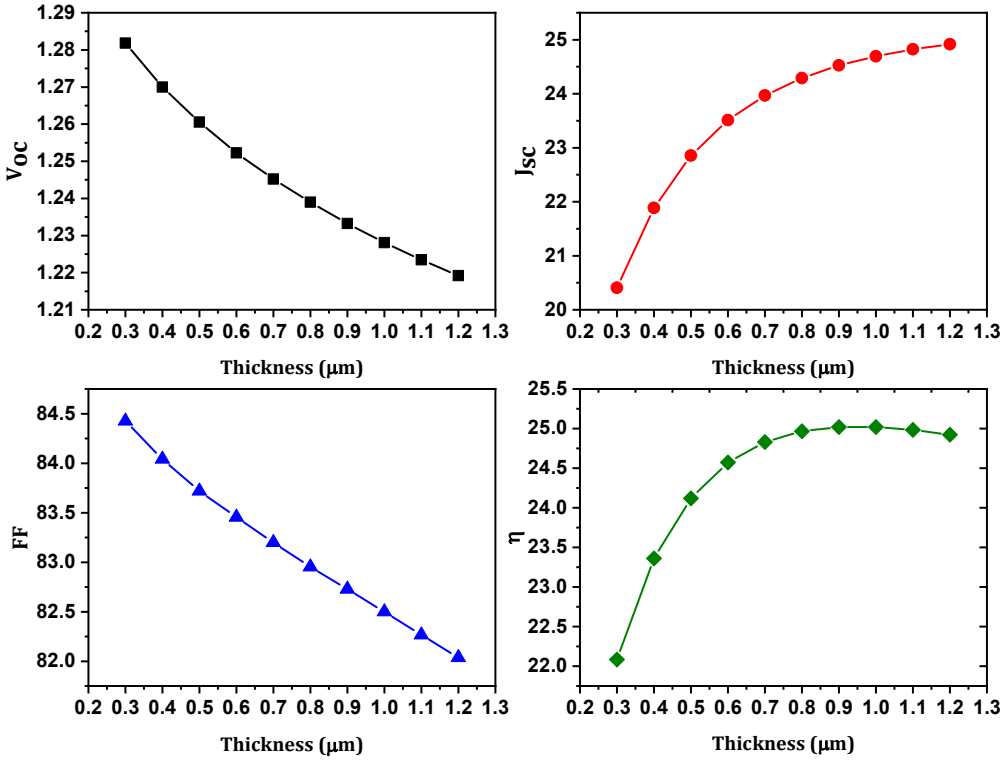

Figure 3. 31: **Effect** of perovskite thickness on output parameters for n-i-p PSC.

When the thickness of the absorber increases, this will allow the longer wavelength of the illumination to be absorbed leading to increasing the absorption of light in perovskite layer, which contributes to the generation of electron-hole pairs. The open-circuit voltage decreases, this variation is due to the bulk recombination of the photogenerated carriers.

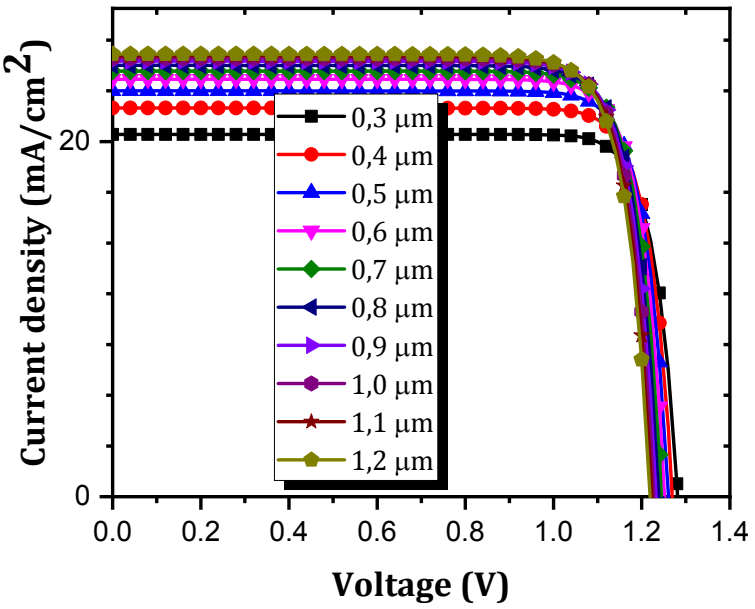

Figure 3. 32: Effect of perovskite thickness on J-V characteristic of p-i-n PSC.

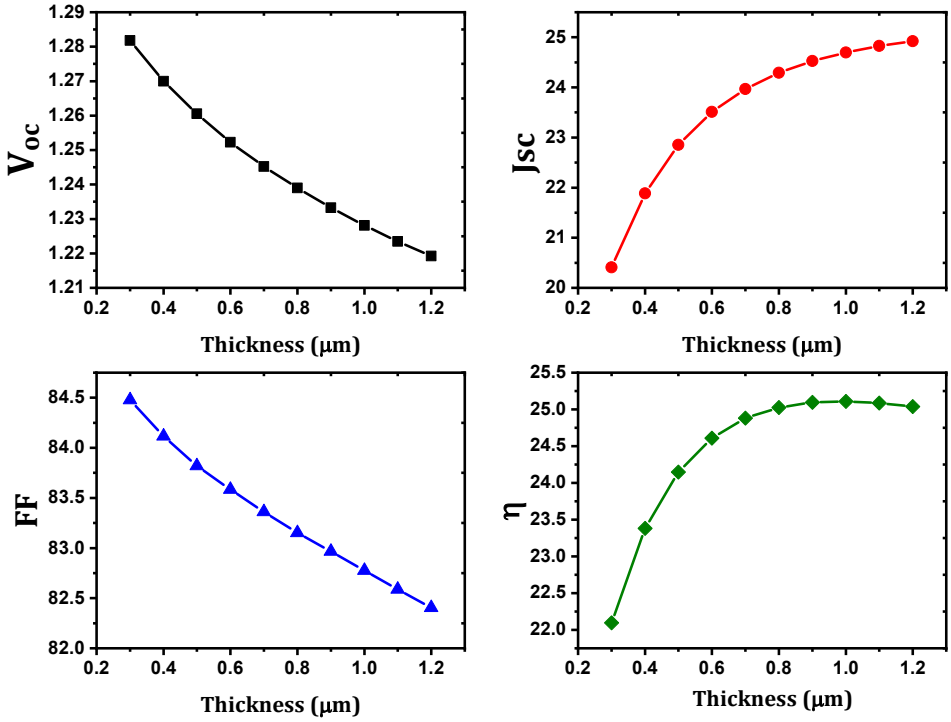

Figure 3. 33: Effect of perovskite thickness on output parameters for p-i-n PSC.

Increasing the permittivity of the material ($\varepsilon \sim 6.5$) (leading to low electron–hole binding energy) [99] enhanced the charge generation. The possibility of charge separation within the absorber itself and long charge carrier diffusion lengths ($L_{n,p} \sim 1\ \mu m$) can explain the good performance of perovskite solar cell. At width (W) more than $1\ \mu m$ ($W \geq 1\ \mu m$) in the absorber layer, there is a bound to occur recombination of charge carriers generated in the absorber. In that case, the charges recombine before they get extracted at the electrodes.

So, we optimized the thickness of perovskite layer to **1 µ*m*** in our solar cells. The performance of modeled solar cells improved. For n-i-p PSC, the conversion efficiency reached 25.02 % and short circuit current density (J_{sc}) increased to24.70 mA/cm^2. While the conversion efficiency reached 25.11 % and short circuit current density (J_{sc}) increased to24.92 mA/cm^2 for p-i-n PSC.

3.14 Effect of interfacial defects

In this part, we briefly introduce the effect of defects on the device performance of perovskite solar cells. The performance of perovskite solar cells can be altered (in most case negatively) by defect states [100]. Deposition process of perovskite solar cell can induce a formation of defects mainly located at surface (or interface) and grain boundaries [101]. These defects results from the interactions of the precursor solvents with HTL and ETL, i.e. the lack of stochiometric compositions at the surfaces of grains and the sublimation of organic molecules during the thermal annealing process could leave defects [101]. Existence of impurities might cause point defects which could form recombination centers.

Substitution defects I_{MA}(I atom occupying a MA (CH_3NH_3) site)located at ca. $-0.75\ eV$ below the conduction band is the main deep defect of perovskite films fabricated by sequential deposition method [101].

Another type of defects was reported by Fan Zhang and co-workers[99], who found that performance hysteresis of perovskite solar cells, is due defects in bulk of both of perovskite and TiO_2 and Perovskite/TiO_2 interface,which affect the electrons injection and electron-hole recombination at the interface. The oxygen vacancies exist naturally in commercial and no treated crystalline TiO_2[100-101].

Consequently in this part, we study the effect of defects on the n-i-p and p-i-n PSCs performances; by considering the two main types of interfacial defects: substitution defects (I_{MA}) and oxygen vacancy (V_O). The defects density is varied from 10^{10} to $10^{14} cm^{-2}$ while theirs energy position in the band gap and charge nature are given in Table 3.10.

Interfacial TiO_2/Perovskite defects	Energy below E_c	Charge type
Substitution defects (I_{MA})	0.75	neutral
Oxygen Vacancy (Vo)	0.17	donor

Table 3. 10: Energy position and types of interfacial defects.

For conventional PSC, the effect of the I_{MA} and V_O defects on the J-V characteristic is shown in Figure 3.34 and Figure 3.35, respectively. In both cases the most sensible parameter is V_{oc} (Figures 3.36 and 3.40) which exhibits a slight reduction caused mainly

by I_{MA} defects when it reaches $10^{14}cm^{-2}$. Consequently, despite that $10^{14}cm^{-2}$is significantly high as interface density, the power conversion efficiency decreases slightly in conventional PSC from 25.02% to 24.61 % for the I_{MA} defects and to 24.95% for the V_o defects (Figure 3.37).

In inverted PSC, the effect of the I_{MA} and V_O defects on the J-V characteristic is shown in Figures 3.38 and 3.39, respectively. The power conversion efficiency decreases from 25.11% to 24.85 % for the I_{MA} defects and to 25.07% for the V_O defects (Figure 3.41).

The performance of inverted PSC is less affected by interfacial defects. Substitution I_{MA}defects located deeper than $V_O$defects have more pronounced effect on the performance of n-i-p and p-i-n PSCs especially if the density of the defects exceeds $10^{14}cm^{-2}$. These electronic states in the band gap of the semiconductor, act as Shockley-Read-Hall (SRH) recombination centers. However the oxygen vacancy (V_o) is considered as shallow defect which leads to slowing down the injection of photo excited electrons from perovskite to TiO_2[101].

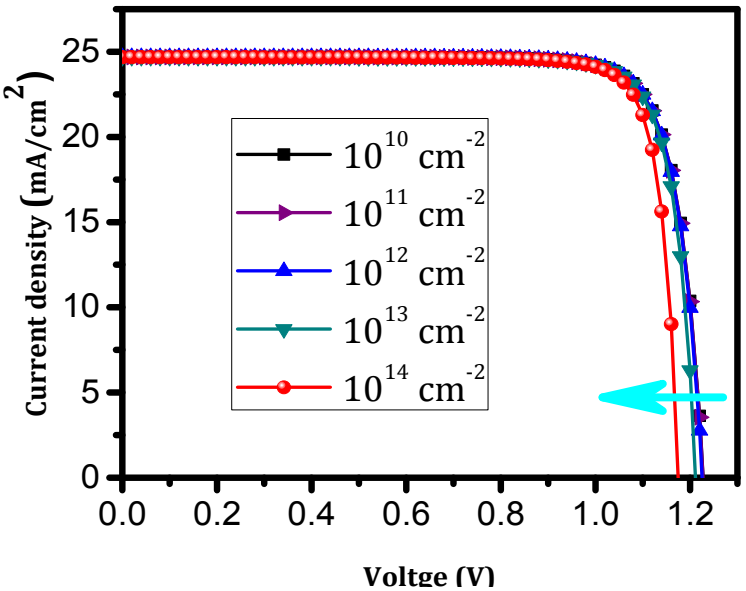

Figure 3. 34: Effect of I_{MA} defects on J-V characteristic for n-i-p PSC.

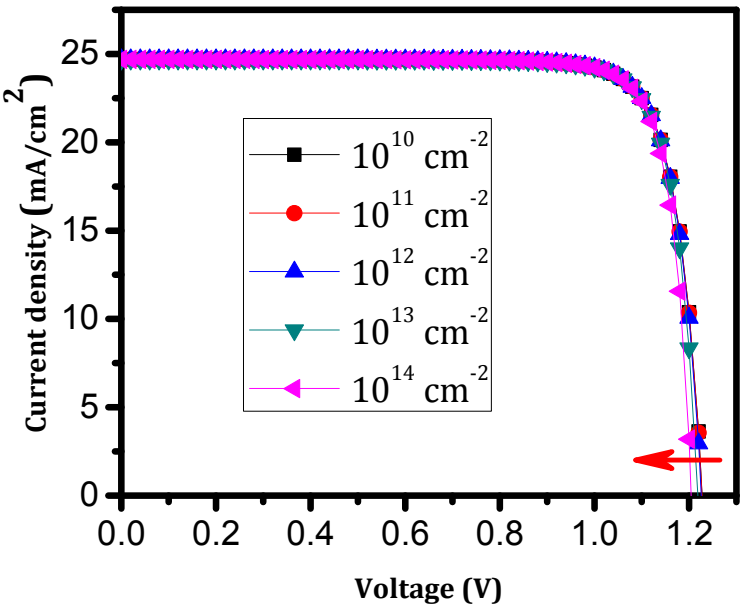

Figure 3. 35: Effect of V_O defects on J-V characteristic for n-i-p PSC.

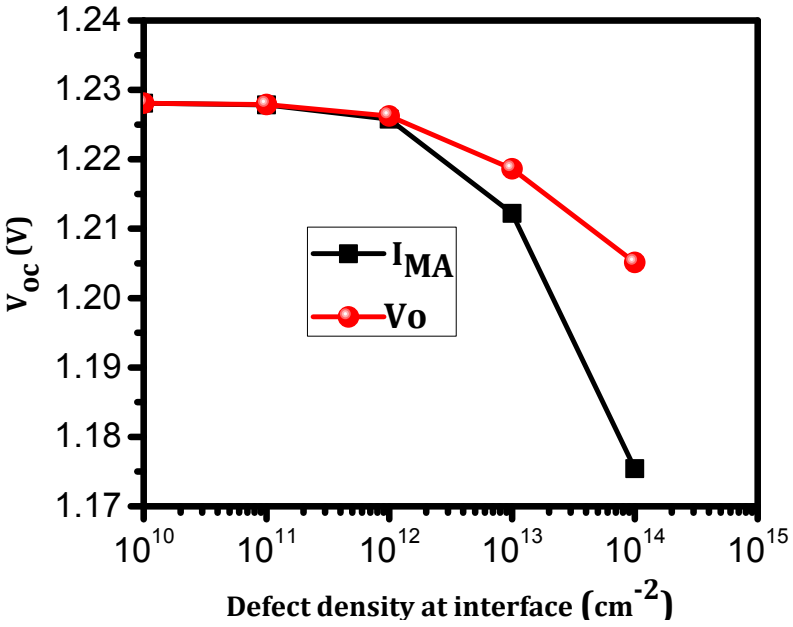

Figure 3. 36: Effect of I_{MA} and V_O on open circuit voltage (V_{oc}).

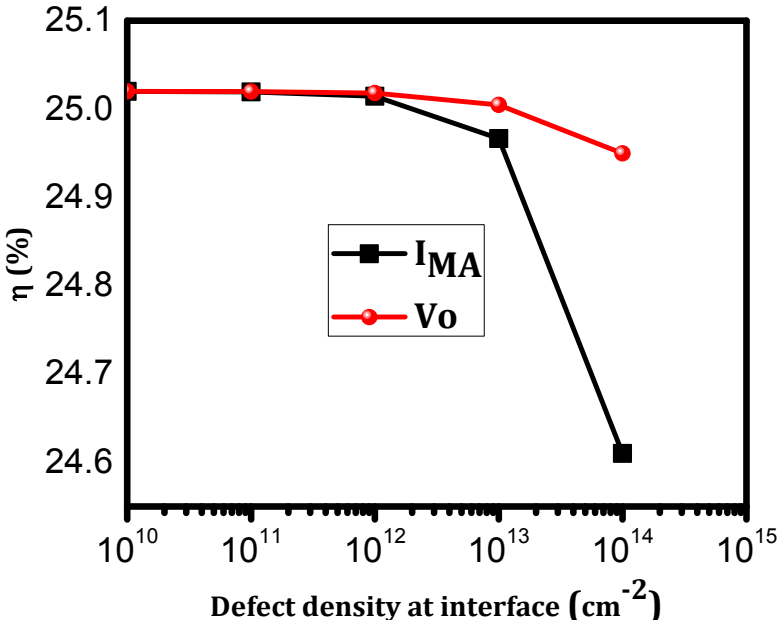

Figure 3. 37: Effect of I_{MA} and V_O on power conversion efficiency (η) for n-i-p PSC.

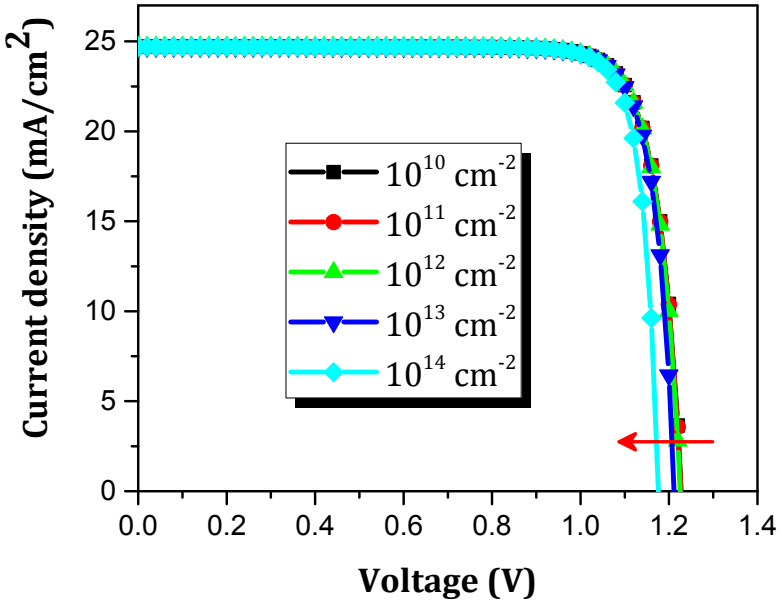

Figure 3. 38: Effect of I_{MA} defects on J-V characteristic for p-i-n PSC.

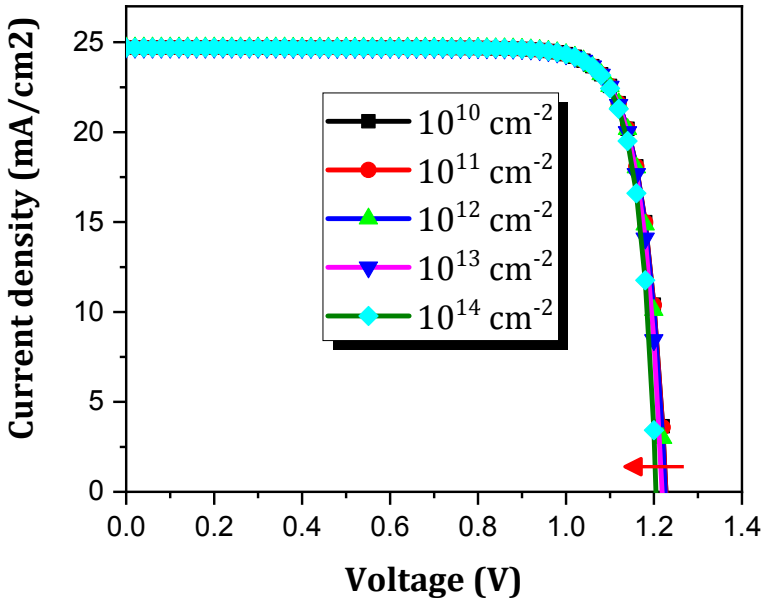

Figure 3. 39: Effect of V_O defects on J-V characteristic for p-i-n PSC.

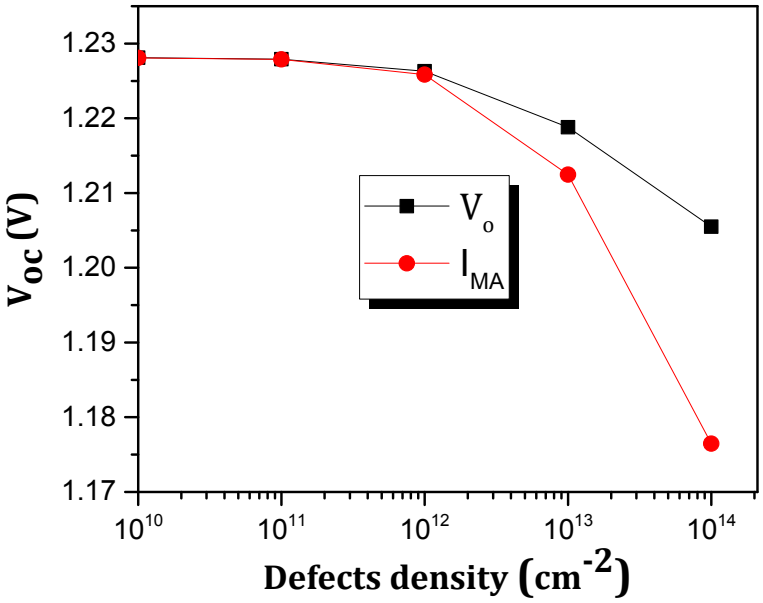

Figure 3. 40: Effect of I_{MA} and V_O on open circuit voltage (V_{oc}) for p-i-n PSC.

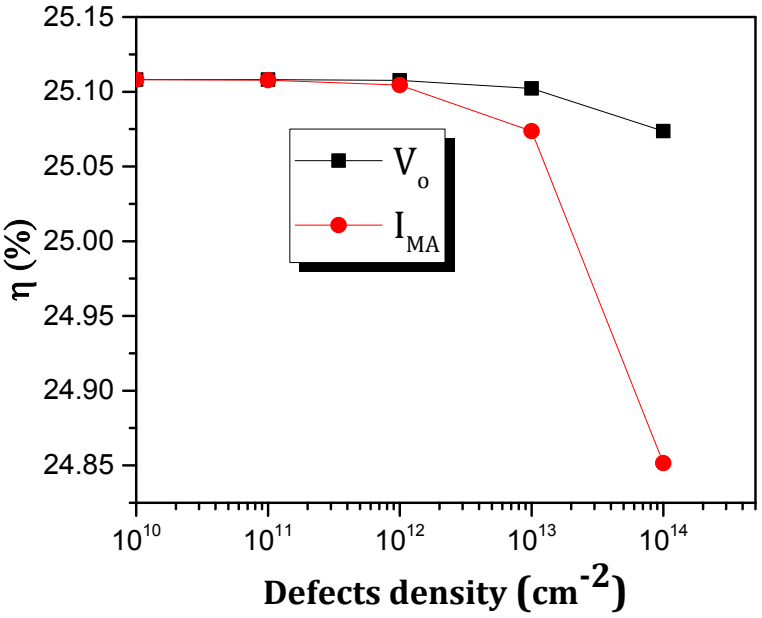

Figure 3. 41: Effect of $\boldsymbol{I_{MA}}$ and $\boldsymbol{V_o}$ on power conversion efficiency ($\boldsymbol{\eta}$) for p-i-n PSC.

Defect states lie near the middle of the band gap instead of on the bottom of the conduction band or at the top of the valence band, have more bad impact on the properties of $MAPbI_3$solar cells. These results indicate that the perovskite/TiO_2 interface is crucial in charge separation.

3.15 Effect of temperature

In this part, the effect of temperature on conventional and inverted PSCs is studied. The temperature was changed from $250K$ to $350K$.

The affected J-V characteristics of both PSCs are represented in Figures 3.42 and 3.43. They show a significant decreasing in open circuit voltages. While the short circuit currents are not affected.

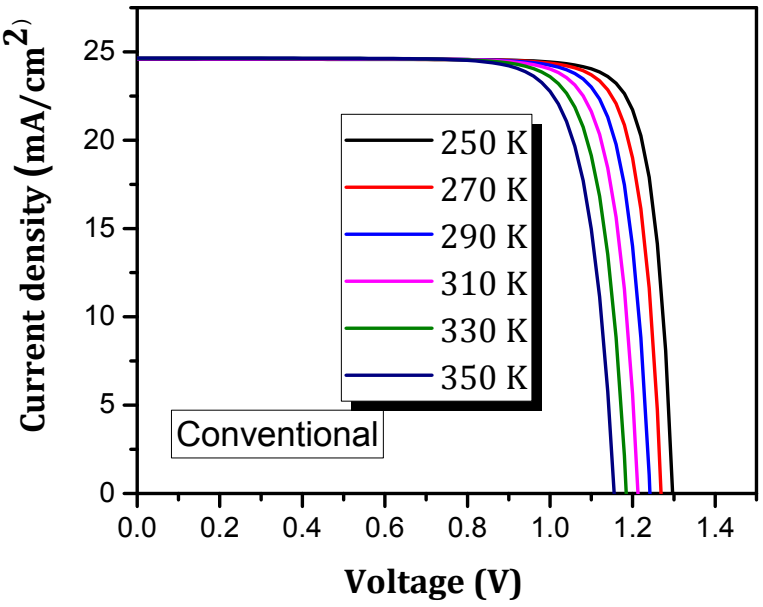

Figure 3. 42: Effect of temperature on J-V characteristic for n-i-p PSC.

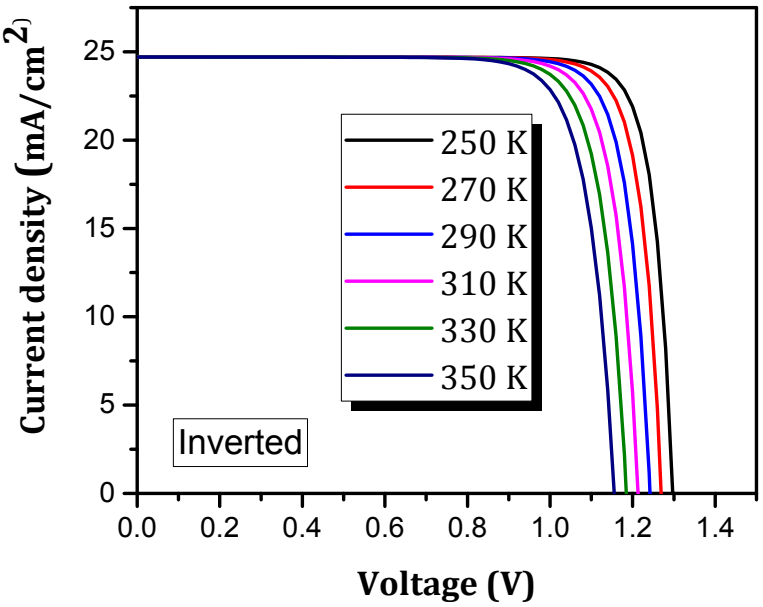

Figure 3. 43: Effect of temperature on J-V characteristic for p-i-n PSC.

Figure 3.44 represents the affected open circuit voltages and power conversion efficiencies for our PSCs. The open circuit voltage of both PSCs is influenced by the same way. When the temperature changed from $250K$ to $350K$, the open circuit voltage decreased from 1.30 V to 1.16 V; while the power conversion efficiency was decreased

from 26.95 % to 22.81 for conventional PSC and from 27.22 % to 22.91 % for inverted PSC.

The open circuit voltage decreases considerably with temperature as the open circuit voltage is given by Equation 1.4. Decreasing of open circuit voltage with temperature is dominated by the exponential increase of the reverse saturation current with temperature. Consequentially, the conversion efficiency decreases.

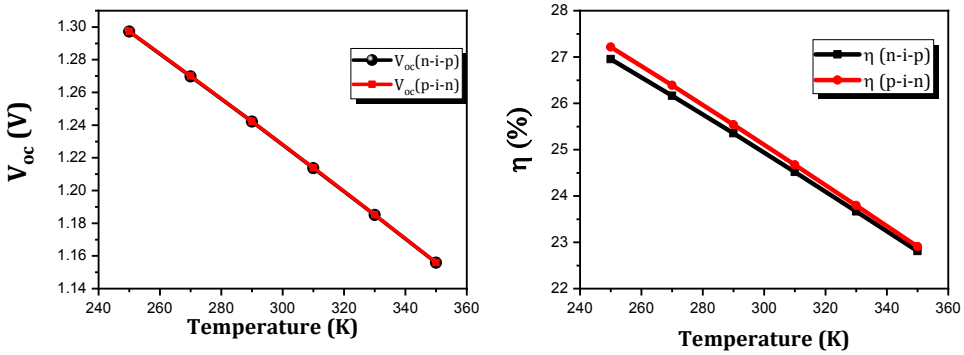

Figure 3. 44: Effect of Temperature on Voc and eta for conventional and inverted PSCs.

3.16 Conclusion

Conventional and inverted PSCs were simulated using SCAPS simulator, using ITO as an ETL and $PEDOT:PSS$ as an HTL. The conventional PSC exhibited better performance where the power conversion efficiency was 13.94% for conventional structure and 10.99% for the inverted one. Replacing ITO by TiO_2 or ZnO led to an enhancement in PSCs' performance where the power conversion efficiency of conventional and inverted PSCs reached 20% and 17.2%, respectively. Also, both PSCs were optimized using CuSCN as an HTL and ZnO as an ETL where the power conversion efficiency was 23.3% which increased to 23.36 % and 23.38% for conventional an inverted PSCs, respectively using TiO_2 as an ETL. Furthermore, thickness of PSCs were optimized to 1 μm leading to 25.02 % and 25.11% in power conversion efficiency for conventional and inverted PSCs; respectively.

Moreover, substitution defects I_{MA} and oxygen vacancies V_O showed a detrimental effect on PSCs performance. But the inverted structure is less affected by these

interfacial defects, in agreement with experimental measurements repported by many works

Finally, when the temperature increased from $250K$ to $350K$, the power conversion efficiency decreased from 26.95 % to 22.81 for conventional PSC and from 27.22 % to 22.91 % for inverted PSC.

Conclusion

Perovskite materials with its remarkable properties such as long electron diffusion length, high optical absorption, small electron and hole effective masses, low processing temperature and strong excitonic transitions, made them suitable for solar cell devices. These properties make the organometallic halide perovskites based solar cells achieve comparable efficiencies to the single crystal silicon and $CIGS$ thin films counterparts. And for this, perovskite solar cells have gained a major interest as "third generation solar cells".

Using SCAPS software, two planar perovskite solar cells in n-i-p and p-i-n configurations were simulated at AM1.5G solar spectrum with an incident power density of $100 mW/cm^2$ at room temperature ($300\ K$). The considred "n" layer was a $0.05\ \mu m$ of ITO, "p" layer was $0.05\ \mu m$ of $PEDOT{:}PSS$ and "i" layer was $0.4\ \mu m$ of$CH_3NH_3PbI_3$. Both solar cells showed relatively poor performance. Although, the conventional solar cell exhibited a power conversion efficiency and a fill factor better than those of inverted solar cell. The power conversion efficiency was about 13.94% for conventional solar cell and about 10.99% for inverted cell. The poor performance of inverted PCS was related to the low doping of $PEDOT{:}PSS$ which led to bulk resistance and interfacial contact resistance and this was observed by deviation of J-V curve from quadratic shape.

Because of some shortcomings in using ITO and $PEDOT{:}PSS$ as an ETL and HTL, respectively; we looked for alternatives to these materials. So, several materials were studied for possible electron and hole transport layers (ETL and HTL). $PCBM$, $IGZO$, SnO_2, $TiO_2$and ZnOwere tested as an ETL and compared to ITO.

We found that replacing ITO by TiO_2 or ZnO improved both solar cells performance where the power conversion efficiency exceeded 20% for conventional PSC and 17.2% for inverted PSC. Furthermore, the hole transport layer was changed to determine the appropriate p type material working as a hole transporter. $Spiro-OMeTAD$, $P3HT$, $CuSCN$, CuI and NiO were examined as an HTL with preserving ZnO as an ETL. For conventional PSC, quantum efficiency curves did not affected by modifying HTL because it located in the back side of the deviceand the optical absorption is negligible there unlike the quantum efficiency of inverted PSC which is affected by changing HTL materials. This goes back to the layer acting as a window that controls the transmittance of light to the active layer. In addition, the lowest power conversion efficiency is achieved in both solar cells based on P3HT as HTL. PSCs based on $CuSCN$ as an HTL and ZnO as an ETL achieved power conversion efficiency

about 23.3% for both n-i-p and p-i-n PSCs. On the other hand, by replacing ZnO by TiO_2 the power conversion efficiency increased by 0.06% and 0.08% for n-i-p and p-i-n, respectively. We considered that inverted PSC is relatively more efficient than conventional PSC.

Also, thickness of PSCs were optimized to $1\,\mu m$. At this thickness the absorption of photons was optimum, leading to $25.02\ \%$ and 25.11% in power conversion efficiency for n-i-p and p-i-n PSCs; respectively.

Moreover, deposition process affects the formation of defects especially at the surface, interface and grain boundaries. Two main types could be existed in perovskite solar cells which are: substitution defects I_{MA} when I atom occupies a MA (CH_3NH_3) site and oxygen vacancies V_O. The effect of these defects on PSCs was studied. Results showed a significant decreasing in solar cells' performance for both types of defects.

When the temperature changed from $250K$ to $350K$, the power conversion efficiency decreased from $26.95\ \%$ to 22.81% for conventional PSC and from $27.22\ \%$ to $22.91\ \%$ for inverted PSC.

As further work, experimental and numerical studies will be done on this type of solar cells in both conventional and inverted configurations. More researches will be achieved to find more safe and cheap materials suitable for perovskite solar cells and to make these cells have long duration and adequate for commercial production.

References

References

[1] Michele D. B, (2016), The stability of third generation solar cells, PhD. Thesis, University of Padua, Center for Nano-science and Technology, CNST @ PoliMi, Italian Institute of Technology.

[2] Shi, Z., Jayatissa, A. (2018). Perovskites-Based Solar Cells: A Review of Recent Progress, Materials and Processing Methods. Materials, 11(5), 729: DOI https://doi.org/10.3390/ma11050729

[3] https://www.nrel.gov/pv/cell-efficiency.html visited march 1st,2021.

[4] Suneth C. W., Zhaoning S., Adam B. P., and Michael J. H, (2018)., Evolution of Perovskite Solar Cells, University of Toledo, Toledo, OH, United States. DOI: https://doi.org/10.1016/B978-0-12-812915-9.00003-4.

[5] Amu, T. L., (2014), Performance Optimization Of Tin Halide Perovskite Solar Cells Via Numerical Simulation, thesis for obtaining degree of master in science, Department of Theoretical Physics African University of Science and Technology, Abuja.

[6] Roni P., Oct 12, 2020, Perovskite applications, Perovskite Solar, Saule Technologies, https://www.perovskite-info.com/saule-technologies-launches-sunbreaker-lamellas-assisted-perovskite-solar-cells

[7] Bryce S., (2018), Efficient Lead-Free Perovskite Solar Cell, Department of Electrical and Computer Engineering, 2ECE 498 CB, University of Illinois at Urbana-Champaign, Urbana, IL 61801, USA.

[8] Stone, J. L., (1993). Photovoltaics: Unlimited Electrical Energy from the Sun. Physics Today, 46(9), 22–29. doi:10.1063/1.881362.

[9] Torchynska T. V. and Polupan G., (2004), High efficiency solar cells for space, Superficies y Vacío 17(3), 21-25.

[10] Harold J. H., (1977), Solar cells for terrestrial applications, **Sci. direct**, vol. 19, no. 6, pp. 605–615.

[11] Kulkarni et al, (2014), Rural Electrification through Renewable Energy Sources- An Overview of Challenges and Prospects, vol. 5013, no. 3, pp. 384–389.

[12] Granovskii, M., Dincer, I. & Rosen, M. (2007). Greenhouse gas emissions reduction by use of wind and solar energies for hydrogen and electricity production: Economic factors. International Journal of Hydrogen Energy. 32. 927-931. 10.1016.

[13] Lior N., (2010), Sustainable energy development: The present (2009) situation and possible paths to the future," **Energy**, vol. 35, no. 10, pp. 3976–3994.

[14] Ye, M., Lv, M., Chen, C., Iocozzia, J., Lin, C., & Lin, Z. (2014). Design, Fabrication, and Modification of Cost-Effective Nanostructured TiO2 for Solar Energy Applications.Low-Cost Nanomaterials, 9–54.doi:10.1007/978-1-4471-6473-9_2.

[15] Stone, J. L. (1993). Photovoltaics: Unlimited Electrical Energy from the Sun. Physics Today, 46(9), 22–29. doi:10.1063/1.881362.

[16] Balema, V., (2009), Alternative Energy Photovoltaics, Ionic Liquids, and MOFs, **Mateial Matters**, vol. 4, no. 4, p. 1.

[17] Chapin, D. M., Fuller, C. S., & Pearson, G. L. (1954). A New Silicon p-n Junction Photocell for Converting Solar Radiation into Electrical Power. *Journal of Applied Physics, 25(5), 676–677.* doi:10.1063/1.1721711 .

[18] M. A. Green et al., (2014), Solar cell efficiency tables (version 43), pp. 1–9.

[19] Brittany L., Oliva C. A., Barron R., (2011), An Introduction to Solar Cell Technology. Open Stax CNX. 11, http://cnx.org/contents/dd0537a2-fb5d-439d-8febbf2e50656dae@1

[20] R. G. Nrel, (2010), **Renewable Energy Data Book**, no. 2010,pp. 1–132.

[21] NREL, Solar cell efficiency chart, (2019), https://www.nrel.gov/pv/assets/images/efficiency-chart.pngi accessed august 2019.

[22] Conibeer G., (2007), Third-generation photovoltaics, ARC Photovoltaics Centre of Excellence, School of Photovoltaic and Renewable Energy Engineering, University of New South Wales , Sydney, NSW 2052, Australia, VOLUME 10, NUMBER 11.

[23] Equer B., (1993), Energie solaire photovoltaïque", physique et technologie de la conversion photovoltaïque, 1ère édition, ELLIPES, Paris.

[24] Sato H., Minami T., Takata S., and Yamada T., (1993), Transparent conducting p-type NiO thin films prepared by magnetron sputtering, Thin Solid Films 236, 27–31.

[25] A. Faiza, (2015), Etude d'une cellule solaire a-IGZO(n)/µ-Si(p), thesis of Master, University Med KhiderBiskra.

[26] Nelson J., (2003), *The Physics of Solar Cells*. Imperial College Press: London, pp. 1–325.

[27] Zeman M., Introduction to photovoltaic solar energy. pp. 1–139.

[28] Sze S. M., Kwok K. Ng, Physics of Semiconductor Devices, third edition. 0-471-14323-5.

[29] Liao K.-S., Yambem S. D., Haldar A., Alley N. J., and Curran S. A., (2010), Designs and architectures for the next generation of organic solar cells," *Energies,* vol. 3, pp. 1212-1250.

[30] Loreta A. T.,(2014), Performance optimization of tin halide perovskite solar cells via numerical simulation, A Thesis presented to the Department of Theoretical Physics, African University of Science and Technology, Abuja..

[31]Yadav P., Pandey K., Bhatt P., Raval D., Tripathi B., Chandra K. P. ,Pandey M. K. and Kumar M., (2015), Exploring the performance limiting parameters of perovskite solar cell through experimental analysis and device simulation. Solar Energy 122,773–782.

[32] Suneth, C. W., Song, Z., Phillips, A. B., and Heben, M. J., (2018), Evolution of Perovskite SolarCells. University of Toledo, Toledo, OH, United States, Elsevier Inc.

[33] Kojima A., Teshima K., Shirai Y., and Miyasaka T. (2009), Organometal Halide Perovskites as Visible-Light Sensitizers for Photovoltaic Cells. J. AM. CHEM. SOC.131, 6050–6051.

[34] Lee M. M., Teuscher J., Miyasaka T., Murakami, T.N., and Snaith H.J. (2012), Efficient hybrid solar cells based on meso-superstructured organometal halide perovskites. Science 338 643647.

[35] Rodríguez B. O. A. (2015), A characterization on hybrid lead halide perovskite solar cells with TiO2 mesoporous scaffold, Master Thesis, university of Jaume, November 2015.

[36] Organic-Inorganic Perovskite Precursors, www.TCIchemicals.com. Accessed august 18th, 2016.

[37] Selina O. (2016), Research Update: The electronic structure of hybrid perovskite layers and their energetic alignment in devices, APL MATERIALS 4, 091502.

[38] Bertrand P., Jesper T. J, Juan P. C-B., Naresh K. J., Amitava B, Sudip C., Ute B. C., Rajeev A., Anders H., Michael O., and Hakan R., (2017), Valence Level Character in a Mixed Perovskite Material and Determination of the Valence Band Maximum from Photoelectron Spectroscopy: Variation with Photon Energy; J. Phys. Chem. C 2017, 121, 26655-26666.

[39] Brivio F., Butler K. T., Walsh A., Schilfgaarde M., (2014), Relativistic quasiparticle self-consistent electronic structure of hybrid halide perovskite photovoltaic absorbers Phys. Rev. B 2014, 89, 155204.

[40] Tsutomu M., (2018), Lead Halide Perovskites in Thin Film Photovoltaics: Background and Perspectives, Bull. Chem. Soc. Jpn. 2018, 91, 1058–1068.

[41] Brittman S., Adhyaksa G. W. P., & Garnett E. C. (2015). The expanding world of hybrid perovskites: materials properties and emerging applications. MRS Communications, 5(01), 7–26.doi:10.1557/mrc.2015.6.

[42] Corre**a**-Baena J.-P., Abate A., Saliba M., Tress W., Jesper Jacobsson T., Grätzel M., and Hagfeldt A., (2017), The rapid evolution of highly efficient perovskite solar cells. Energy & Environmental Science, 10(3), 710–727. doi:10.1039/c6ee03397k.

[43] Zhou, Y., Zhou, Z., Chen, M., Zong, Y., Huang, J., Pang, S., &Padture, N. P. (2016). Doping and alloying for improved perovskite solar cells. Journal of Materials Chemistry A, 4(45), 17623–17635. doi:10.1039/c6ta08699c.

[44] Abdi-Jalebi, M., Dar, M. I., Sadhanala, A., Senanayak, S. P., Franckevičius, M., Arora, N. Friend, R. H. (2016). Impact of Monovalent Cation Halide Additives on the Structural and Optoelectronic Properties of CH3NH3PbI3Perovskite. Advanced Energy Materials, 6(10), 1502472. doi:10.1002/aenm.201502472.

[45] Zhou, Y., Chen, J., Bakr, O. M., & Sun, H.-T. (2018). Metal-doped lead halide perovskites: synthesis, properties, and optoelectronic applications. Chemistry of Materials. doi:10.1021/acs.chemmater.8b02989.

[46] Chang, C., Zou, X., Cheng, J., Yang, Y., Yao, Y., Ling, T., &Ren, H. (2019). NaI Doping Effect on Photophysical Properties of Organic-Lead-Halide Perovskite Thin Films by Using Solution Process. Advances in Materials Science and Engineering, 2019, 1–9. doi:10.1155/2019/2878060.

[47] Frolova, L. A., Dremova, N. N., &Troshin, P. A. (2015) , The chemical origin of the p-type and n-type doping effects in the hybrid methylammonium–lead iodide (MAPbI3) perovskite solar cells. Chemical Communications, 51(80), 14917–14920. doi:10.1039/c5cc05205j.

[48] Nanduri, S. N. R. (2017), Numerical simulation and performance optimization of perovskite solar cell. University Of Missouri-Kansas City.

[49] Yi W. (2012), Synthesis and optical properties of self-assembled 2D layered organic-inorganic perovskites for optoelectronics. École normale supérieure de Cachan - ENS Cachan, 2012.

[50] Amrita M. B., Dan R. W., and Thomas U., (2018), High efficient perovskite solar cell material CH3NH3PbI3: Synthesis of films and their characterization, AIP Conference Proceedings 1942, 140038.

[51] Lee J-W and Park N-G, (2015), Two-step deposition method for high-efficiency perovskite solar cells, MRS BULLETIN, Materials Research Society. VOLUME 40.

[52] Heping S., The D., Yiliang W., Jun P., Daniel J., Nandi W., Klaus W., Tom W. and ,Kylie C., (2018), Metal halide perovskite: a game-changer for photovoltaics and solar devices via a tandem design, Science and Technology of advanced MaTerialS, vol. 19, no. 1, 53–75.

[53] Qamar W., Naveen K. E., Yaseen I., Ashraf U., Rajan J., (2018), Tandem perovskite solar cells, Renewable and Sustainable Energy Reviews 84, 89–110.

[54] Rui S., Anita W. Y., Ho B., Shujuan H., Mark K., Xiaojing H., Liangcong J., Yi-Bing C., and Martin A. G., (2015), Four-Terminal Tandem Solar Cells Using CH3NH3PbBr3 by Spectrum Splitting, J. Phys. Chem. Lett. 2015, 6, 3931-3934. DOI: 10.1021/acs.jpclett.5b01608.

[55] Eperon, G. E., Burlakov, V. M., Goriely, A., &Snaith, H. J. (2013). Neutral Color Semitransparent MicrostructuredPerovskite Solar Cells. ACS Nano, 8(1), 591–598. doi:10.1021/nn4052309.

[56] ChuantianZuo , Henk J. Bolink , Hongwei Han , Jinsong Huang , David Cahen ,* and Liming Ding, Advances in Perovskite Solar Cells, *Adv. Sci.* **2016**, 150032,

[57] Andy Extance, 7 January 2019, First building-integrated deployment shows perovskite solar's growing maturity, Chemistry world, https://www.chemistryworld.com/news/first-building-integrated-deployment-shows-perovskite-solars-growing-maturity/3009953.article

[58] Chen, J., Zhou, S., Jin, S., Li, H., & Zhai, T. (2016). Crystal organometal halide perovskites with promising optoelectronic applications. Journal of Materials Chemistry C, 4(1), 11–27. doi:10.1039/c5tc03417e.

[59] Minhuan W., Yantao S., Jiming B., Qingshun D., Hongjun S., Hongzhu L., Yingmin L., Yuzhi Z., (2016), Electroluminescence from perovskite LEDs with the structure of Ag/Spiro-OMeTAD/CH3NH3PbI3/TiO2/FTO Chemical Physics Letters 662 (2016) 176–181.

[60] Tan, Z.-K., Moghaddam, R. S., Lai, M. L., Docampo, P., Higler, R., Deschler, F., Price, M., Sadhanala, A., Pazos, L. M., Credgington, D., Hanusch , F., Bein, T., Snaith, H.J. and Friend, R. H. (2014). Bright light-emitting diodes based on organometal halide perovskite. Nature Nanotechnology, 9(9), 687–692. doi:10.1038/nnano.2014.149.

[61] Nana W., Lu C., Junjie S, Xiaoyong L., Yizheng J., Jianpu W., and Wei H., (2016), Morphology control of perovskite light-emitting diodes by using amino acid self-assembled monolayers, APPLIED PHYSICS LETTERS 108, 141102.

[62] Zhao, X., & Tan, Z.-K. (2019). Large-area near-infrared perovskite light-emitting diodes. Nature Photonics.doi:10.1038/s41566-019-0559-3.

[63] Mohite, A., Chhowalla, M., Gupta, G., (2018), Efficient Solar Water Splitting with 5,000 Hours Stability Using Earth-abundant Catalysts and Durable Layered 2D Perovskites, Los Alamos National Laboratory.

[64] Malinkiewicz, O., Imaizumi, M., Sapkota, S.B. *et al.* Radiation effects on the performance of flexible perovskite solar cells for space applications. *emergent mater.*(2020). doi:10.1007/s42247-020-00071-8.

[65] Minemoto et al, (2014), Device modeling of perovskite solar cells based on structural similarity with thin film inorganic semiconductor solar cells, *J. Appl. Phys.*, vol. 116, no. 5, p. 05450.

[66] Tanaka et al, (2003), Comparative study on the excitons in lead-halide-based perovskite-type crystals CH3NH3PbBr3 CH3NH3PbI3," *Sci. direct*, vol. 127, pp. 619–623, 2003.

[67] Edri et al, (2014), Elucidating the charge carrier separation and working mechanism of $CH_3NH_3PbI_{(3-x)}Cl_{(x)}$ perovskite solar cells., *Nat. Commun.*, vol. 5, p. 3461.

[68] Farzaneh A. R., Najmeh A., Vahid A., Aldo D-C., Karim O. A., Ali S-Z. T., Farzaneh S. G., Masoud P., Nasibeh M. R. F., (2018), Bulk heterojunction polymer solar cell and perovskite solar cell: Concepts, materials, current status, and opto electronic properties,. Solar Energy 173 407–424.

[69] Zhyrair G., Vladimir G., and Yurii L., (2016), Large diffusion lengths of excitons in perovskite and TiO2 heterojunction, Applied Physics Letters 108, 051109.

[70] Ibn-Mohammed T., Koh S.C.L., Reaney I.M., Acquaye A., Schileo G., Mustapha K.B., Greenough R., (2017), Perovskite solar cells: An integrated hybrid lifecycle assessment and review in comparison with other photovoltaic technologies Renewable and Sustainable Energy Reviews 80 (2017) 1321–1344

[71] Kang, D.-H., & Park, N.-G. (2019). On the Current-Voltage Hysteresis in Perovskite Solar Cells: Dependence on Perovskite Composition and Methods to Remove Hysteresis. Advanced Materials, 1805214.doi:10.1002/adma.201805214

[72] Elumalai, N. K., & Uddin, A., (2016),.Hysteresis in organic-inorganic hybrid perovskite solar cells. Solar Energy Materials and Solar Cells, 157, 476 509. doi:10.1016/j.solmat.2016.06.025.

[73] Elumalai, N., Mahmud, M., Wang, D., & Uddin, A. (2016). Perovskite Solar Cells: Progress and Advancements. Energies, 9(11), 861. doi:10.3390/en9110861

[74] Kim, H.-S., Jang, I.-H., Ahn, N., Choi, M., Guerrero, A., Bisquert, J., & Park, N.-G. (2015). Control of I–V Hysteresis in CH3NH3PbI3 Perovskite Solar Cell. The Journal of Physical Chemistry Letters, 6(22), 4633–4639. doi:10.1021/acs.jpclett.5b02273.

[75] Unni K., Manjot K., Manjeet K., Akshay K., (2019), Factors affecting the stability of perovskite solar cells: a comprehensive review," J. Photon. Energy 9(2), 021001.

[76] Wang, S., Jiang, Y., Juarez-Perez, E. J., Ono, L. K., & Qi, Y. (2016). Accelerated degradation of methylammonium lead iodide perovskites induced by exposure to iodine vapour. Nature Energy, 2(1), 16195. doi:10.1038/nenergy.2016.195.

[77] Aristidou, N., Sanchez-Molina, I., Chotchuangchutchaval, T., Brown, M., Martinez, L., Rath, T., & Haque, S. A. (2015). The Role of Oxygen in the Degradation of Methylammonium Lead Trihalide Perovskite Photoactive Layers. Angewandte Chemie, 127(28), 8326–8330. doi:10.1002/ange.201503153.

[78] Sylla, A., Touré, S., and Vilcot, J. P. (2017). Numerical Modeling and Simulation of CIGS-Based Solar Cells with ZnS Buffer Layer. Open Journal of Modelling and Simulation, 5, 218-231..

[79] Nadia, M., (2016). Study Of The Effect Of Grading In Composition On The Performance Of Thin Film Solar Cells Based On AlGaAs And CZTSSe, A Numerical Simulation Approach, Doctorat Thesis In Énergétique, Université Med Kheider BISKRA, June

[80] Liu, Y., Sun, Y., & Rockett, A. (2012). A new simulation software of solar cells - WxAMPS. Solar Energy Materials and Solar Cells, 98, 124-128.

[81] M. Belarbi, A. Benyoucef , B. Benyoucef, (2014). Simulation Of The Solar Cells With Pc1d, Application To Cells Based On Silicon, Advanced Energy: An International Journal (Aeij), Vol. 1, No. 3.

[82] Burgelman, M., Decock, K., Niemegeers, A., Verschraegen, J., and Degrave, S. (2018). SCAPS manual , Version: 23 January 2018.

[83] Marc Burgelman, (2018). Models for the optical absorption α (λ)of materials in SCAPS, 20-1-2018, Correspondence address: Dept. of Electronics and Information Technology (ELIS), University of Gent, 'Belgium'. E-mail: Marc.Burgelman@elis.ugent.be

[84] Singh Surjeet. (2017). Mathematical Modeling of a P-N Junction Solar Cell using the Transport Equations. Browse all Theses and Dissertations. 1775.(2017).

[85] Atlas User's Manual, Device simulation software, Santa Clara, California 95054, November 7, 2014.

[86] Löper, P., Stuckelberger, M., Niesen, B., Werner, J., Filipic, M., , Moon, S., Yum, J., Topic, M., De Wolf, S., Ballif, C., et al. (2015). Complex refractive index spectra of CH3NH3PbI3 perovskite thin films determined by spectroscopic ellipsometry and spectrophotometry. Journal of Physical Chemistry Letters 6, pp. 66–71.

[87] SCAPS data base 2018. Version sacps3307.

[88] Minemoto,T., Murata, M. (2014). Impact of work function of back contact of perovskite solar cells without hole transport material analyzed by device simulation. Current Applied Physics 14. 1428e1433.

[89] Mandadapu,U.,Vedanayakam, S. V., and Thyagarajan,K. (2017). Simulation and Analysis of Lead based Perovskite Solar Cell using SCAPS-1D. Indian Journal of Science and Technology.Vol 10(11).

[90] Wolf,S. D.,Holovsky,J., Moon,S. J., Löper, P., Niesen, B.,edinsky, M, Haug, F. J., Yum, J. H., and Ballif,C. (2014). Organometallic Halide Perovskites: Sharp Optical Absorption Edge and Its Relation to Photovoltaic Performance. J. Phys. Chem. Lett. 5, 1035−1039.

[91] Yi, M., Jang, W., & Wang, D. H. (2019).Controlled pH of PEDOT:PSS for Reproducible Efficiency in Inverted Perovskite Solar Cells: Independent of Active Area and Humidity. ACS Sustainable Chemistry & Engineering.doi:10.1021/acssuschemeng.8b06619

[92] Voroshazi, E., Verreet, B., Buri, A., Müller, R., Di Nuzzo, D., &Heremans, P. (2011). Influence of cathode oxidation via the hole extraction layer in polymer:fullerene solar cells. Organic Electronics, 12(5), 736–744.doi:10.1016/j.orgel.2011.01.025

[93] Meiss, J., Uhrich, C. L., Fehse, K., Pfuetzner, S., Riede, M. K., & Leo, K. (2008). *Transparent electrode materials for solar cells. Photonics for Solar Energy Systems II.*doi:10.1117/12.781275 .

94<91 Wang,Y.,Xia,Z., Liang, J., Wang, X.,Liu, Y.,Liu, C.,Zhang, S., andZhou, H. : Towards printed perovskite solar cells with cuprous oxide hole transporting layers: a theoretical design. Semicond. Sci. Technol. 30 054004 (7pp).(2015).

[95] Azri,F.,Labed,M., Meftah,A. F.,Sengouga,N.,Meftah, A. M. (2016). Optical characterization of a-IGZO thin film for simulation of a-IGZO(n)/l-Si(p) heterojunction solar cell. Opt Quant Electron 48:391, (2016).

[96] Chen,A.,Zhu,K.,Shao, Q. (2016). Understanding effects of TCO work function on the performance of organic solar cells by numerical simulation. Semicond.Sci. Technol. 31 065025 (6pp).

[97] Haider,S. Z.,Anwar,H., and Wang, M. (2018). A comprehensive device modelling of perovskite solar cell with inorganic copper iodide as hole transport material.Semicond. Sci. Technol. 33, 035001 (12pp).

[98] Sajid, A.,Elseman, M.,Ji, J.,Dou, S.,Huang, H.,Cui, P.,Wei, D.,Li, M. (2016). Novel hole transport layer of nickel oxide composite with carbon for high-performance perovskite solar cells", Chin. Phys. B. 25(9): 097303.

[99] Miyata, A., Mitioglu, A., Plochocka, P., Portugall, O., Wang, J. T.-W., Stranks, S. D., … Nicholas, R. J. (2015). Direct measurement of the exciton binding energy and effective masses for charge carriers in organic–inorganic tri-halide perovskites. Nature Physics, 11(7), 582–587. doi:10.1038/nphys3357

[100] Fan, Z., Wei, M., Haizhong, G., Yicheng, Z., Xinyan, S., Kuijuan, J., He, T., Qing, Z., Dapeng, Y., Xinghua, L., Gang, L. and Sheng, M. (2016). Interfacial Oxygen Vacancies as a Potential Cause of Hysteresis in Perovskite Solar Cells. acs.chemmater.5b04019.

[101] Feng, W., Sai, B., Wolfgang, T., Anders, H. and Feng, G. (2018). Defects engineering for high-performance perovskite solar cells. npj Flexible Electronics 2:22.